AN EXPERIMENTAL STUDY OF VERTICALLY UPWARD AIR-WATER TWO-PHASE SLUG FLOW USING HOT-FILM ANEMOMETRY

CENTRE FOR NEWFOUNDLAND STUDIES

TOTAL OF 10 PAGES ONLY
MAY BE XEROXED

(Without Author's Permission)

GUANJUN WANG

001311

CENTRE FOR NFLD. STUDIES
MEMORIAL UNIVERSITY
OF NEWFOUNDLAND

INFORMATION TO USERS

This manuscript has been reproduced from the microfilm master. UMI films the text directly from the original or copy submitted. Thus, some thesis and dissertation copies are in typewriter face, while others may be from any type of computer printer.

The quality of this reproduction is dependent upon the quality of the copy submitted. Broken or indistinct print, colored or poor quality illustrations and photographs, print bleedthrough, substandard margins, and improper alignment can adversely affect reproduction.

In the unlikely event that the author did not send UMI a complete manuscript and there are missing pages, these will be noted. Also, if unauthorized copyright material had to be removed, a note will indicate the deletion.

Oversize materials (e.g., maps, drawings, charts) are reproduced by sectioning the original, beginning at the upper left-hand corner and continuing from left to right in equal sections with small overlaps.

ProQuest Information and Learning
300 North Zeeb Road, Ann Arbor, MI 48106-1346 USA
800-521-0600

UMI®

National Library of Canada
Acquisitions and Bibliographic Services
395 Wellington Street
Ottawa ON K1A 0N4
Canada

Bibliothèque nationale du Canada
Acquisitions et services bibliographiques
395, rue Wellington
Ottawa ON K1A 0N4
Canada

Your file Votre référence

Our file Notre référence

The author has granted a non-exclusive licence allowing the National Library of Canada to reproduce, loan, distribute or sell copies of this thesis in microform, paper or electronic formats.

L'auteur a accordé une licence non exclusive permettant à la Bibliothèque nationale du Canada de reproduire, prêter, distribuer ou vendre des copies de cette thèse sous la forme de microfiche/film, de reproduction sur papier ou sur format électronique.

The author retains ownership of the copyright in this thesis. Neither the thesis nor substantial extracts from it may be printed or otherwise reproduced without the author's permission.

L'auteur conserve la propriété du droit d'auteur qui protège cette thèse. Ni la thèse ni des extraits substantiels de celle-ci ne doivent être imprimés ou autrement reproduits sans son autorisation.

0-612-73566-4

Canada

AN EXPERIMENTAL STUDY OF VERTICALLY UPWARD AIR-WATER TWO-PHASE SLUG FLOW USING HOT-FILM ANEMOMETRY

By

© Guanjun Wang

(B. Eng. M. Sc.)

A thesis submitted to the School of Graduate Studies
in partial fulfillment of the requirements for
the degree of Doctor Philosophy

Faculty of Engineering and Applied Science
Memorial University of Newfoundland
December, 2001

St. John's Newfoundland Canada

Abstract

An experimental study has been conducted to investigate two-phase slug flow and the closure problem of two-phase flow models. To investigate the problem experimentally, a 3-inch ID and 180-foot long close loop re-circulation multiphase flow research facility was constructed at the Fluids Laboratory, Memorial University of Newfoundland (MUN). Accurate instrumentation of this facility makes it suitable for both conducting multiphase flow research and testing multiphase flow measurement systems. A new flow pattern map has been developed based on dimensional analysis. The functional equation governing the flow pattern formation was analyzed to yield the proper dimensionless plotting parameters. The use of these parameters makes the resultant flow pattern map independent of flow geometry and fluid physical properties. Data collected from the MUN flow loop as well as from the literature were used to generate the new flow pattern map. Flow pattern boundaries were systematically determined using a pattern recognition technique

The second part of this study is focused on vertically upward concurrent slug flow. A simultaneous flow measurement system using both dual-probe hot-film anemometry and high-speed flow visualization was used to obtain the quantitative flow information. To discriminate the signal into the gas and liquid phases, a combined amplitude and first-order time derivative phase detection method has been developed. The void fraction of the flow was estimated from the resultant phase indicator function. An innovative data reduction technique using wavelet analysis combined with the phase detection method was developed to decompose the original signals into signals corresponding to air slugs and small air bubbles. This technique results in two velocities corresponding to slugs and bubbles from cross-correlation analysis of the discriminated signals. Slug/bubble velocities, slug/bubble sizes, slug/bubble frequencies and slug/bubble void fractions were also estimated from the decomposed signals. Slug flows under a variety of flow conditions were investigated to yield a detailed description of the flow. The calculated mean velocities of air slugs, bubbles and liquid slugs are slightly lower than those predicted by the correlations in literature. Necessary modifications of these models were, therefore, recommended. Models for predicting void fraction, slug

void fraction, slug/bubble dimensions and bubble frequency were also developed. The results obtained from the hot-film signal processing technique were verified by the two image processing methods.

A technique for approximating the interfacial area concentration from a single normal probe was proposed in this study. Comparison of the measurements conducted in this study with the reported interfacial area concentration models developed based on bubble flow indicates that these models are not suitable for slug flow. An interfacial area concentration model was, therefore, formulated for slug flow based on the synthesis method. The proposed correlation indicates that the interfacial area concentration is closely related to flow and fluid properties. In summary, the study presented in this thesis provides a detailed quantitative flow description and information for formulating accurate constitutive equations for vertically upward air-water two-phase slug flow.

Acknowledgements

I would like to express my deep and sincere appreciation to my supervisor, Dr. Chan Ching, for his constant and patient guidance and encouragement. With the help of his expertise, some important problems have been solved. Special thanks are given to Dr. Neil Hookey, Dr. D'Arcy Hart, Dr. Hinchey and Associate Dean, Dr. Haddara, Faculty of Engineering and Applied Science, Memorial University of Newfoundland for their encouragement throughout the course of my study. I would like to thank John Hiscock for his valuable help with the image processing algorithms. Also, I would like to thank all the personnel in Fluids Laboratory for their kindly assistance during the experiments.

I am especially thankful to my wife Wenbo and my family, whose understanding and constant moral support made it possible for me to complete the thesis.

Additionally, the financial support from Natural Sciences and Engineering Research Council (NSERC) of Canada, Memorial University of Newfoundland and INSTRUMAR Limited is gratefully acknowledged.

Table of Contents

List of Figures

List of Tables

Nomenclature

Roman Letters

Δt_{12}	time duration of the bubble passing over the probe, s
A	cross sectional pipe area, m^2
a_i	interfacial area concentration, m^{-1}
A_{sg}	surface area of the gas phase, m^2
d	gas bubble or slug diameter, m
D	pipe diameter, m
D_H	channel diameter, m
f	frequency, Hz
g	gravitational acceleration constant, m/s^2
$g(x)$	bubble chord length probability density function
G_L	liquid mass flux, kg/m^2s
L	location of the flow observation site, m
l	slug or bubble length, m
M_{ik}	generalized interfacial drag, N/m^2
P	pressure, N/m^2
q	volume flow rate, m^3/s
Q	total flow over a time period, m^3
r	measurement location, m
R	pipe radius, m
R_{xy}	cross correlation function
S	phase velocity ratio
t	time, s
T	total time period, s
u	absolute phase velocity, m/s
U	superficial phase velocity, m/s
u_t	terminal velocity, m/s
V	hot film output, $volt$
V_T	total flow volume, m^3

Dimensionless Groups

Fr	Froude number
Re	Reynolds number

Greek Letters

τ_k^t	turbulent stress, N/m^2
ρ	density, kg/m^3
$\rho(\tau)$	cross correlation coefficient
μ	dynamic viscosity, $kg/m\ s$
ν	kinematic viscosity, m^2/s

τ	time delay, s
α	time fraction
ε	void fraction
β	volume flow ratio
τ_i	interfacial shear stress, N/m^2
Γ_k	mass generation, kg
σ	surface tension, N/m^2
ϕ	wavelet function
ψ	scale function
$\bar{\tau}_k$	average viscous stress, N/m^2
γ	surface-to-volume ratio, m^{-1}

Subscripts

b	bubble
c	center
G	gas phase
i	summation index
k	phase number
L	liquid phase
LS	liquid slug
M	mixture

Chapter 1

Introduction

Multiphase flows are common in the oil and gas industry. The unprocessed oil well stream from a petroleum reservoir is a multiphase mixture of crude oil, water and natural gas. Real-time information about the oil-water-gas production rates of each well would result in improved reservoir management and operational control, and thereby maximize the recovery from the reservoir, however, this data is currently not available. Conventionally, on a monthly or semi-monthly basis, the output from each well is diverted to an off-line test separator system, and the flow rates are estimated from measurements on the separated flow components (Figure 1.1). The separation equipment and flow handling operations are expensive and bulky, and the procedure to measure a set of flow rates requires several hours. Also, extrapolation of the data outside the measurement interval presents a high degree of uncertainty, as the flow rate sampling is effectively done only over a small fraction of the total production time of the well. The need within the oil industry for compact and reliable in-line instruments to measure the oil-water-gas flow rates of the unprocessed oil well streams is well-established (Millington 1997, Hutton 1997).

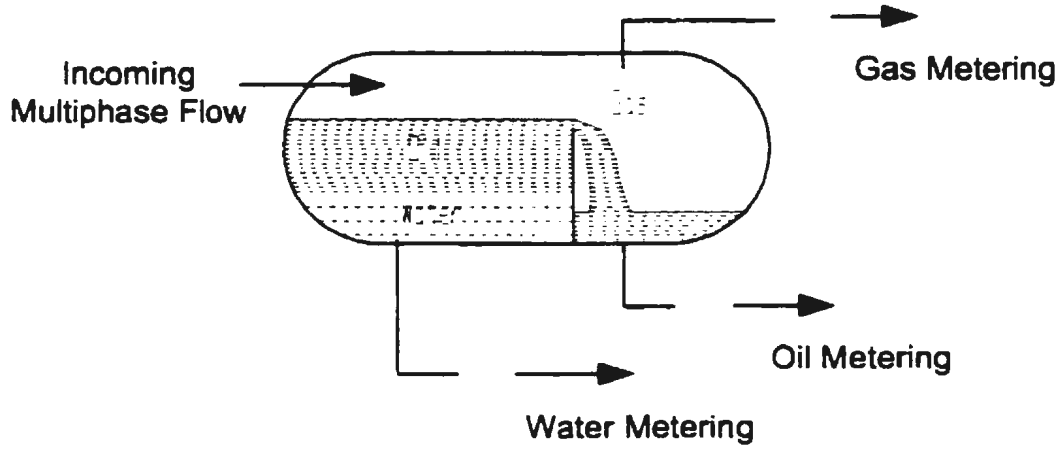

Figure 1.1 - Schematic of conventional multiphase flow metering method

Ideally, such an in-line flow measurement system should be sufficiently accurate, non-intrusive, reliable, flow pattern independent and suitable for use over the entire component fraction range (Thorn et al. 1997). However, the flow mechanism of multiphase flows differs substantially from that of single-phase flows. Consequently, the relatively mature techniques for single-phase flow measurement cannot simply be applied to multiphase flow. At present, direct flow measurement techniques for the individual components of multiphase flow do not exist. An alternative solution is to use inferential measurement techniques. Inferential methods require the knowledge of phase velocities, densities and cross sectional phase fractions to determine the phase flow rates. The density information can be inferred from temperature and pressure measurements for the gas phase and by direct measurement for the liquid phase. The most challenging part of this technique is, however, to determine the phase fractions and velocities.

Research and development of in-line real-time Multi-Phase Flow Meters (MPFM) has emerged only over the past 20 years. Since then, the development, evaluation and use of multiphase flow metering systems have rapidly become a major focus within the

multiphase flow community and the entire oil and gas industry. Currently, technology has advanced to the point where operators are now considering the installation of a MPFM as a serious option in both new and marginal fields for operational purposes. Several MPFMs, such as AGAR, FLUENTA 1900VI, FRAMO, MFI Full Range and KONGSBERG MCF-351, have been developed and commercialized. These meters have been developed to achieve a measurement uncertainty of ±10% over a reasonably wide flow range (Millington 1997). However, the targeted uncertainty of ±5% of reading over the entire fraction ranges and flow patterns has yet to be achieved (Thorn et al. 1997).

1.1 INSTRUMAR MPFM

INSTRUMAR LTD., with the assistance of C-CORE and Memorial University of Newfoundland (MUN), has been developing an in-line MPFM. The INSTRUMAR MPFM is based on electroquasistatic sensing technology (Figure 1.2). This device is designed to meet the specifications listed in Table 1.1, and will initially be tested in a multiphase flow loop at MUN.

Table 1.1 INSTRUMAR MPFM specifications

Characteristic	Specification
Max. Working Pressure	10 MPa (1500 PSI)
Explosion Environment	Class 1, Division 1, Group B (CSA)
Weight	420 kg (925 lbs.)
Inside Diameter	74 mm (3-inch Sch. 80)
Intrusions or Flow Restrictions	None
Flow Velocities	0.5-7.6 m/s
Installation Orientation	Vertical (upwards flow)

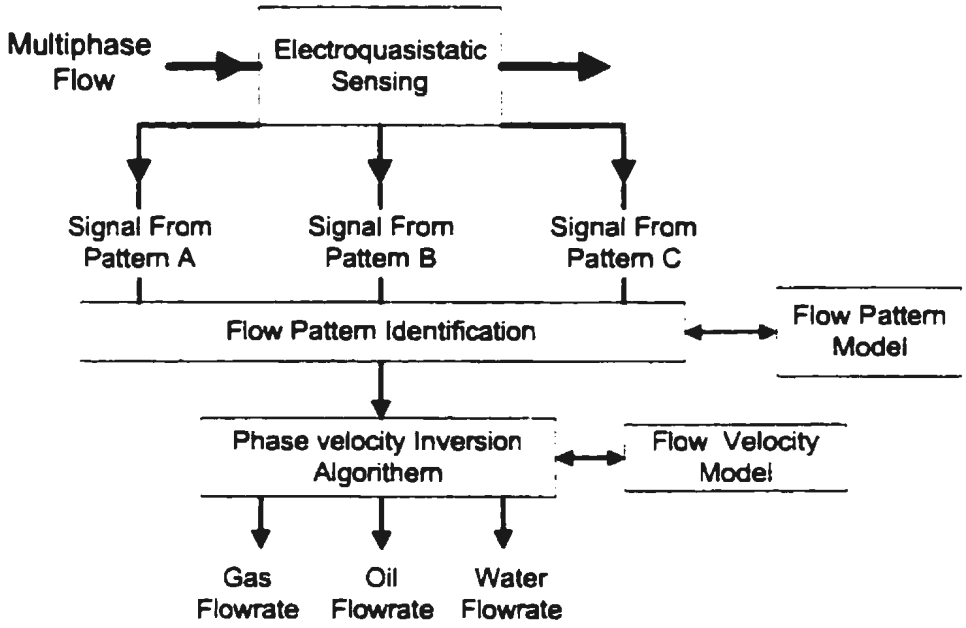

Figure 1.2 - Schematic of INSTRUMAR MPFM working principle

The meter operates by measuring a sequence of impedances at two streamwise locations. Like all other multiphase flow metering systems, this device has two fairly distinct tasks: to measure the fraction of oil, gas and water in the flow; and to measure and interpret the velocities of each component. The meter contains metal sensing elements deposited on a cylindrical ceramic insert, which monitor the flow as it passes through the meter. In order to measure the fractions over the entire range of water fractions, two types of sensing elements are used. One sensing element measures oil continuous flows, and the other measures brine continuous flows. Each sensing element has 26 electrodes, with different voltage patterns used to measure the impedance at different sections of the flow. The full set of measurements is made in less than 1.3 milli-seconds, which effectively provides the measurements at the same section of the flow.

Each of the voltage patterns is sensitive to a different region of the flow, and the measurements provide sufficient independent information to obtain phase fractions for the entire section.

The velocities are estimated by cross correlation analysis of signals at two streamwise locations along the flow. There are two locations for each type of measurement from the sensing elements, for a total of four sets of data. Data are collected at a rate of 400 Hz from each sensor. Signal processing algorithms are designed to detect multiple velocities, and provide a correlation quality factor for each velocity. The multiple velocities are then processed to provide a single average velocity value for each component. Flow pattern identification is done by monitoring a time series of phase fraction measurements, and comparing the gas/liquid parameters with patterns that are characteristic for each type of flow. The velocity data are then combined with the phase fraction information to determine the volume flow rates of each flow component.

1.2 Nature of the Problem

The motivation of the research described in this thesis is to support the INSTRUMAR MPFM development project. The investigation of vertically upward multiphase flows is of primary interest because the meter is configured to operate in this orientation. Unlike single-phase flow, several flow patterns (regimes) with distinct physical characteristics are present in the multiphase flow. The formation mechanisms of these flow patterns are complex and different for different flow patterns. The INSTRUMAR MPFM interprets the flow patterns based on the information extracted from the different electrode patterns. A large number of flow patterns are likely to be

encountered in practice, therefore, the correct identification of the flow patterns is critical for accurate signal interpretation. Additionally, the phase velocity inversion algorithm of the meter requires an accurate and robust flow model.

For two-phase (gas-liquid) vertically upward flow, four principal flow patterns have been identified (Hewitt and Hall-Taylor 1970). They are bubble flow, slug flow, churn and annular flows, with transition flow patterns between the neighboring flow regimes. The presence of a third component, oil, further complicates the problem. However, there are no apparent three-phase effects observed in vertically upward flows as observed in horizontal flows since there is less opportunity for the separation of oil and water to occur (Hall 1997). As a result, three-phase oil-water-air vertically upward flow has flow patterns similar to those in two-phase flow with the oil and water phases considered as one homogenous liquid phase. Air-water two-phase flow patterns are good approximations to the oil-water-gas flow patterns for vertically upward flow (Hall 1997). The modeling of air-water two-phase flow can, therefore, provide valuable information on understanding the oil-water-gas multiphase flow.

However, even for gas-liquid two-phase flow, the complexity of the flow makes it difficult to obtain a complete analytical (theoretical) solution. Various flow models such as the homogeneous flow model, separated or mixed two-phase-flow model and two-fluid model have been proposed to obtain solutions for two-phase flow. The two-fluid model is considered the most accurate because it permits different gas and liquid velocities as well as different flow directions. The accuracy of the two-fluid model depends to a great extent upon its closure laws, which include the flow pattern model and interfacial transfer model.

1.3 Overview of the Thesis

A multiphase flow research facility was designed and constructed to experimentally investigate the multiphase flow. Based on dimensional analysis, an innovative and robust flow pattern identification technique with universal portability was developed. The study is then focused mainly on slug flow. A hot-film anemometry flow measurement system and a high-speed flow visualization system were developed to measure void fraction, slug/bubble velocities, slug/bubble sizes, slug/bubble frequencies and interfacial area concentration. Effective signal and image processing techniques were developed to deduce the quantitative flow information from both measurement systems. The results provide the information for understanding the flow and formulating the closure laws for two-phase flow models.

1.4 Organization of the Thesis

This thesis consists of nine chapters. Chapter 2 presents a comprehensive review of two-phase flow measurements, flow pattern maps and flow models. The objectives of this research are described, together with the problem definition, in chapter 3. Chapter 4 details the design and construction of the MUN multiphase flow research loop as well as the data acquisition and operational control system. The two-phase flow measurement systems: hot film anemometry and high-speed flow visualization are also presented in this chapter. In chapter 5, the dynamic response of the hot-film probe to the passage of a gas slug is initially investigated with the assistance of high-speed flow images. A complete understanding of flow and probe interaction leads to the development of a data

reduction scheme using wavelet analysis coupled with a sophisticated phase detection method. This method is used to extract void fraction, slug/bubble velocities, slug/bubble sizes, slug/bubble frequencies and interfacial area concentration. Result verifications with high-speed flow images are also presented in this chapter.

In chapter 6, the functional equations governing the flow pattern formation and interfacial exchange are analyzed using the dimensional analysis technique. The resultant dimensionless functional equations provide guidelines for developing the flow pattern map and interfacial area concentration model. Results of the dimensionless flow pattern map are presented in chapter 7. This innovative flow pattern mapping technique provides a direction for obtaining a universal flow pattern map. Comparison of this flow pattern map with data in the literature is discussed.

Chapter 8 provides an extensive analysis of void fraction, slug/bubble velocities, slug/bubble sizes, slug/bubble frequencies and interfacial area concentration under a variety of flow conditions. Models for predicting void fraction, slug void fraction, slug/bubble velocities, slug/bubble sizes, bubble frequency and interfacial area concentration are proposed based on the present measurements. Chapter 9 summarizes the results presented in the earlier chapters and provides the conclusions and recommendations for further work.

Chapter 2

Flow Fundamentals and Literature Review

The introduction of a second phase in a flow complicates the flow modeling. The fluid properties, which are known or readily calculated at every position in single-phase flow, can no longer be determined directly from the total gas and liquid flow rates for two-phase flow. This is due to the fact that the gas and liquid travel at different velocities in two-phase flow. The large number of phase interfaces between the gas and liquid further complicates the problem. At each gas-liquid interface, mass, momentum and energy are transferred from one phase to the other. Such transfers are deemed to play a major role in two-phase flow modeling. The understanding of the interfacial transfer is, however, far from complete, because the transfer mechanisms and the interfacial areas over which they take place are difficult to specify analytically or to measure experimentally (Levy 1999).

Various aspects of two-phase flow have been investigated in order to understand its extremely complex flow behavior. A vast amount of technical information on two-phase flow in a vertical flow channel is available in the literature. Some relevant information, particularly pertaining to flow metering, flow modeling and its measurement, is reviewed in this chapter. The review starts with the introduction of two-

phase flow fundamentals and several common two-phase flow models. To implement these flow models, proper flow measurement methods are required to provide the quantitative flow information. Both intrusive and non-intrusive flow measurement techniques for acquiring such information are reviewed in the latter part of this chapter.

2.1 Fundamentals of Two-Phase Flow

Due to the complex nature of two-phase flow, it is extremely difficult to have a complete analytical solution. Various flow models have been proposed to obtain solutions to two-phase flow problems. Time-averaged flow properties are often used in these models since two-phase flows are intermittent in their overall or local time behavior, and their variations with time are significantly larger than for single-phase flows. The earliest two-phase flow models were simple and only used as an analytical tool. They used uniform flow and thermal conditions and were, therefore, referred to as homogeneous models. The closure laws for homogeneous models can be derived readily from the methodology for single-phase flow (Levy 1999). The next evolution is the separated two-phase flow models without dealing specifically with the interfaces, flow patterns or any potential non-thermal equilibrium conditions. They were formulated in terms of area- and time-averaged parameters of the flow by assuming constant fluid properties. Since no interfacial interactions were considered, these models had to rely upon semi-empirically or empirically derived closure laws for gas volume fraction and pressure drops (Levy 1999).

The most recent and perhaps most accurate models are two-fluid models including interfacial exchange. Two-fluid models permit different gas and liquid

velocities and directions and hence reflect the flow in a more realistic manner. Ishii (1975) developed a practical three-dimensional two-fluid model using temporal and statistical averaging. Without considering the thermal problem, the governing equations can be written as follows:

Conservation of Mass:

$$\frac{\partial}{\partial t}(\varepsilon_k \rho_k) + \nabla \cdot (\varepsilon_K \rho_k u_k) = \Gamma_k \tag{2-1}$$

Conservation of Momentum:

$$\frac{\partial}{\partial t}(\varepsilon_k \rho_k u_k) + \nabla \cdot (\varepsilon_k \rho_k u_k^2) = -\varepsilon_k \nabla P_k - \nabla \cdot \varepsilon_k (\bar{\tau}_k + \tau_k^t) + \varepsilon_k \rho_k g + u_{ki}\Gamma_k + M_{ik} - \nabla \varepsilon_k \cdot \tau_i \tag{2-2}$$

where Γ_k, M_{ik}, and τ_i are the mass generation, generalized interfacial drag and interfacial shear stress, respectively. The subscript k denotes the 'k' phase, and i stands for the value at the interface. ε_k, ρ_k, u_k, and P_k denote void fraction, density, velocity and pressure of the k phase. $\bar{\tau}_k$, τ_k^t and g stand for average viscous stress, turbulent stress and gravitational constant of phase k at the interface. The interfacial transfer terms should obey the balance law at the interface. The interfacial transfer conditions can be obtained from an average of the local jump condition as (Ishii 1975, Ishii and Mishima 1984):

$$\sum_k \Gamma_k = 0 \tag{2-3}$$

$$\sum_k M_{ik} = 0 \tag{2-4}$$

Two-fluid models recognize the presence of flow patterns and treat the exchanges at the gas-liquid interface specifically. Consequently, in addition to the constitutive equations for ∇P_k, $\bar{\tau}_k$, τ_k' and τ_i, the two-fluid models require the closure laws to explicitly deal with the phase interface and flow patterns. In general, the interfacial transfer terms, Γ_k and M_{ik}, can be modeled in terms of interfacial area concentration and the corresponding driving forces (Ishii 1975, Ishii and Mashima 1984) as:

$$\Gamma_k = -\rho_{ki}(u_{ki} - u_i) \cdot n_{ki} a_i \tag{2-5}$$

$$M_k = -\rho_{ki} u_{ki} (u_{ki} - u_i) \cdot n_{ki} a_i \tag{2-6}$$

The interfacial area concentration (density) or interfacial surface area per unit volume, a_i, is defined as the ratio of the gas phase surface area and the total flow volume:

$$a_i = \frac{A_{sg}}{V_T} \tag{2-7}$$

where A_{sg} is the surface area of the gas phase, and V_T is the total flow volume. Also, because the closure is dependent upon flow pattern, the flow pattern model must be specified (Levy 1999).

It is also necessary to define other parameters for two-phase flow. Void fraction is a measure of the state of a two-phase flow. Conventionally, the void fraction, ε, of gas-

liquid two-phase flow is defined as the fraction of the pipe cross-sectional area (or volume) occupied by the gas phase (Hetsroni 1982). There is slip between the two phases, because of the velocity difference between the gas and liquid. Phase slip, S, is a measure to characterize this velocity difference. It is defined as the ratio of gas and liquid absolute velocities:

$$S = \frac{u_G}{u_L} = \frac{q_G / A\varepsilon}{q_L / A(1-\varepsilon)} = \frac{q_G / \varepsilon}{q_L /(1-\varepsilon)} = \frac{q_G(1-\varepsilon)}{q_L \varepsilon} \tag{2-8}$$

where u is the absolute flow velocity, q is volumetric flow rate, and A is the pipe cross sectional area. The subscripts G and L refer to gas and liquid. The definition of phase velocity ratio makes it easy to define other two-phase flow parameters. Void fraction ε can be obtained by transforming equation 2-8 as:

$$\varepsilon = \frac{q_g}{Sq_L + q_G} \tag{2-9}$$

Phase superficial velocity U, which is the bulk flow velocity of each phase, can be written as $\frac{q}{A}$. The phase velocity ratio (or phase slip) can be expressed in terms of U as:

$$S = \frac{u_G}{u_L} = \frac{q_G / A\varepsilon}{q_L / A(1-\varepsilon)} = \frac{U_G / \varepsilon}{U_L /(1-\varepsilon)} = \frac{U_G(1-\varepsilon)}{U_L \varepsilon} \tag{2-10}$$

It is important to differentiate the void fraction from volume flow ratio. The volume flow ratio, β, is defined as the ratio of gas volume flow rate to the total volume flow rate.

$$\beta = \frac{q_G}{q_G + q_L} \tag{2-11}$$

Comparing equations 2-9 and 2-11, β and ε are equal only if $S=1$, which implies there is no slip between the two phases. In the case of vertically upward flow ($S>1$ because of the buoyancy), β is greater than ε at all times. Another important parameter, especially in the context of a point measurement of the flow, is the time fraction α_G. It is defined as the ratio of time a sensor is in the gas phase to the total time over a specific measurement period. For an infinitesimal area (see Figure 2.1), dA, surrounding a sensor in the flow field, the total air flow across dA over a specific measurement time period Δt_G at location r is:

$$dQ_G(r) = u_G(r) \cdot dA \cdot \Delta t_G(r) \tag{2-12}$$

The local time fraction at this location can be expressed as:

$$\alpha_G(r) = \frac{\Delta t_G}{\Delta t} = \frac{dQ_G(r)}{\Delta t \cdot dA \cdot u_G(r)} = \frac{dq_G(r)}{dA \cdot u_G(r)} = \frac{U_G(r)}{u_G(r)} = \varepsilon(r) \tag{2-13}$$

The averaged time fraction α_G is the integration of $\alpha_G(r)$ over the entire pipe cross section. This integration results in:

$$\alpha_G = \frac{1}{A}\int_A \alpha_G(r)dA = \frac{1}{A}\int_A \frac{dq_G}{u_G dA}dA = \frac{1}{A}\frac{q_G}{u_G} = \frac{1}{A}\frac{q_G}{\frac{q_G}{A\varepsilon}} = \varepsilon \qquad (2\text{-}14)$$

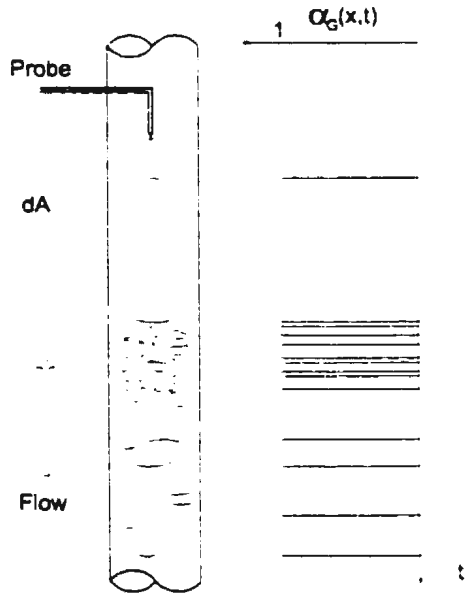

Figure 2.1 - Schematic Void Fraction measurement

Thus, the time fraction and void fraction are equivalent parameters. This permits the void fraction to be determined directly from the time fraction measurements, which are much easier to perform.

2.2 Flow Pattern Maps

One of the most important tasks in two-phase flow modeling is to be able to predict the flow patterns under various flow conditions. The flow patterns of two-phase flow depend on several factors including phase flow rates, fluid physical properties as well as flow geometry. Despite the complex nature of the flow, the distribution of gas and liquid in two-phase flow can be categorized into a few dominant flow patterns. The inconsistency of the flow pattern definitions has resulted in a variety of flow pattern names being used in the literature. This is partly because of the subjective nature of flow pattern definitions and partly because of a variety of names being given to essentially the same flow pattern (Hetsroni 1982). Among the different definitions, Hewitt and Hall-Taylor's (1970) description of the flow patterns might be the most accurate and recognized. They identified four main flow patterns for upward gas-liquid two-phase flow in vertical tubes, classified as bubble flow, slug flow, churn flow, and annular flow (Figure 2.2). Based on the definition of Hewitt and Hall-Taylor, McQuillan and Whalley (1985) gave a much more detailed description of the four flow patterns as follows:

- Bubble flow (Figure 2.2a): The liquid is the continuous phase, and the gas is dispersed in the liquid in the form of bubbles of variable shape and size, usually distorted spheres.
- Slug (plug) flow (Figure 2.2b): When the bubble concentration in the flow increases, bubble coalescence occurs, and the largest bubbles are of the same order of size as the tube diameter. Further coalescence results in the deformation of the bubble into bullet shaped pockets of gas, which characterize the slug flow. Slug flow consists of these pockets of gas, commonly called plugs (or gas slugs) or Taylor bubbles, separated by

regions of bubble flow, commonly called liquid slugs. The plugs of gas are surrounded by a thin liquid film, which usually flows vertically downwards.

- Churn flow (Figure 2.2c): Churn flow is a highly disordered flow in which the vertical motion of the liquid is oscillatory. Churn flow possesses some of the characteristics of slug flow, with the main differences being: (a) the gas slugs become narrower and more irregular; (b) the continuity of the liquid in the slug is repeatedly destroyed by regions of high gas concentration; and (c) the thin film of liquid surrounding the gas slugs can no longer be observed.
- Annular flow (Figure 2.2d): In annular flow the gas flows along the center of the tube. The liquid flows partially as a film along the walls of the tube, and partially as droplets in the central gas core.

Figure 2.2 - Schematic flow patterns in vertically upward gas-liquid flow

Between each of these flow patterns, there exist a number of transition flow patterns that possess the characteristics of more than one of the main flow patterns

(McQuillan and Whalley 1985). The slug/churn flow occurs when the flow pattern oscillates between slug and churn, and the churn/annular flow occurs when the flow appears as annular flow but with occasional intermittent churn flow. Although the problem of two-phase flow modeling is reduced to dealing only with these specific flow patterns, within a given flow pattern, the flow behavior can be very complex and not amenable to any direct calculation. This has led to a variety of phenomenological models, which have been applied with varying degrees of success (Hetsroni 1982).

The usual way of predicting two-phase flow patterns is to form a so-called flow pattern map in which the flow patterns are plotted with two axes representing certain physical characteristics of the two phases. Kosterin (1949) was probably the first to suggest the use of the flow pattern map technique, which was later extended by Hoogendoorn (1959). Baker (1954) developed a flow pattern map based on the experimental results from horizontal 2.54-mm ID pipes. He used superficial phase velocities as the two axes, and included the effect of fluid density, viscosity, and surface tension at atmospheric conditions as correction factors. The inclusion of surface tension in Baker's flow pattern map is probably due to the small diameter pipe he used. Spedding and Spence (1993) indicated that the accuracy of Baker's flow pattern map was poor for 4.55-mm and 9.35-mm ID pipes. This is to be expected, since the diameter effect is not considered in Baker's flow pattern map. Although Baker's flow map was modified through the introduction of more flow pattern information, those maps showed no significant improvements (Spedding and Spence 1993). This is primarily because the pipe geometry and fluid physical properties were not considered in this technique.

Using data collected from a 4.55-mm ID pipe, Spedding and Nguyen (1980) proposed a series of empirical flow pattern maps, covering flow angles from vertically upwards to vertical downwards. They identified the Froude number of the mixture, $Fr = U_M / \sqrt{gd}$, and phase flow ratio, q_L/q_G, as the plotting parameters. Their flow maps presented a promising approach towards a universal flow pattern map because of the consideration of pipe diameter and gravitational effects, and the adoption of dimensionless groups. However, this mapping technique did not attract much attention, probably because of the lack of a proper theoretical analysis. Later, using 2.54-mm and 9.53-mm ID pipes, Lin and Hanratty (1987) investigated the flow pattern formation and transition mechanics, and proposed flow pattern maps based on superficial phase velocities. Again, the improper handling of pipe geometry and the lack of fluid physical property information in their maps resulted in a poor agreement with results from other diameter pipes.

Among the flow pattern mapping techniques, superficial phase velocities, in different forms, have been the most widely used mapping parameters (Baker 1954, Lin and Hanratty 1987). Others used either the mass flow rates or mass velocity expressions for defining flow pattern maps (Scott 1963, Newson 1964, Bennett et al. 1965). A small number of workers (Spedding and Nguyen 1980) adopted dimensionless groups, mainly the Froude number as the main mapping parameter. The most widely used flow pattern maps are probably those recommended by Hewitt and Roberts (1969), which use the superficial phase momentum fluxes (Figure 2.3) and Taitel et al. (1980), which use the superficial phase velocities as the mapping parameters (Figure 2.4).

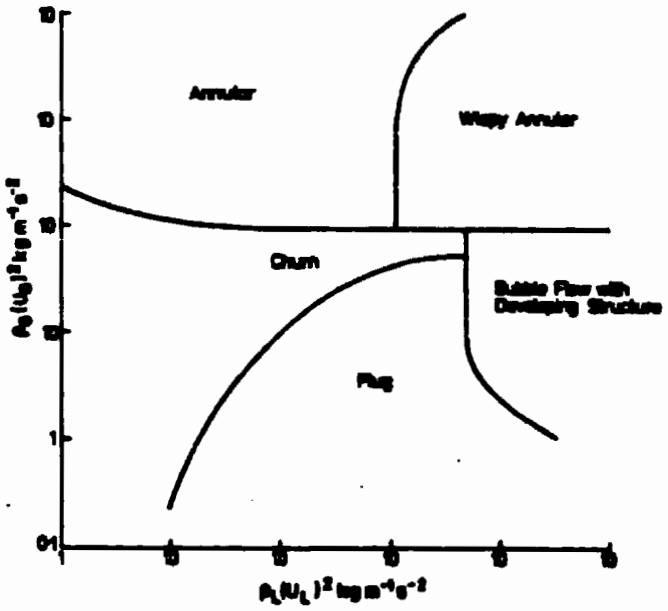

Figure 2.3 – Flow pattern map (Hewitt and Roberts 1970)

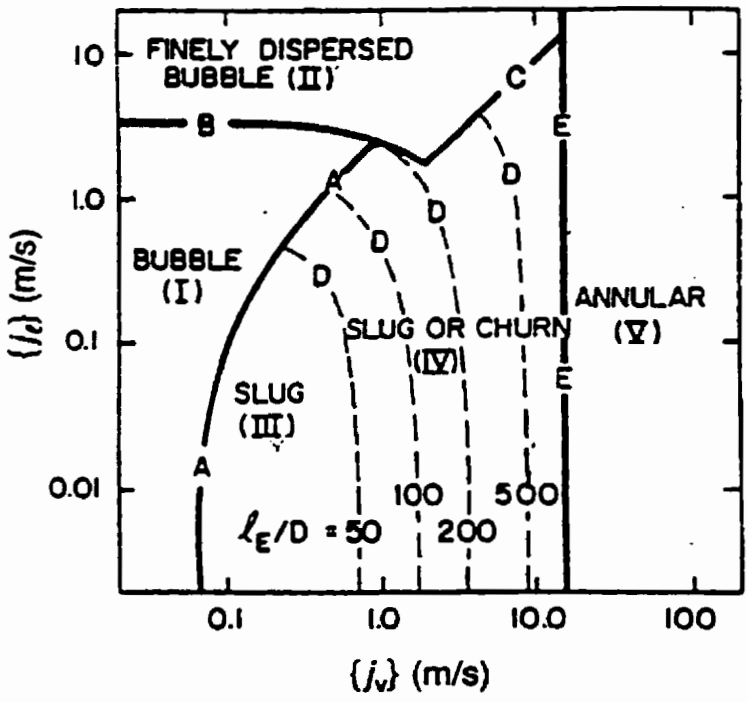

Figure 2.4 – Flow pattern map (Taitel et al. 1980)

In Figure 2.4, j_v and j_l are the superficial gas and liquid velocities, and l_E/D is the flow observation location and pipe diameter ratio. In addition to the experimental flow pattern mapping techniques, theoretical flow pattern maps (McQuillan and Whalley 1985) have also been developed. The postulated mechanisms by which the transition between flow patterns occurs are investigated, and then a series of equations are produced for predicting the flow patterns. Chen and Brill (1997) also developed a model to predict the transition from slug flow to churn flow in vertical pipes based on an analysis of the physical mechanism of the wake effect of the Taylor bubbles on the highly aerated liquid slugs. However, because of the complex nature of the flows, a complete analytical solution to the problem is still an elusive goal.

2.3 Two-Phase Flow Modeling

The rise of bubbles through a liquid, both individually and in swarms, has received considerable attention. Experimentally, Haberman and Morton (1953), Peebles and Garber (1953) and Harmathy (1969) studied the rise of single bubbles in an infinite medium and proposed a series of correlations for drag coefficient and bubble terminal velocity. Zuber and Hench (1962) performed what was probably the first most comprehensive study on bubble flow with a 10-cm ID Plexiglass tube filled with water and equipped with various types of orifice plates through which air could be introduced at the bottom. They measured the average gas volume fraction as the gas flow rate was changed, investigated the dimension change, shape change and distribution change of bubbles with gas flow rate and distinguished three types of bubble flows: ideal bubbling flow, transition flow and churn-turbulent flows.

Wallis (1961) was among the first to present a theoretical approach to estimating the bubble velocity by assuming that the flow was frictionless and that there was no variation in gas volume fraction or velocity across the channel. He related the bubble velocity to the liquid velocity, bubble terminal velocity and void fraction. Later, Zuber (1964) extended Wallis' analysis by incorporating the viscosity of the continuous phase for laminar bubble flow. The presence of wall shear stress was found to increase the drag on the flow and the bubble drag coefficient was affected by the bubble diameter (Zuber 1964).

There is general agreement that bubble flow exhibits a distribution of bubble sizes and shapes, and that the bubble characteristics are variable and depend on flow conditions, fluid properties, and the way that the bubbles are generated or introduced into the flow system. In recent years, there has been increasing interest in understanding the detailed mechanisms of bubble flow. Serizawa et al. (1987) measured the lateral void fraction distribution in vertical pipes. They described four different major gas volume patterns: wall peak, intermediate peak, transition and core peaks. They suggested that larger bubbles tend to migrate toward the center of the channel. A similar observation was also reported by Wang et al. (1987). Liu (1991) pointed out that the initial bubble size influences the volume distribution, especially at low liquid flow.

Slug flow is characterized by a succession of liquid slugs separated by large Taylor bubbles whose diameter approaches that of the tube. The earliest solutions dealing with Taylor bubbles rising in a channel were reported by Davis and Taylor (1950) under the assumption that viscosity and surface tension can be ignored. Accordingly, the asymptotic rising velocity of the bubble can be calculated from potential flow theory.

Davis and Taylor (1950) postulated that the velocity close to the pipe wall was in the axial direction and that the pressure at the bubble boundary was constant. Wallis (1962) studied the rise of Taylor bubbles for a variety of fluids in vertical tubes of different diameters and recommended a slug velocity correlation. He observed three different types of air slug/bubble shapes. When viscosity dominated, the bubbles were rounded at both ends and there was no turbulence in the wake. When viscosity and surface tension were negligible, the bubbles were rounded at the nose and flat at the tail with a strong toroidal vortex prevalent in the wake. Finally, when surface tension became significant, the bubble nose filled more and more of the tube, and the bubble exhibited an additional contraction or expansion just prior to its tail.

Table 2.1 Correlation equations for bubble/slug velocity

Author	Correlation	Limitation
	Bubble	
Peebles and Graber (1953)	$u_t = 1.18[\frac{\sigma g(\rho_L - \rho_G)}{\rho_L^2}]^{1/4}$	Single bubble in infinite media
Harmathy (1969)	$u_t = 1.53[\frac{\sigma g(\rho_L - \rho_G)}{\rho_L^2}]^{1/4}$	Single bubble in infinite media
Wallis (1961)	$\bar{u}_G - \bar{u}_L = u_t(1-\varepsilon)$	Frictionless
Zuber (1964)	$u_{bs} = \frac{g\Delta\rho d^2}{18\mu_L}(1-E_G)^3$	d < 0.05 cm
Zuber (1964)	$u_{bs} = 1.14(\frac{\sigma g\Delta\rho}{\rho_L^2})^{1/4}(1-E_G)^{3/2}$	0.05 < d <2 cm
Zuber and Findlay (1965)	$\bar{u}_G = C_o U_m + 1.53(\frac{\sigma g\Delta\rho}{\rho_L^2})^{1/4}$	Frictionless
	Slug	
Davis and Taylor (1950)	$u_t = 0.35(\frac{gd\Delta\rho}{\rho_L})^{1/2}$	U_L=0 and neglect surface tension
Nicklin et al. (1962)	$\bar{u}_G = 1.2U_m + 0.35c\sqrt{gd}$	Frictionless

Griffith and Wallis (1961) probably presented the first theoretical analysis of gas slug velocity in vertical tubes. They expressed the rising velocity of a gas slug as a function of Reynolds number, total superficial velocity, gravity and tube diameter. Subsequently, Nicklin et al. (1962) refined this slug velocity expression by taking into account the non-uniform velocity profile ahead of the bubble. Griffith (1963) measured the gas slug velocity in non-circular channels in the region where inertia forces are dominant. He reported that in a rectangular channel the larger dimension was the important one and the liquid ran down the smaller side as the gas slug rose. Ellis and Jones (1980) found that the gas slug velocity dependence on diameter disappears as the tube size exceeds 4 to 6 inches based on the maximum permissible bubble diameter constrained by Taylor hydrodynamic instability. Table 2.1 summarizes several correlations proposed by different authors for estimating the bubble and slug velocities.

Interfacial area concentration has been less investigated and remains poorly understood in two-phase flow, despite its importance in determining the inter-phase transfer of mass, momentum and energy. A number of interface area concentration correlations have been proposed to resolve the closure problem of two-phase flow models, mostly for bubble flow. Some approaches correlate the interfacial area concentration with frictional pressure drop, $(\frac{\Delta P}{L})_f$, or total frictional pressure drop, $(\frac{\Delta P}{L})_T$ (Kasturi and Stepank 1974, Shimimkan and Stepank 1977, Tomida et al. 1978, Dejuses and Kawaji 1990). Others derived the correlations in terms of some other flow parameters. Akita and Yoshida (1974) correlated the interfacial area concentration in terms of dimensionless parameters for bubble flow in a 15-cm ID tube. Tabie et al.

(1989) correlated the interfacial area concentration with the void fraction. Using the data obtained from a 1.2-cm ID tube for bubble flow with phase change, Zeitoun et al. (1994) also proposed an interfacial area correlation in terms of dimensionless parameters. Some of the reviewed correlations for interfacial area concentration are provided in Table 2.2. The recent study of Delhaye and Bricard (1994) indicated that, in bubble flow, the interface area and the bubble diameter increase as the gas volumetric fraction increases. A similar trend was also reported by Park (1992) for both air-water flow and laminar air-oil flow.

Table 2.2 Interfacial area correlations and models

Author	Correlation
Kasturi and Stepank (1974)	$a_i(\frac{q_L}{1-\varepsilon}) = 2.26\times10^{-5}(\frac{\Delta P}{L})_f^{1.07}$
Akita and Yoshida (1974)	$a_i D_h = \frac{1}{3}(gD_h^2\frac{\rho_f}{\sigma})^{0.5}(g\frac{D_h^3}{\nu_f^2})^{0.1}\varepsilon^{1.13}$
Shilimkan and Stepank (1977)	$a_i(\frac{q_L}{1-\varepsilon}) = 3.61\times10^{-5}(\frac{\Delta P}{L})_f^{1.31}$
Tomida et al. (1978)	$a_i = 0.22(\frac{\Delta P}{L})_T\cdot\varepsilon$
Tabie et al. (198)	$a_i = 2100\varepsilon^{1.25}(1-\varepsilon)^{0.75}$
DeJuses and Kawaji (1990)	$a_i = 1.535(\frac{\Delta P}{L})_T^{0.12}U_G^{1.2}U_L^{-0.14}(1-\varepsilon)^{1.6}$
Zeitoun et al. (1994)	$a_i = 3.24\varepsilon^{0.757}(\frac{g\Delta\rho}{\sigma})^{0.55}(\frac{\mu}{G_L})^{0.1}$

2.4 Two-phase Flow Measurements

Quantitative flow information, such as local phase velocities, void fraction, slug/bubble sizes and phase interfacial area concentration, is required to develop and validate the mechanistic flow models. Several intrusive and non-intrusive methods have

been developed to perform such measurements. Intrusive measurement techniques have been frequently used in laboratory settings. The most common intrusive techniques use resistivity probes, optical probes and hot-film probes. Each method is based on an operating principle of phase detection using variations in the local fluid properties of the two phases. The three methods, which provide local information, are only accurate provided that the sampling times are sufficiently long to give statistically accurate results. The gas bubble velocities are most often estimated from two measurements along the streamwise locations. A cross-correlation between the signals from the two probes yields an average time-difference-of-arrival at the two probes. The velocities are estimated from the distance between the sensors and the resultant time-difference-of-arrival.

Figure 2.5 - Schematic response of a cylindrical hot-film probe to the passage of a gas bubble

In hot-film anemometry, an electronic feedback circuit is used to maintain the sensing element/probe at a constant temperature higher than the surrounding fluid. The output voltage is proportional to the heat transfer from the sensor to the surrounding

fluid. Measurements using hot-films exploit the larger difference in heat transfer from the sensor to the liquid and gas. For a sufficiently long observation, the fraction of time the probe detects the gas can be interpreted as the local void fraction (Serizawa 1974). In order to discriminate the hot-film signal into the gas and liquid, the dynamic response of the anemometer output to the passage of gas bubbles over the probe needs to be clearly understood.

Farrar and Brunn (1989) investigated the interaction between a cylindrical single normal (*SN*) probe and a gas bubble. For the simple case of a direct hit of a gas bubble to the *SN* hot-film probe, the signal response to the passage of a bubble can be explained with reference to Figure 2.5. When a bubble approaches the probe (A), the anemometer output voltage E increases, because the bubble moves with a velocity greater than the average liquid velocity. The signal continues to increase until the bubble front reaches the probe (B). The process of the probe piercing the bubble is characterized by a steep voltage drop in the signal. When the probe is inside the gas bubble, a slow evaporation of the liquid film on the sensor occurs. At some stage the liquid film between the prongs may break, giving rise to a peak (F). However, in most cases the film will not break before the back of the bubble arrives. When the back of the bubble arrives (G), the liquid phase moves around the probe. The rapid covering of the sensor with the liquid results in a steep rise in the signal voltage, ending at peak 3. The 2-3 part of the signal is caused by a dynamic meniscus effect (Farrar and Bruun 1989). Following peak 3, the signal drops slowly towards the average velocity of the liquid phase as the bubble moves away from the probe. In summary, two events (1 and 2) need to be clearly identified in order to extract the void fraction. The passage of the gas bubble corresponds to the time

difference $\Delta t_{12} = t_2 - t_1$. Having identified the two events for each gas passage, the void fraction, ε, can be determined from the time fraction (see equation 2-13).

In the early research, an amplitude threshold was used as a discriminator to discretize the signal into the gas and liquid phases (Resch et al. 1974, Abel and Tesch 1978, Jones and Zuber 1978). Any data points below the voltage threshold are deemed to be associated with the gas phase, and those points above are assumed to represent the liquid phase. This method is simple in both concept and application. However, the most significant disadvantage of this scheme is that it does not identify either of the two events and makes no distinction between events 2 and 3. Serizawa et al. (1983) proposed an improved detection technique based on a slope threshold method, in which the first-order time derivative of the signal is compared with one or more threshold levels. Misintepretation may occur when film breakage takes place. To overcome this, Farrar (1988) developed a combined amplitude threshold and slope analysis scheme. This scheme consists of an initial amplitude method for bubble detection, followed by a search method to locate the two events associated with the passage of a bubble.

Liu and Bankoff (1993a, b) also developed a combined amplitude and slope threshold phase discrimination scheme using eight decision algorithms where the amplitude, and forward and backward slopes of the signal are compared with the amplitude and slope thresholds. This method has the advantage of incorporating more of the real physics of bubble-probe interaction. Farrar et al. (1995) further refined their technique by taking into account the significant liquid film breakage spike events. The optimun amplitude and slope are determined by using the probability density function. Although this technique can successfully identify virtually all bubbles in the flow and

eliminates the signal peak associated with liquid film breakage, signals associated with tiny bubbles cannot be detected. The discrimination techniques usually translate the hot-film signal into a binary signal, which indicates the two phases. The void fraction is simply calculated as the fraction of time the probe is in the gas phase (Farrar et al. 1995). From the void fraction measurement, the size and distribution of the gas bubbles can be estimated statistically (Wang et al. 1987). The mean phase velocities can also be estimated from the void fraction distribution and phase volume flow rates.

The instantaneous phase velocities can be determined if effective hot-film sensor calibrations in both the gas and liquid can be obtained. However, calibrations that are effective in both the liquid and gas phases are difficult to achieve. The calibrations are very sensitive to fluid temperature change due to the low overheat ratio imposed by the hot-film, and as a result, even a fraction of a degree change in temperature can lead to a significant error in the inferred velocity (Samways et al. 1994). Also, the evaporation of the residual liquid film on the sensor as the gas passes over the probe makes it extremely difficult to quantify the gas velocity inside the bubble. The calibration drift with fluid temperature creates a high uncertainty in interpreting the phase velocities. This problem can be sombewhat overcome by installing an in-line cooling system to maintain a constant liquid temperature (Samway el al. 1994)

The principle of two-phase flow measurements by resistivity probes is based upon the difference in conductivity between the gas and liquid. The probe yields a two-state signal indicative of the phase in gas-liquid flow, because a gas bubble behaves like an electrical insulator. Many of the early investigators (Uga 1972, Herringe and Davis 1974 and 1976, Serizawa et al. 1987) transformed the original analog signal into a binary data

series by presetting a voltage trigger level. The accuracy of the trigger level setting directly affects the accuracy of void fraction, bubble velocity and bubble size measurement, owing to the finite rising and falling times of bubble-probe interaction. Welle (1985) devised a system using two self-adjusting trigger levels for bubble detection, where the levels are updated according to the last measurement and the minimum and maximum values. Liu and Bankoff (1993b) used a miniature dual-sensor resistivity probe to measure the void fraction, bubble velocity and bubble size distribution in two-phase bubble flow. They developed an iterative routine of self-adjusted amplitude and slope phase discrimination scheme for phase identification. Both a multichannel analysis and a cross-correlation method were used to determine the bubble velocities. The local bubble size and its distribution were determined from the measured bubble chord length spectrum based on a statistical analysis of the bubble residence time (Uga 1972).

The operation of an optical fiber probe is based on sensing changes in the refractive index of the surrounding medium. In two-phase flow, the probe is able to discriminate between the two phases only if their refractive indices are sufficiently different. As with other types of intrusive probes, gas bubbles passing the probe are characterized by the rising and falling slopes on the output signal. Cartellier (1990) studied and compared the response of various optical probes to the passage of a bubble. He introduced the concept of the latency length, which is the spatial resolution of the interface detection by a given probe, and suggested that the latency length must be sought in order to ensure a better accuracy of the local void fraction. The processing of the raw signal requires the location of the gas/liquid interface. The simple amplitude thresholding techniques exhibit a high sensitivity to the processing criteria because the selection of the

thresholds is very subjective. A wave-form analysis providing the amplitude and shape of each signal was introduced by Cartellier (1992). By associating the signal rising time with the liquid/gas transition, Cartellier (1992) developed a technique to measure the bubble velocity and size simultaneously using a single probe. By cross correlating the optical probe measurements at two streamwise locations, Moujaes and Sparks (1998) obtained the profiles of void fraction, gas velocity and gas bubble diameter for different flow regimes along the cross-sectional, transverse axes in a rectangular channel.

Apart from the intrusive measurement methods, non-intrusive flow measurement techniques have been used in multiphase flow. These techniques have the obvious added advantage over intrusive techniques of not disturbing the flow. Common non-intrusive flow measurement techniques for multiphase flow include Pulsed Light Velocimetry (PLV), Holography, Laser Doppler Velocimetry (LDV), Nuclear Magnetic Resonance (NMR), Electrical Impedance Tomography (EIT) and Gamma Densitometers.

PLV is a technique that tracks fluid flow by imaging regions of the fluid within the flow field at two or more known times (Adrian 1991). Its measurements yield a collection of Lagrangian vectors describing the fluid motion. Common PLV measurement techniques are Particle Image Velocimetry (PIV), laser speckle velocimetry and Particle Tracking Velocimetry (PTV). Several hybrid PIV techniques have been developed to study two-phase flows. Gopal and Jepson (1998) developed a novel image analysis technique to study the dynamic slug flow characteristics in gas-liquid flows. Hay et al. (1998) used a backlighted imaging technique for drop size measurements in annular two-phase flows with small concentrations of drops in the gas phase. Meng et al. (1995) developed an optical system to obtain shadow-photographs of bubbles in a high-pressure

forced convection evaporator tube. The photographs are used to obtain bubble size, velocity and longitudinal position information. Peterson et al. (1983) developed a process of measuring bubble size and position by using an electronic circuit capable of recording two-dimensional spatial coordinates selected on a magnified video screen. The method was especially useful for nonspherical bubbles that often pose problems for intrusive probe measurement techniques. It is best suited to two-phase flows with relatively low velocities and low void fractions. Hawighorst (1983) used a technique of digital image analysis to measure bubble size and velocity in a three-phase fluidized bed system. The analysis uses a gradient calculation to determine the outline of each bubble. The significance of the holographic technique is its ability to obtain information in three-dimensions. Laser Doppler Velocimetry (LDV) has been used to study two-phase flows (Bachalo 1994). Ohba et al. (1987) used LDV to measure the bubble and liquid mean velocities in a square duct two-phase flow.

NMR imaging is a recently established non-invasive technique that can be used to study multiphase flow. Lemonnier (1997) investigated the use of NMR in two-phase air-water flows and determined that the technique can provide detailed information on the turbulence of both phases. The technique can also produce accurate measurements of the volume fraction, volumetric flux and phase flow rate for each individual phase of the mixture. Despite the requirement for expensive and complex equipment, the NMR technique has significant potential for local phase measurements in multiphase flow.

The basic principle of the impedance method is to measure the resistance and capacitance of the fluid. The measurement is achieved by placing electrodes around the pipe (Figure 2.6). The earlier impedance based methods had limited flow range and were

flow pattern dependent (Thorn et al. 1997). In order to reduce the flow pattern dependency, Merilo et al. (1977) devised a measurement system, which consisted of three pairs of electrodes spaced around the pipe. By sequentially measuring the conductance between each electrode, a rotating field is produced, resulting in a spatially averaged measurement. Lucas and Simonian (1991) also investigated the rotating field technique using multi-electrode capacitance sensors with oil-gas and oil-water flows. An alternative to the rotating field sensor is the helical sensor. Tests using this technique on both air-water and air-oil flows show that flow pattern independent measurements can be achieved (Abouelwafa and Kendall 1979, Hammer et al 1989).

Figure 2.6 - Schematic cross section of an impedance flow measurement system

EIT is an emerging technology based on the impedance sensing method. It provides an inexpensive solution for multiphase flow measurements (Seleghim and Hervieu 1998). Seleghim and Hervieu (1998) used EIT to detect large structures such as slugs in air-water two-phase flow and some finer details including the wavy or rugged

interface in stratified flow. Lemonnier (1997) performed similar work with air-water two-phase flows.

Figure 2.7 - Schematic cross section of a conventional γ-ray densitometer

Gamma densitometers are generally considered as a practical method for measuring volumetric phase fractions in multiphase flows (Lunde et al. 1998). A typical gamma densitometer setup consists of a radioactive source on one side of the test section and a detector on the other side (Figure 2.7). Lunde et al. (1998) successfully used a single energy gamma densitometer to make field measurements in the North Sea. Kirouac et al. (1999) used a gamma densitometer to obtain line-averaged and cross-sectional averaged void fractions in two-phase flow. The dual-energy technique employs two independent measurements along the streamwise direction to determine the oil, water and gas fractions and velocities (Abouelwafa and Kendall 1980, Roach et al. 1994, Van Santen et al. 1995, Hewitt et al. 1995). The primary limitations of gamma densitometers

are their long measurement times, limited spatial resolution and near wall measurement difficulty.

2.5 Summarizing Remarks

A review of the flow pattern maps shows little convergence for data from different flow facilities and fluid properties. Tests with data from different diameter pipes indicate that none of the discussed flow pattern maps can successfully accommodate changes in flow geometry and fluid properties. It is, therefore, useful to develop a universal flow pattern map. Such a flow pattern map can significantly simplify flow pattern identification.

Considerable progress has been made in understanding gas-liquid bubble/slug flows and predicting the terminal velocity of a single gas bubble/slug. Non-dimensional groupings taking into account bubble geometry and deformation were employed in most studies. Empirical correlations have been used in simplified analytical continuity models to approximately describe the behavior of a multitude of bubbles rising within a liquid. Two-dimensional measurements of gas volume fraction for bubble flow have been obtained to help formulate new mechanisms and explain the void distribution across the channel. To investigate the interfacial phase transfer mechanisms, several correlations for estimating the interfacial area have been proposed. Some shortcomings in our understanding of slug flows include:

1. Change in bubble size and geometry with flow conditions.
2. Bubble interactions, coalescence and clustering. This complex bubble behavior is expected to depend on bubble size and distribution and to influence the

multidimensional gas volume fraction and distribution of turbulent velocity fluctuations.

3. Detailed knowledge about the form and amount of gas present in the liquid film, slug and bubble.
4. The periodic changes in the direction of the liquid film flow.
5. The frequencies of air slugs and bubbles.
6. The influence of channel geometry on phase velocities and flow patterns.
7. The lack of data beyond air-water mixtures.
8. The effect of bubble dimension on the bubble velocity.
9. The lack of data and understanding of interfacial area concentration and its modeling for slug flow.

A variety of techniques have been employed to quantify two-phase flows. The dynamic interaction between a bubble and the hot-film probe has been investigated for interpretation of the signal. Relatively less is known about the interaction between the probe and a passing gas slug. Several data reduction schemes have also been developed to estimate void fraction and phase velocities. Some non-intrusive methods have been successfully used for two-phase flow measurements. There is general agreement that the velocities of the gas bubbles depend on their physical dimension and location in the flow field. It is necessary to relate the bubble velocity with the corresponding bubble size and its spatial location. Therefore, flow measurement techniques need to be further developed to obtain such flow information.

Chapter3

Research Objectives

A project was initiated at the Multiphase Flow Research Laboratory of MUN to investigate vertically upward gas-liquid two-phase flows. The research objectives were formulated based on the literature review and technical requirements of the INSTRUMAR MPFM. This chapter details the problem definition, objectives and scope of the research.

3.1 Problem Definition

The review of flow pattern mapping techniques has revealed that most of the flow pattern maps show little convergence for different flow facilities and fluids. These flow pattern maps are sensitive to pipe diameter and fluid properties, which makes them difficult to use. To overcome this, a new flow pattern mapping technique needs to be developed. The new flow pattern map will incorporate the flow dimension and fluid properties and hence make it independent of these parameters. In addition, the new flow pattern map will greatly simplify the flow pattern identification algorithm used by the MPFM and improve its portability in flow geometry and fluid properties.

Significant progress has been made on two-phase flow measurement techniques. Various techniques for flow qualification have been developed. In order to translate the output signal into the desired flow information, the dynamic interaction between a bubble and a probe has been investigated. However, no observation has been made on the interaction between the probe and the passing gas slugs. A good understanding of this interaction will provide valuable information for interpreting the output signal. Also, a more efficient and accurate gas bubble/slug detection technique needs to be developed to yield more detailed and complete flow information. This should lead to a better understanding of the flow physics and structure of two-phase flows.

Recently, there has been an increasing application of dual-probe techniques for estimating phase velocity. To better understand the flow and develop more accurate flow models, it is necessary to decompose this velocity into those corresponding to different gas bubble size groups.

3.2 Research Objectives

Guided by the problem definition described above, the objectives of this research are:

1. To design and construct a multiphase flow research facility to experimentally investigate vertically upward gas-liquid two-phase flows.
2. To develop a robust and effective flow pattern map for identifying and predicting the different flow patterns.
3. To develop robust flow measurement techniques to obtain accurate quantitative information about two-phase slug flow. This includes void fraction, slug/bubble

velocities, slug/bubble frequencies, slug/bubble dimensions and interfacial area concentration.

4. To verify the resultant flow measurements with high-speed flow visualization as well as with those reported in the literature.
5. To develop/validate models for predicting the void fraction, slug/bubble velocities, slug/bubble frequencies, slug/bubble dimensions and interfacial area concentration for two-phase slug flow.

Chapter 4

Experimental Facilities

The design, construction and commissioning of the multiphase flow loop at MUN are a significant part and a major contribution of this thesis. This flow loop is designed to simulate the various flow patterns and flow conditions that are commonly encountered in production oil well streams. The design of the flow loop was finalized in June 1997, and the flow loop was commissioned in January 1998. The design was based on the specification of the pre-production prototype MPFM of INSTRUMAR Ltd. (Marshall, 1996). Two measurement systems are incorporated into this flow loop: a high-speed flow visualization system and a hot-film anemometry system. The primary purpose of this flow loop is to investigate vertically upward gas-liquid flows in support of the INSTRUMAR MPFM development program. The flow loop also has a horizontal test section to study horizontal flows and it can be readily modified to perform a variety of other multiphase flow related studies. A detailed description of the test facility is presented in this chapter.

4.1 Outline of MUN Multiphase Flow Loop

Due to space and financial limitations, construction of a sophisticated multiphase flow facility with a stand-alone in-line phase separator was not feasible. A relatively compact 3-inch ID, 180-foot long open loop re-circulation system (Figure 4.1) was constructed in the Fluids Laboratory of MUN.

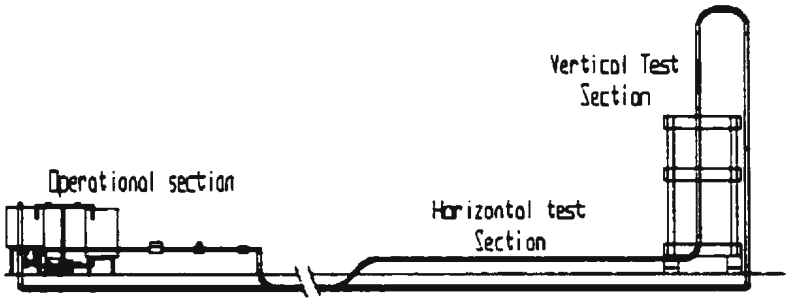

(a)

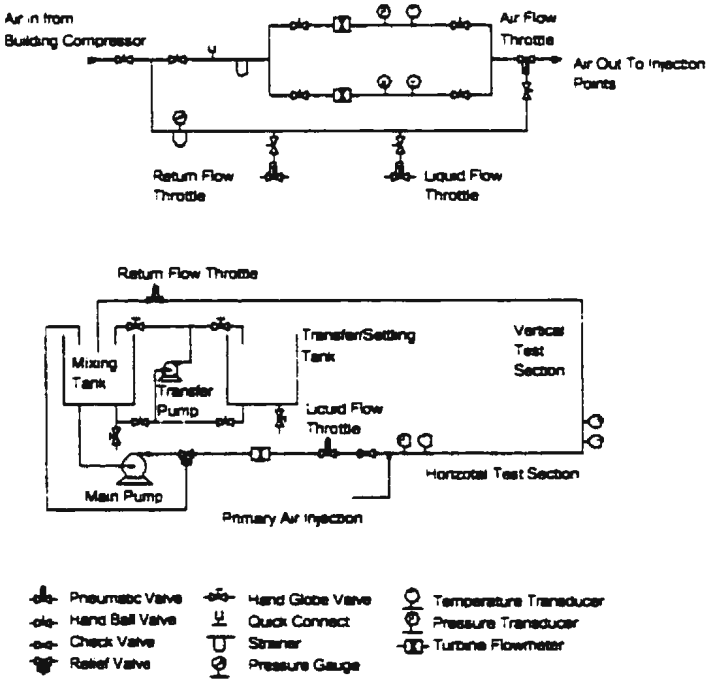

(b)

Figure 4.1 - (a) Flow loop layout (b) Schematic piping and instrumentation diagram

The flow loop consists of three major sections: operational section, horizontal test section and vertical test section. The return line is constructed below the floor level of the lab in a 2.5-foot deep trough in order to save space and to avoid other laboratory facilities. The flow loop is designed to generate different flow patterns and conditions of both horizontal and vertical multiphase flows, although current research is focused on vertically upward flow.

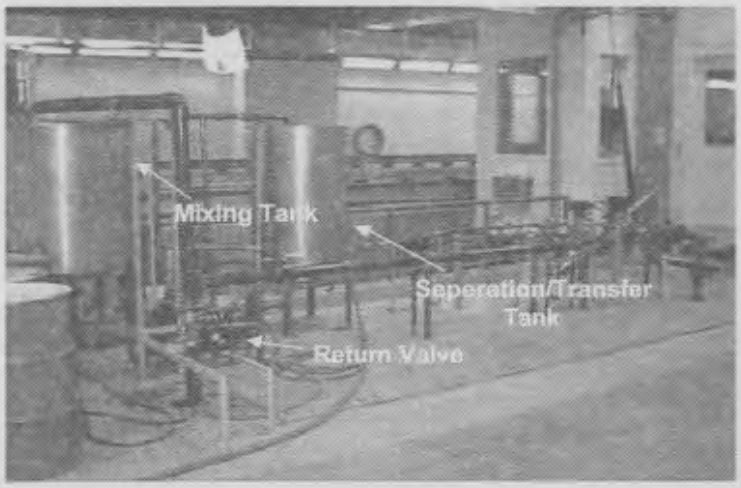

Figure 4.2 - Operational section of flow loop

To ensure proper phase mixing, and allow the flow patterns to fully develop, the distance from the air-liquid mixing tee to the horizontal flow observation section is about 250 pipe diameters. The vertical distance to the vertical test section is about 50 pipe diameters. For visual observation of the flow, clear PVC pipes are incorporated along the horizontal and vertical sections of the loop. A 3-foot long vertical section of the PVC pipe is replaced by optically clear Plexiglass tubing for better flow visualization. Long radius elbows are used in the loop construction to minimize flow disturbances due to the

change in flow direction. Pipe supports are carefully designed and tested to minimize system vibration. The effect of thermal stresses on the piping system was also considered during the design. Liquid is stored and pre-mixed in a 0.75-m^3 mixing tank at the operational section. In the case of oil-water-air multiphase flow tests, a 0.63-m^3 transfer/settling tank is used to separate the oil and water after each series of experiments. The water-oil mixture is transferred through a 1.5-inch ID copper pipe between the two tanks by a 1.1 kW transfer/settling pump. Figure 4.2 is a picture of the operational section showing both the mixing and transfer/settling tanks. Specifications of the flow loop are provided in Table 4.1.

Table 4.1 Flow loop specifications

Item	Specification
Mixing Tank	0.75 m^3
Separation Tank	0.63 m^3
Flow Loop Dimension	3-inch ID, 180-ft long Schedule 40 PVC pipe
Horizontal Test Section	6 m
Vertical Test Section	6 m
Transfer Piping	1.5-inch ID copper pipe
Liquid Flow Rate	10-260 GPM
Air Flow Rate	0.75-140 SCFM
Maximum Working Pressure	Max. 120 psia
Main Pump	Jacuzzi R5EM3-1 with 3.7 kW motor
Transfer Pump	Dynesco with 1.1 kW motor
Compressed Air Lines	½ and 1-inch ID steel pipes

* GPM = Gallon per minute; SCFM = Standard cubic feet per minute

Phase flow rates are monitored in real time by in-line liquid and gas flow meters. Electro-pneumatic control valves are installed on both the liquid and air lines to regulate the flow rates and loop pressure. Several temperature and pressure transducers are installed along the loop to monitor the flow conditions (see Figure 4.1b). Operational

control of the loop is implemented through a fully integrated computer system, which also handles the data acquisition from the flow meters, and pressure and temperature transducers. The loop can be pressurized to 120 psia to investigate the effects of pressure on the multiphase flow.

4.2 Flow Control System

Two 3-inch and one 1-inch ID pneumatic control valves are installed in-line to control the flow rate and loop pressure. Each control valve consists of a ball valve connected to a pneumatic actuator and an electro-pneumatic positioner. One 3-inch control valve is installed upstream of the test section to control the liquid flow, while the other is installed downstream in order to pressurize the loop.

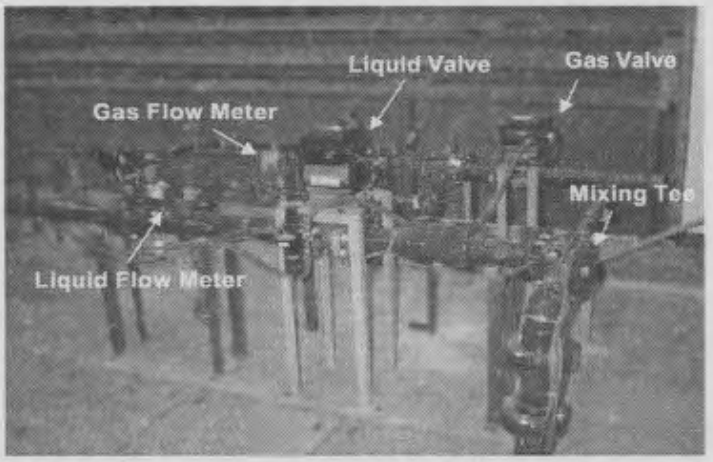

Figure 4.3 - Flow control and metering components

Figure 4.3 provides a picture of the liquid and gas control valves. The air line control valve is positioned downstream of the air flow meters to regulate the air flow rate. These values are controlled through a computer using a D/A card that generates a 4-20

mA DC control signal. LABTECH VISION (Figure 4.4) is employed to develop the graphical user interface (GUI) for the valve controls.

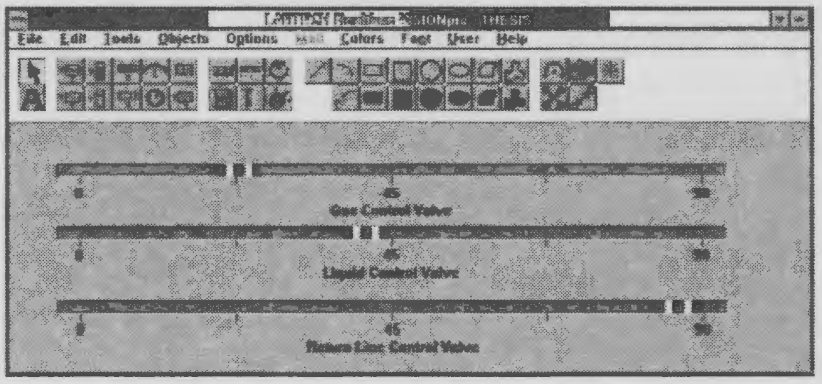

Figure 4.4 - LABTECH VISION showing control GUI for the control valves

4.3 Instrumentation

Accurate metering of the phase flow rates is critical for flow modeling, testing and calibrating the MPFM. As a result, a significant investment was made on the loop metering system. The flow rates of each phase are monitored through in-line flow meters. A 3-inch turbine flow meter (FTB-730, OMEGA) is used for liquid metering, and 1-inch (FTB-936, OMEGA) and ½-inch (FTB-931, OMEGA) turbine flow meters are used for air metering (see Figure 4.3). Two separate air flow meters are installed in parallel to ensure that the entire flow range specified by the MPFM can be covered with the desired resolution. The flow meters were selected according to the MPFM specifications and calibrated by the manufacturer over their operating ranges. Table 4.2 lists the detailed specifications of these flow meters. The high accuracy and repeatability of these flow meters ensure good credibility and confidence in the results.

Table 4.2 Specifications of flow meters

Model	ID (Inch)	Flow Range	Accuracy	Repeatability
FTB-730	3	3-600 *GPM*	± 1% full scale	N/A
FTB-931	½	0.35-3.5 *ACFM*	± 1% reading	± 0.25%
FTB-936	1	4-60 *ACFM*	± 1% reading	± 0.25%

* ACFM = Actual cubic feet per minute.

In order to convert the air volume flow rate to the loop conditions, pressures and temperatures in the air lines and the test sections are monitored in real time during loop operation. The pressure transducers are PX603-100G5V (OMEGA) for the liquid line, and PX603-200G5V (OMEGA) for the air lines. The thermocouples (TC(T)-NPT-U-72, OMEGA) are installed to measure the local temperature (See Table 4.3 for specifications). The positioning of the three flow meters, and the pressure and temperature transducers can be found in Figures 4.3 and 4.5.

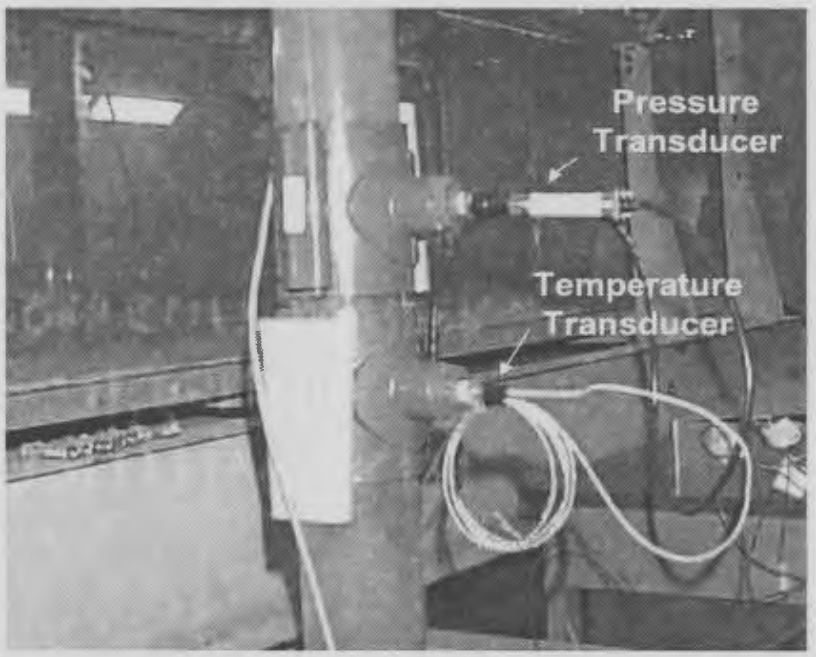

Figure 4.5 - Pressure and temperature transducers on vertical section

Table 4.3 Specifications of pressure and temperature transducers

Transducers	Model	Range	Accuracy	Repeatability
Pressure	PX603-100G5V	0-100 *PSIA*	± 0.4% BFSL	± 0.05% FS
Pressure	PX603-200G5V	0-200 *PSIA*	± 0.4% BFSL	± 0.05% FS
Temperature	TC(T)-NPT-U-72	< 287 °C	1 °C or 0.75% of the reading, whichever is greater	N/A

* Pressure and temperature transducers are calibrated by the manufacturer

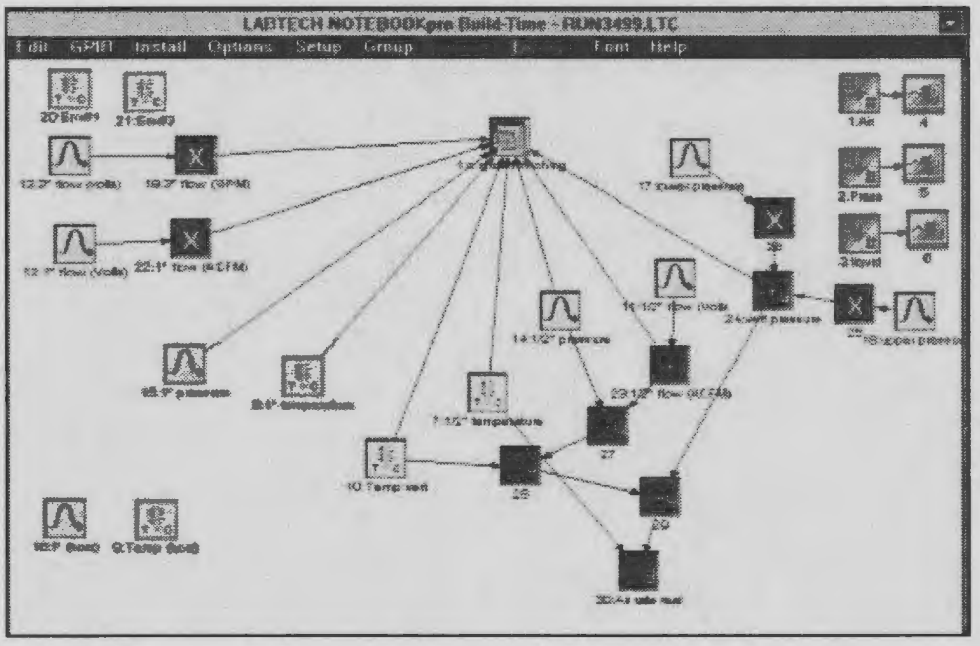

Figure 4.6 - LABTECH BUILD-TIME showing icons of instrumentation

Data logging is achieved and controlled using LABTECH BUILD-TIME (Figure 4.6). Each sensor and data conversion function is displayed as an icon. The data acquisition system accepts signals from the flow meters and transducers, and outputs signals to control the valves at a 10 Hz sampling rate. A signal conditioner CYEXP 32 Multiplexor, an A/D converter CYDAS 8 and a D/A converter CYDDA08I from Cyber Research are integrated into a computerized data acquisition and control system (Figure 4.7). The specifications of each component are listed in table 4.4.

Table 4.4 Data acquisition system

Mode	Resolution	Channel	Max. Sampling rate	Accuracy
CYEXP 32	N/A	32 single/16 differential	N/A	± 0.01% reading
CYDAS 8	12-bit	8 single-ended	20 kHz	± 0.01% reading
CYDDA08I	12-bit	8 channels	N/A	N/A

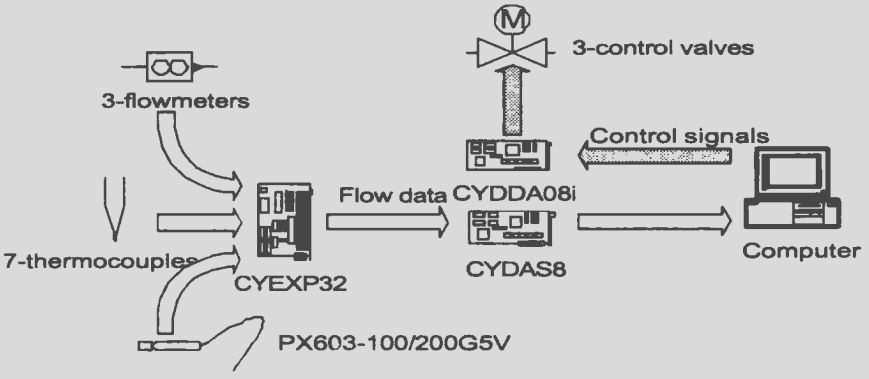

Figure 4.7 - Schematic data acquisition system

4.4 Hot-Film Anemometry and Flow Visualization

The test section for the hot-film and flow visualization is located 50 pipe diameters downstream of the nearest elbow in the vertical test section of the flow loop and is constructed of clear optical grade acrylic tubing. An elevated platform accommodates both the hot-film anemometry and the flow visualization system (Figure 4.8). The flow images are captured using a high-speed digital imaging system (MotionScope PCI 1000s) that consists of a CCD camera, PCI interface card and digital image memory with a maximum frame rate of 1000 frames per second (fps). The camera is mounted on a positioning stand and located on the elevated platform with a remote monitor (Figure 4.9).

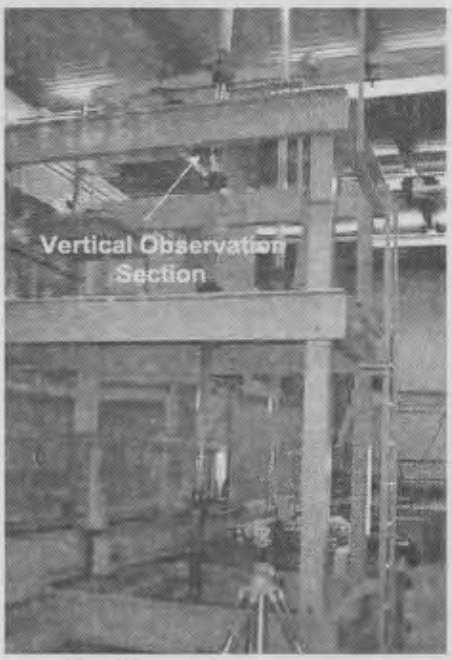

Figure 4.8 - Vertical test section along with observation platform

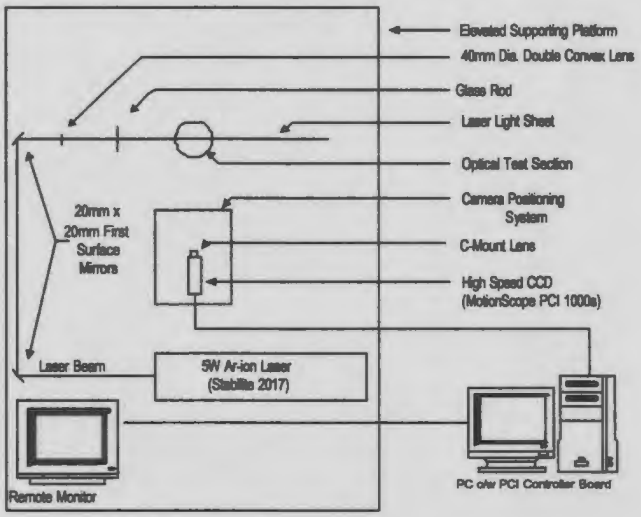

Figure 4.9 - Top view of flow visualization system

The system records a sequence of digital images of the flow at a pre-selected frame rate between 60 and 1000 fps, and stores the frames in an image memory on the controller unit. The images can be viewed forward or backward at any selected frame

rate, frame-by-frame or freeze frame, to analyze flow motion and time during the sequence. The electronic shutter operates at rates of 1× to 20× the set recording rate with exposure times shown in Table 4.5. Details of the frame rate, image resolution, number of stored frames and record time are provided in Table 4.6. Although the high-speed imaging system is capable of recording images at 1000 fps, picture resolution is reduced with an increase in frame rate. Consequently, frame rates of 250 and 500fps were optimum for the present test flow conditions.

Table 4.5 Exposure times for set shutter speeds

Frame Rate	60	125	250	500	1000
Exposure (s) @ 1X Shutter Speed (sec)	1/60	1/125	1/250	1/500	1/1000
Exposure (s) @ 2X Shutter Speed (sec)	1/120	1/250	1/500	1/1000	1/2000
Exposure (s) @ 3X Shutter Speed (sec)	1/180	1/375	1/750	1/1500	1/3000
Exposure (s) @ 4X Shutter Speed (sec)	1/240	1/500	1/1000	1/2000	1/4000
Exposure (s) @ 5X Shutter Speed (sec)	1/300	1/625	1/1250	1/2500	1/5000
Exposure (s) @ 10X Shutter Speed (sec)	1/600	1/1250	1/2500	1/5000	1/10000
Exposure (s) @ 20X Shutter Speed (sec)	1/1200	1/2500	1/5000	1/10000	1/20000

Table 4.6 Camera specifications

Frame Rate (fps)	Resolution (Pixels)	No. of Frames Stored	Total Record Time (s)
60	480 x 420	512	8.5
125	480 x 420	512	4.1
250	480 x 420	512	2.0
500	320 x 280	1024	2.0
1000	240 x 210	2048	2.0

A 5W Ar-Ion laser (Stabilite 2017) is used in conjunction with an optic setup to create a laser light sheet for the flow visualization. Space restrictions on the elevated platform necessitate a unique optic setup to create an adequately thin light sheet (Prenel et al. 1989). The optic setup consists of two first surface mirrors, a double convex lens and a glass rod. The two first surface mirrors are mounted at 45° angles to the beam and are aluminized on the surface closest to the incident light, thereby minimizing energy loss. The double convex lens is used to converge the beam before it passes through the glass rod to obtain a thin sheet of light. Figure 4.9 provides a schematic description of the system setup. A scale illuminated with a separate point light source, recorded as part of the flow image, is used to calibrate the image pixel resolution (Figure 4.10). Images were also obtained using a backlighting technique that consisted of two 500 W halogen photography lamps reflected off a matt finish white screen (Figure 4.11).

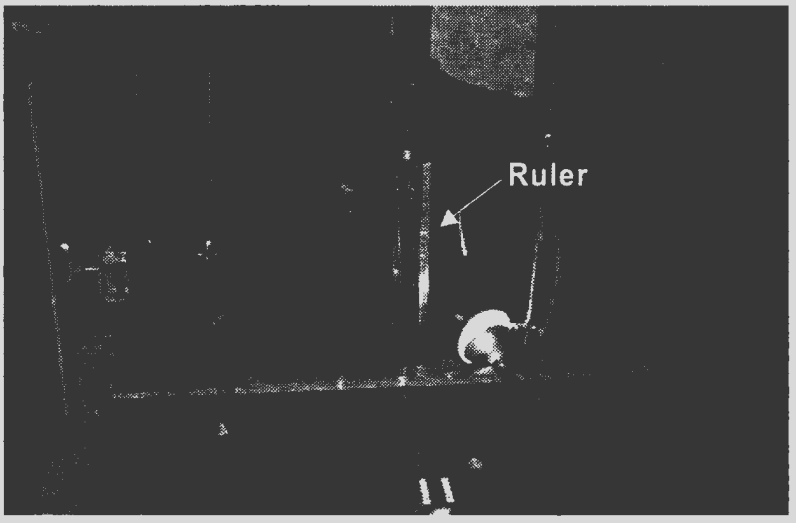

Figure 4.10 - Laser light sheet and illuminated calibration scale

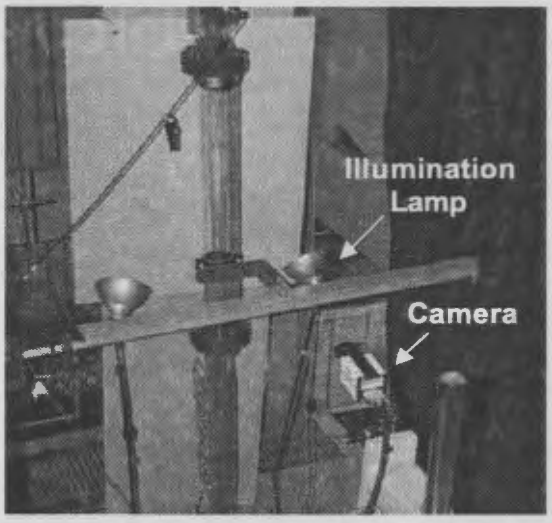

Figure 4.11 - Flow visualization test section

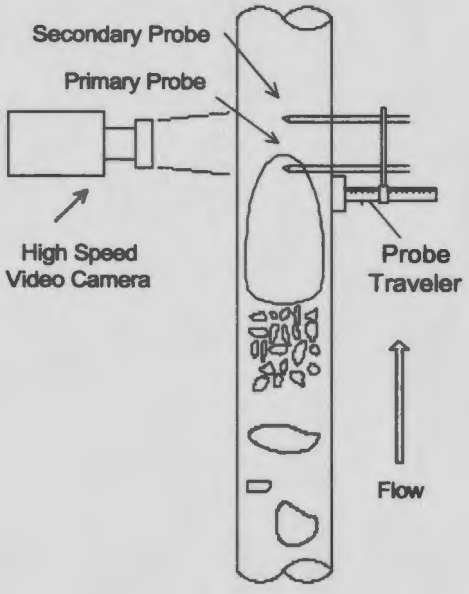

Figure 4.12 - Schematic of hot-film and flow visualization test section

The normal location of the hot-film test section is immediately upstream of the flow visualization test section. However, for investigating the dynamic hot-film response to a passage of a gas slug, the camera was pointed at the hot film probes (Figure 4.12).

The hot-films are mounted on a traverse that allows the probes to be moved along the pipe diameter with an accuracy of ±0.01-mm (accuracy of the traverse).

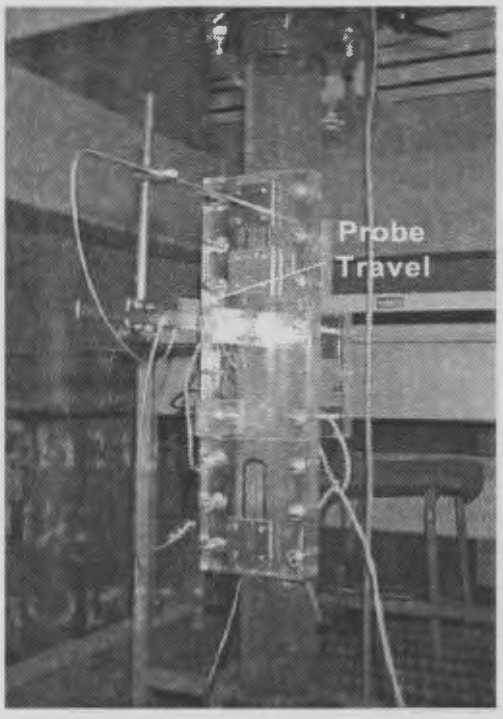

Figure 4.13 - Hot-film test section

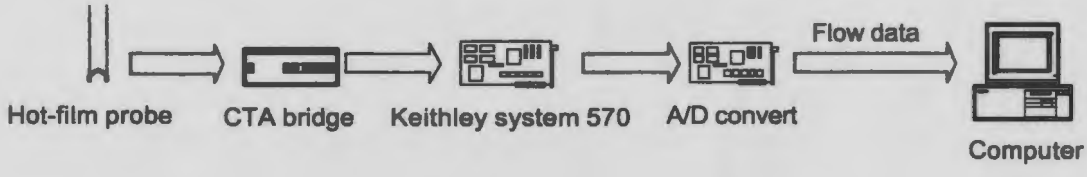

Figure 4.14 - Hot-film anemometry data acquisition system

Figure 4.13 provides a picture of the hot-film test section. Heavy-coated cylindrical DANTEC 55R11 hot-film probes, operated at an overheat ratio of 1.1 are used with a DISA 55M10 Constant Temperature Anemometer (CTA) system. The hot-film

signals are sampled directly at 7000Hz into a dedicated personal computer through a KEITHLEY S570 A/D converter (Figure 4.14). To obtain simultaneous flow visualization and hot-film measurements, a common external trigger circuit with a built-in time delay on one channel was designed to synchronize the two measurement systems. Upon activation of the hot-film data acquisition system, the flow visualization system is triggered after a pre-determined delay. The shift in the two sets of data is aligned exactly during post-processing by focusing on key identifiable characteristics of the flow.

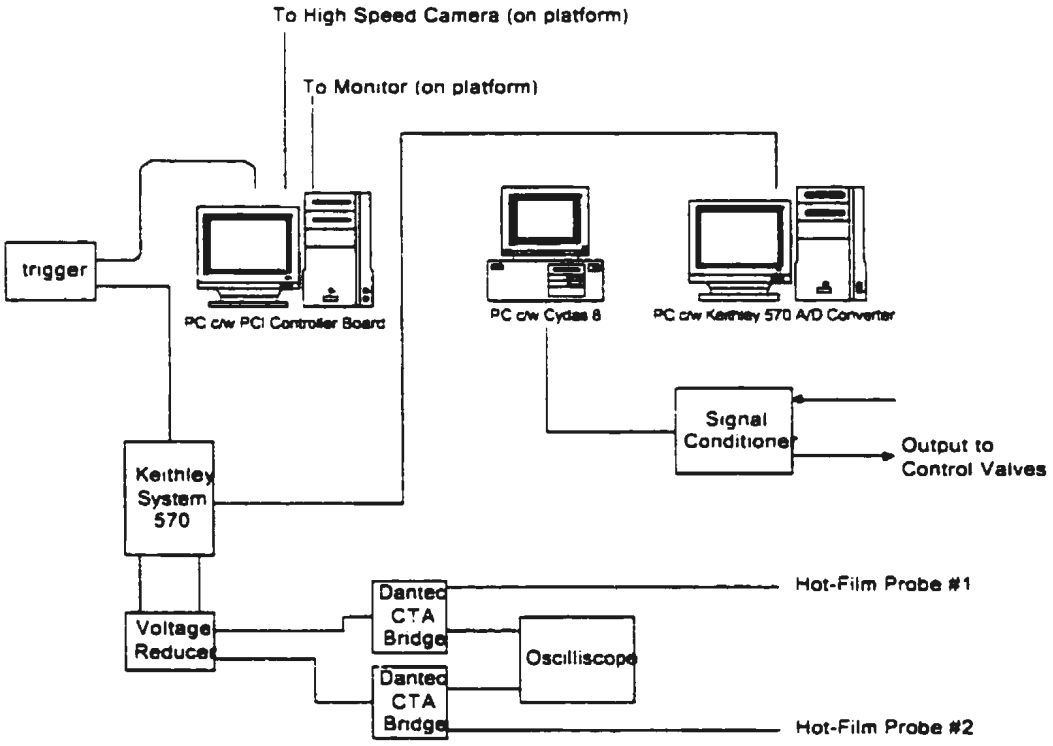

Figure 4.15 - Schematic of flow loop control/data acquisition and hot-film and flow visualization systems

The flow measurement and control systems are controlled by three personal computers (Figure 4.15). Figure 4.16 provides a pictorial description of this setup.

Figure 4.16 - Control equipment for flow loop, hot-film and flow visualization

4.5 Summarizing Remarks

A multiphase flow loop has been constructed at MUN to investigate oil-water-gas flows. The flow loop is instrumented with accurate flow rate, pressure and temperature measurement systems. Hot-film and high-speed flow visualization measurement systems are equipped on the flow loop to obtain the quantitative information about each flow component. A fully integrated computerized system handles the system control and the data acquisition. The MUN flow loop is the first multiphase flow research facility that has been built in the Atlantic Canada region. Its construction makes it possible to conduct multiphase flow related research at MUN, including the research described in this thesis.

Chapter 5

Dimensional Analysis of Two-Phase Flow

The flow pattern map and interfacial area concentration are two important parameters required to determine the closure relations of two-phase flow models. Although various models have been proposed as discussed in chapter 2, no reliable model exists for determining the flow patterns and phase interfacial area. A great number of models for flow pattern and phase interfacial area concentration are expressed in dimensional form in the literature. The use of dimensional parameters in these models makes them inappropriate for use under different circumstances. To overcome this, dimensional analysis is introduced in this chapter to simplify the problem and to provide guidelines for planning experiments and presenting results by formulating the functional equations for flow pattern and phase interfacial area concentration.

5.1 Introduction to Dimensional Analysis

It is extremely difficult to obtain a complete analytical solution to two-phase flow patterns due to the complex nature of the flow. A partial solution can, however, be obtained using dimensional analysis. Although partial analysis does not provide a complete solution, it can tremendously simplify the problem and provides rules for

modeling the system concerned. Methods of partial analysis are based on dimensional or similarity approaches, which result in a dimensionless functional equation. This equation can be employed as a guideline for planning experimental measurements and analyzing results.

Dimensional analysis is based on the principle of Fourier's dimensional homogeneity theory (Sharp 1981). However, conventional methods of dimensional analysis suffer from several disadvantages. The most significant drawback is, perhaps, that little facility is provided for guiding the analysis towards a convenient, rather than merely a correct, solution (Sharp 1973). Another disadvantage is that the complete range of solutions is not readily apparent. Although compounding can be used to find the final convenient solution to the problem, the procedure is often a tedious approach, especially when a large number of variables is involved.

The synthesis method of Barr (1969, 1971) greatly overcomes these disadvantages. Barr formulated an intermediate stage between the initial functional equation and the final dimensionless formula by introducing linear proportionalities. Linear proportionalities, together with any relevant lengths of the system, are formulated from the initial functional equation to produce a homogeneous equation with dimension of length. The most convenient solution to the problem can then be obtained by compounding these dimensional length terms. The introduction of linear proportionalities as the intermediate stage provides more freedom and choices in formulating the final dimensionless equation. The linear proportionalities are found in a similar manner to that used in the Buckingham method (Buckingham 1914). However, the variables are combined to form terms with dimension of length rather than immediate dimensionless

numbers. For the purpose of formulating the linear proportionalities, density may be eliminated from the list of variables and included as required because density is not a relevant (independent) factor unless it is combined with another variable that has a mass dimension (Sharp 1975). In general, if there are m terms to be combined (terms excluding density and length) it is possible to form ${}_2C_m$ linear proportionality terms, of which only $(m-1)$ terms are required in formulating any correct dimensionally homogenous equation (Sharp 1981). The final dimensionless functional equation can then be formulated through compounding this dimensionally homogenous equation. Apparently, the linear proportionalities introduce redundant dimensional length terms. The redundancy provides more choices and freedom at the final compounding stage. The synthesis method is employed to derive the appropriate two-phase flow pattern mapping parameters in this thesis.

5.2 Dimensional Analysis of Flow Pattern Map

The initial step of the analysis is to establish the system functional equation. The gravitational effect is significant in vertical slug flows. Phase flow rates and fluid physical properties, such as density, viscosity and pipe geometry also need to be included in the functional equation. Effects of pressure and temperature on the flow patterns are incorporated through density and viscosity changes, and hence need not be included directly in the functional equation. Surface tension is speculated to play a role in bubble formation, and is included in the equation. Two-phase flow is a densimetric phenomenon because there are two fluids involved. The density difference requires modifying the gravitational acceleration. Consider the case where gas bubbles and slugs are surrounded

by liquid in the pipe. The weight of gas bubble can be approximated as $\rho_G g d^3$, where d is the gas bubble characteristic diameter. The upthrust on a gas bubble immersed in the liquid is approximately $\rho_L g d^3$, therefore, the reduced gravity of the air bubble or plug is:

$$g_G = \frac{(\rho_L - \rho_G) g d^3}{\rho_G d^3} = \frac{\Delta\rho}{\rho_G} g$$

In the case where the gas is the continuous phase, the reduced gravity for the liquid is:

$$g_L = \frac{(\rho_L - \rho_G) g d^3}{\rho_L d^3} = \frac{\Delta\rho}{\rho_L} g$$

In bubble and slug flows, the reduced gravity is relevant only for the gas phase since liquid is the continuous phase. Therefore, the flow pattern functional equation is:

$$Pattern(bubble, slug) = \phi(q_G, q_L, \mu_G, \mu_L, \rho_G, \rho_L, g, g_G, \sigma_L, L, D) \qquad (5\text{-}1)$$

where q is the volume flow rare, μ is the dynamics vicosity, σ is the surface tension, D is the pipe diameter, and L is the flow pattern observation location. The subscripts G and L indicate gas and liquid phases, respectively. One of the densities or gravities is redundant in this functional equation. Its inclusion in the equation is to facilitate the derivation of the linear proportionalities. Using the synthesis method, the flow pattern can be expressed in terms of linear proportionalities as:

$$Pattern(buble,slug) = \phi(\frac{q_G^{2.5}}{g_G^{1.5}}, \frac{q_L^{2.5}}{g_G^{1.5}}, \frac{q_G^{2.5}}{g^{1.5}}, \frac{q_L^{2.5}}{g^{1.5}}, \frac{q_G}{v_G}, \frac{q_G}{v_L}, \frac{q_L}{v_G}, \frac{q_L}{v_L}, \frac{v_G^{2.3}}{g_G^{1.3}}, \frac{v_G^{2.3}}{g^{1.3}}, \frac{v_L^{2.3}}{g^{1.3}}, \frac{v_L^{2.3}}{g_G^{1.3}},$$

$$\frac{\sigma_L^{1.2}}{\rho_L^{1.2} g^{1.2}}, \frac{\sigma_L^{1.2}}{\rho_G^{1.2} g^{1.2}}, \frac{\sigma_L^{1.2}}{\rho_G^{1.2} g_G^{1.2}}, \frac{v_L^2 \rho_L}{\sigma_L}, \frac{v_G^2 \rho_G}{\sigma_L}, \frac{v_L^2 \rho_G}{\sigma_L}, \frac{v_G^2 \rho_L}{\sigma_L}, \frac{q_L \rho_L^{1.2}}{\sigma_L^{1.2}}, \frac{q_L \rho_G^{1.2}}{\sigma_L^{1.2}}, \frac{q_G \rho_L^{1.2}}{\sigma_L^{1.2}}, \frac{q_G \sigma_G^{1.2}}{\sigma_L^{1.2}} L, D) \quad (5\text{-}2)$$

Equation 5-2 is an exhaustive list of all the possible linear proportionalities that can be derived. Since there are seven terms involved in forming the linear proportionalities (excluding densities and lengths), six terms (7 – 1 = 6) need to be selected to formulate the dimensionally homogenous equation. In choosing the linear proportionalities, it is necessary to ensure that every variable must be included at least once in the functional equation (Sharp 1981).

$$Pattern(bubble,slug) = \phi(\frac{q_L^{2.5}}{g^{1.5}}, \frac{q_G^{2.5}}{g^{1.5}}, \frac{q_G}{v_G}, \frac{q_L}{v_L}, \frac{q_L^{2.5}}{g_G^{1.5}}, \frac{\sigma_L^{1.2}}{\rho_L^{1.2} g^{1.2}}, L, D) \quad (5\text{-}3)$$

Consequently, the final dimensionless functional equation after compounding is:

$$Pattern(bubble,slug) = \phi(\frac{q_G}{q_L}, \frac{q_L}{D^{5/2} g^{1/2}}, \frac{q_L}{v_L D}, \frac{q_G}{v_G D}, \frac{\Delta\rho}{\rho_G}, \frac{\sigma_L^{3/2}}{\rho_L^{3/2} g^{1/2} v_L^2}, \frac{L}{D}) \quad (5\text{-}4)$$

In churn flow, both the gas and liquid reduced gravitational constants must be included in the flow pattern functional equation, because the flow alternates between gas and liquid continuous flows. The dimensional functional equation is:

$$Pattern(churn) = \phi(q_G, q_L, \mu_G, \mu_L, \rho_G, \rho_L, g_L, g_G, \sigma_L, L, D) \tag{5-5}$$

The final dimensionless functional equation can be obtained in a similar manner to equation 5-4 as:

$$Pattern(churn) = \phi(\frac{q_G}{q_L}, \frac{q_L}{D^{5/2} g_L^{1/2}}, \frac{q_L}{\nu_L D}, \frac{q_G}{\nu_G D}, \frac{\rho_L}{\rho_G}, \frac{\sigma_L^{3/2}}{\rho_L^{3/2} g^{1/2} \nu_L^2}, \frac{L}{D}) \tag{5-6}$$

Gas is the continuous phase in annular flow, and therefore, only g_L must be included in the annular flow pattern dimensional functional equation:

$$Pattern(annular) = \phi(q_G, q_L, \mu_G, \mu_L, \rho_G, \rho_L, g_L, g, \sigma_L, L, D) \tag{5-7}$$

The resultant dimensional functional equation is:

$$Pattern(annular) = \phi(\frac{q_G}{q_L}, \frac{q_L}{D^{5/2} g_L^{1/2}}, \frac{q_L}{\nu_L D}, \frac{q_G}{\nu_G D}, \frac{\Delta\rho}{\rho_L}, \frac{\sigma_L^{3/2}}{\rho_L^{3/2} g^{1/2} \nu_L^2}, \frac{L}{D}) \tag{5-8}$$

In all three flow pattern functional equations (equations 5-4, 5-6 and 5-8), $\frac{q_L}{\nu_L D}$ and $\frac{q_G}{\nu_G D}$, which are equivalent to the liquid and gas phase Reynolds numbers, are very likely not to be important, because the flows of interest are turbulent. The variation in surface tension, viscosity and density for a specific liquid is negligible, therefore,

$\frac{\sigma_L^{3/2}}{\rho_L^{3/2} g^{1/2} \nu_L^2}$ is more or less constant for a specific liquid and can be ignored from the flow pattern functional equation. However, the importance of this term for different liquids needs to be assessed. It is tentatively assumed that this term is not critical in defining the flow pattern. This validation of this assumption will be justified in chapter 7.

The parameter $\frac{L}{D}$ is important for a developing flow, and must be equal in each individual experiment in order to satisfy geometric similarity (Sharp 1981). However, this restriction will be relaxed for fully developed flows where the flow patterns remain invariant with distance. Bubble, slug and churn flows may depend on temperature and pressure because the dimensionless density, $\frac{\Delta\rho}{\rho_G} = \frac{\rho_L}{\rho_G} - 1$, of the bubble and slug flows, and $\frac{\rho_L}{\rho_G}$ of the churn flow are sensitive to the individual phase density change. The similarity requirement of the density terms seems to be stringent. It requires that not only the dimensionless density must be equal in each experiment but also the individual phase density must stay constant throughout the experiment. This postulation, however, needs to be verified by experiments. On the contrary, the dimensionless density term, $\frac{\Delta\rho}{\rho_L} = 1 - \frac{\rho_G}{\rho_L}$, of the annular flow indicates that even a significant change of gas density only results in a negligible change to it as a whole. The annular flow is, therefore, a temperature and pressure insensitive flow. Provided that the density similarity is satisfied, for fully developed, turbulent vertical-up gas liquid flows, $\frac{q_G}{q_L}$ and $\frac{q_L}{D^{5/2} g^{1/2}}$ are the only

dominant terms for bubble, slug and annular flows, and $\frac{q_G}{q_L}$ and $\frac{q_L}{D^{5/2} g_L^{1/2}}$ for churn flow. In order to keep the parameters consistent, $\frac{q_L}{D^{5/2} g^{1/2}}$ instead of $\frac{q_L}{D^{5/2} g_L^{1/2}}$ is used as the churn flow plotting parameters. The error incurred by this change is negiligible, because of the minor difference between g and g_L. Therefore, $\frac{q_G}{q_L}$ and $\frac{q_L}{D^{5/2} g^{1/2}}$ are the final plotting parameters for all two-phase gas-liquid flow patterns. The parameter $\frac{q_L}{D^{5/2} g^{1/2}}$ is the Froude number, and can be interpreted as the ratio of inertial to gravitational forces. It should be an important parameter in vertical-up two phase flow where gravity plays a significant role. The plotting parameters suggest that the flow patterns are primarily dependent on the ratio of gas-to-liquid flow rate and the ratio of the inertial to gravity forces.

5.3 Dimensional Analysis of Interfacial Area Concentration

The important dimensionless parameters that determine the interfacial area concentration can be derived in a similar manner to the dimensionless flow pattern map parameters. For gas-liquid two-phase slug flow, the phase interface can exist in a wide variety of forms, depending on the flow rates and physical properties of the phases, as well as on the geometry and inclination of the tube (McQuillan and Whalley 1985). Therefore, for vertically upward slug flow, the functional equation for the interfacial area concentration, a_i, can be expressed as:

$$a_i = \phi(q_L, q_G, \mu_G, \mu_L, \rho_G, \rho_L, g, g_G, \sigma_L, D) \tag{5-9}$$

Using the synthesis method, the linear proportionalities equation is formed as:

$$\frac{1}{a_i} = \phi\left(\frac{q_G^{2.5}}{g_G^{1.5}}, \frac{q_L^{2.5}}{g_G^{1.5}}, \frac{q_G^{2.5}}{g^{1.5}}, \frac{q_L^{2.5}}{g^{1.5}}, \frac{q_G}{\nu_G}, \frac{q_G}{\nu_L}, \frac{q_L}{\nu_G}, \frac{q_L}{\nu_L}, \frac{\nu_G^{2.3}}{g_G^{1.3}}, \frac{\nu_G^{2.3}}{g^{1.3}}, \frac{\nu_L^{2.3}}{g^{1.3}}, \frac{\nu_L^{2.3}}{g_G^{1.3}}, \frac{\sigma_L^{1.2}}{\rho_L^{1.2} g^{1.2}},\right.$$

$$\left.\frac{\sigma_L^{1.2}}{\rho_G^{1.2} g^{1.2}}, \frac{\sigma_L^{1.2}}{\rho_G^{1.2} g_G^{1.2}}, \frac{\nu_L^2 \rho_L}{\sigma_L}, \frac{\nu_G^2 \rho_G}{\sigma_L}, \frac{\nu_L^2 \rho_G}{\sigma_L}, \frac{\nu_G^2 \rho_L}{\sigma_L}, \frac{q_L \rho_L^{1.2}}{\sigma_L^{1.2}}, \frac{q_L \rho_G^{1.2}}{\sigma_L^{1.2}}, \frac{q_G \rho_L^{1.2}}{\sigma_L^{1.2}}, \frac{q_G \sigma_G^{1.2}}{\sigma_L^{1.2}}, D\right)$$

(5-10)

Seven independent terms are involved in formulating the linear proportionalities. Six terms are, therefore, needed to formulate the dimensionally homogenous equation, along with the length term and interfacial area concentration. The resultant dimensionally homogenous equation is:

$$\frac{1}{a_i} = \phi\left(\frac{q_L^{2.5}}{g^{1.5}}, \frac{q_G^{2.5}}{g^{1.5}}, \frac{q_G}{\nu_G}, \frac{q_L}{\nu_L}, \frac{q_L^{2.5}}{g_G^{1.5}}, \frac{\sigma_L^{1.2}}{\rho_L^{1.2} g^{1.2}}, D\right) \tag{5-11}$$

The dimensionless functional equation is formulated by compounding as:

$$a_i D = \phi\left(\frac{\nu_G}{\nu_L}, \frac{\nu_L}{D^{3.2} g^{.2}}, \frac{q_L}{q_G}, \frac{q_L}{\nu_L D}, \frac{\Delta\rho}{\rho_G}, \frac{\sigma_L}{g\Delta\rho D^2}\right) \tag{5-12}$$

The interfacial area concentraion is, therefore, a function of the viscosity ratio, Reynolds-Froude Number ($\frac{v_L}{D^{3/2} g^{1/2}}$), volume flow ratio, Reynolds number of the liquid phase, Froude-Weber number ($\frac{\sigma_L}{g\Delta\rho D^2}$), and pipe diameter. Compared with the dimensionless equation proposed by Zeitoun et al. (1994), three additional terms are found in equation 5-12, because the physical properties of the gas phase are included in this analysis. The additional terms are viscosity ratio, $\frac{v_L}{D^{3/2} g^{1/2}}$ and dimensionless density. The addition of these terms should improve the portability and applicability of equation 5-12 over the equation proposed by Zeitoun et al. (1994).

5.4 Summarizing Remarks

In summary, the dimensionless flow pattern map and interfacial area concentration equations for vertical-up gas-liquid flows have been formulated using dimensional analysis. The use of dimensionless parameters leads to more portable and robust models, which will be developed in this thesis.

Chapter 6

Signal Analysis and Data Reduction

Hot-film anemometry is used primarily to obtain measurements of void fraction, slug/bubble velocities, slug/bubble dimensions, slug/bubble frequencies and interfacial area concentration. The first part of this chapter describes the dynamic response of hot-film to the passage of a gas slug. This information provides the basis for developing the signal processing techniques to obtain the desired flow information from the hot-film signal in this thesis. The results from hot-film anemometry are corroborated using a high-speed quantitative flow visualization system.

6.1 Data Reduction for Multiple Velocities

Direct measurement of the gas and liquid velocities from a single hot-film probe is impractical with the current MUN flow loop configurations. The low overheat ratio makes the hot-film calibration very sensitive to variations in the fluid temperature. This is evident in the calibration curves obtained over a period of time (Figure 6.1). The time interval between each calibration curve is 1.5 hours, and the temperature increase of the liquid (water) is due to the continous pump operation. The calibration drift results in a velocity misinterpretation on the order of 1 *m/s* per °C temperature change.

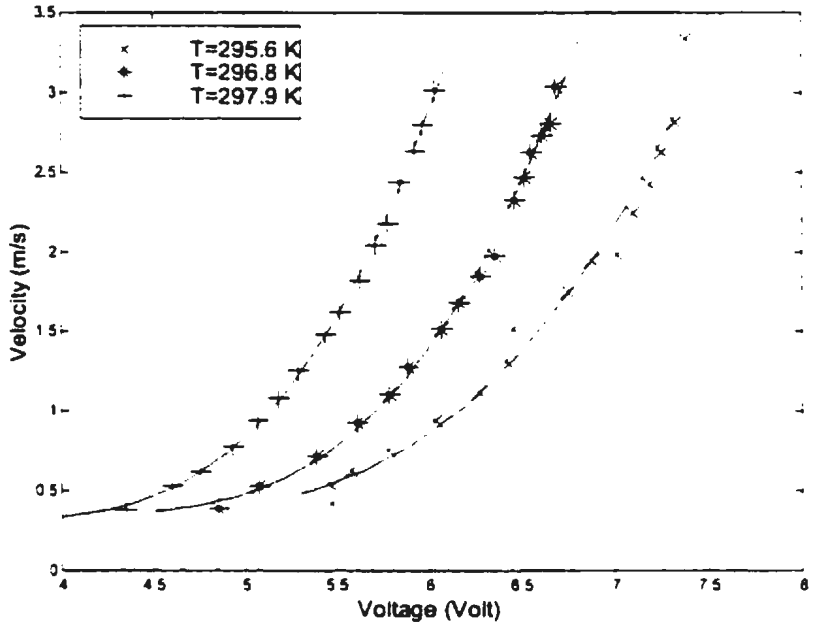

Figure 6.1 - Calibration curves obtained from MUN flow loop

Also, the process of the residual liquid film evaporating on the probe during the passage of a gas bubble/slug is extremely difficult to model. A dual-probe technique can overcome these difficulties and was employed to measure the gas bubble velocity in this research. Figure 6.2 schematically illustrates the principle of this technique. Two hot-film probes are spaced along the steamwise direction. The time-difference-of-arrival of the gas bubbles at the two probe locations can be estimated from a cross correlation between the signals from the probes if the distance between them is properly chosen. A series of tests was performed to determine the appropriate probe distance, indicating that a probe distance of 20 mm is optimal. This spacing ensures good accuracy while preserving reasonably strong cross correlation.

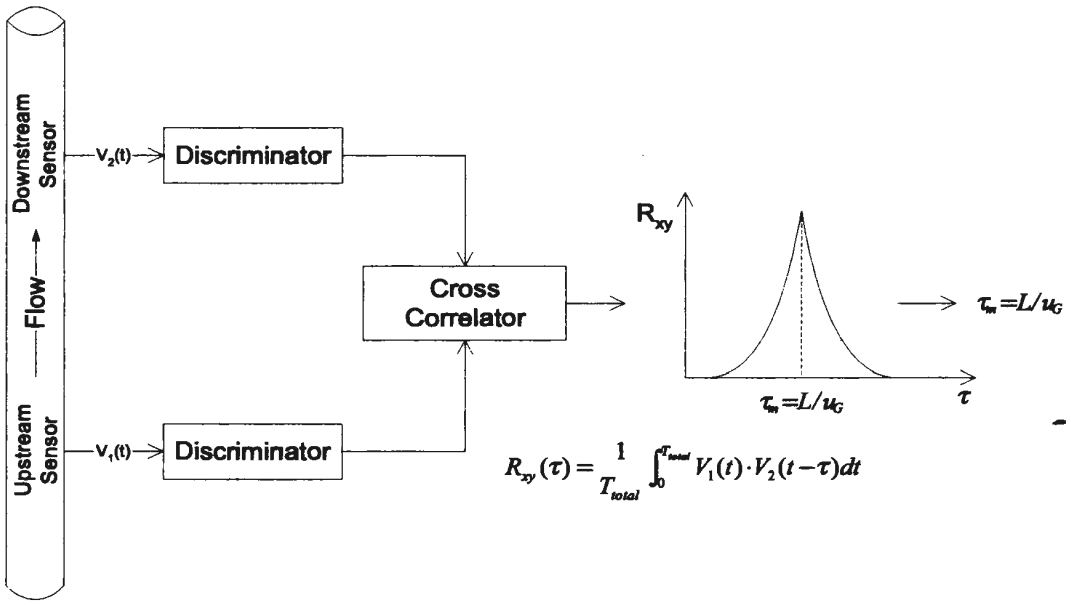

Figure 6.2 - Schematic of velocity estimation procedure

The sampling rate for each hot-film probe is 7 kHz. A 300-second sampling time was chosen to obtain statistically steady flow results. Multiple velocities corresponding to different bubble size groups can be estimated through selective discrimination of the signal to reflect the different bubble size groups. The principle of this technique is implemented in five steps:

1. Signal decomposition using wavelet transforms to remove high-frequency signal noise.
2. Identification of gas slugs and bubbles using an amplitude and first-order time derivative of the signal.
3. Discrimination of the signal into signals corresponding to different bubble size groups.
4. Cross-correlation of the discriminated signals from the two sensors to obtain the time-difference-of-arrival of the gas bubbles at the sensor locations.

5. Estimation of slug/bubble velocities from the time-difference-of-arrival and the distance between the sensors, and consequently slug/bubble sizes, slug/bubble void fraction and slug/bubble frequencies

6.2 Dynamic Response of Hot Film to the Passage of Gas Bubble and Slug

The distinct signal response of the hot-film to the gas and liquid phases makes it possible to discriminate between the two phases. In order to accurately discriminate the hot-film signals into the gas and liquid phases, the dynamic response of the probe to the passage of a gas slug/bubble needs to be clearly understood. This was investigated using simultaneous high-speed flow visualization (500 fps, 320×280 pixels) and hot-film measurements. The detailed experimental setup was illustrated in Figure 4.12 in chapter 4.

Figure 6.3 shows a typical hot-film trace as a gas slug passes over the probe, with the corresponding flow images. The field of view of the video is about 7×7 inches. However, the images are cropped to 7×3 inches for better display. The dynamic response of the probe is similar to that described by Farrar and Bruun (1989) for a gas bubble as discussed in chapter 2. As the slug front approaches the probe (A), the signal output increases because the liquid just upstream of the slug is moving with a slightly greater velocity than the average liquid velocity. This velocity increase can be explained with the assistance of Figure 6.4. For liquid velocity of U_2 and gas slug velocity of U_1, where U_1 is greater than U_2 due to buoyancy (Figure 6.4a), the relative liquid velocity upstream of the slug against the gas slug is U_2-U_1. By conservation of mass, the relative liquid velocity in

the shaded region shown in Figure 6.4b must be higher than U_2-U_1 due to the reduced cross sectional area.

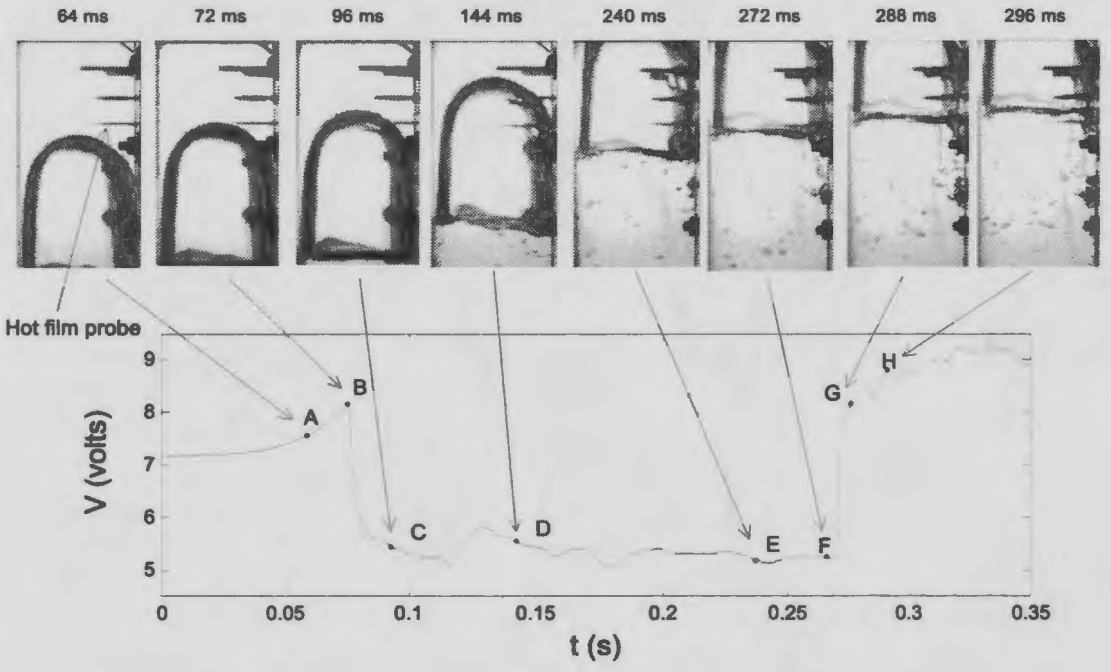

Figure 6.3 - Dynamic hot-film response to a passage of a gas slug

The hot-film signal continues to increase until the probe pierces the slug (B), and this event is accompanied by a small overshoot in the hot film signal. A steep drop (from B to C) in the signal is followed due to the rapid evaporation of the liquid film on the sensor surface. At locations D and E the probe is in the gas phase and the signal corresponds to that of the gas phase, provided that the liquid film on the sensor is fully evaporated. When the back of the slug arrives at the probe, the rapid covering of the probe with the liquid results in a steep rise in the signal output (from F to G). At location H, the probe is in the wake region of the slug. The two events, B and F, corresponding to the slug front and back hitting the sensor, need to be clearly identified to localize the slug

passage. The two events are associated with a sign change in the time derivative of the signal and this feature was used to determine the location of the slug front and back.

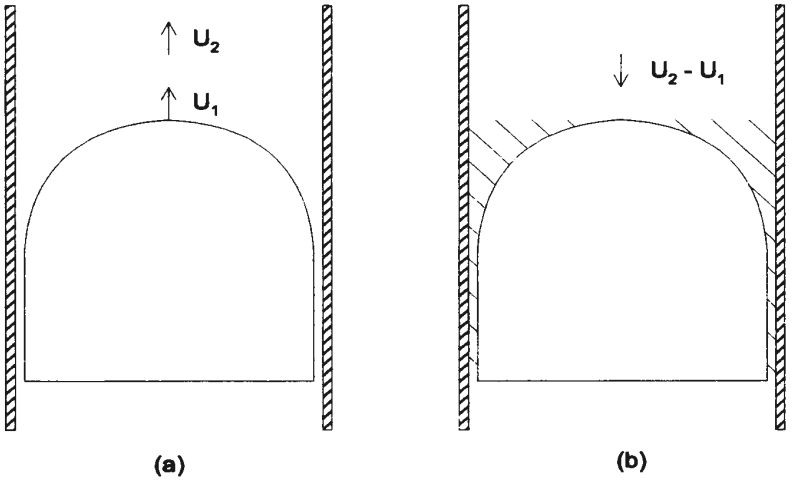

Figure 6.4 - High velocity region just upstream of a gas slug

6.3 Schemes for Discriminating Gas and Liquid

A good understanding of the dynamic response of hot-film to the passage of gas bubbles and slugs allows accurate quantitative information to be obtained from the hot-film signals. A combined amplitude and first-order time derivative method was developed to identify the two events B and F (Figure 6.3). The amplitude threshold is calculated using the signal amplitude probability density function (Farrar et al. 1995). Once the intersection points of the signal with the threshold are located, a backward searching scheme is used to locate the front and back of the bubble/slug from the signal. The sign change in the first-order time derivative is associated with the two events (see Figure 6.3). The improved phase identification scheme is deemed to be simpler and more accurate than the thesholding method originally proposed by Farrar et al. (1995), in which a subjectively selected threshold of the first-order time derivative of the signal was

used. It also avoids the tedious trial and error process that must be performed when selecting the threshold, and hence is much easier to use.

6.4 Signal Discretization and Void Fraction Estimation

Once the events associated with the front and back of the bubbles/slugs hitting the probe are correctly identified in the hot-film signal, the signal can be discretized into a phase indicator function, in which *1* indicates the gas phase, while *0* indicates the liquid phase. A sample flow condition is used throughout this chapter to assist the description of the entire data reduction process. The sample flow is an air-water slug flow with the flow conditions presented in Table 6.1.

Table 6.1 Sample Flow Condition

U_L (m/s)	U_G (m/s)	β %	Flow Pattern
0.97	0.23	19.2	Slug

The hot-film signal of this sample flow over a representative one-second time interval is provided in Figure 6.5. The occurrences of the gas bubbles and slugs in Figure 6.5a are reflected and localized accurately by the phase indicator function (Figure 6.5b). Since the time fraction and void fraction are equivalent parameters (see equation 2-13), the void fraction, ε, can be determined from the phase indicator function as:

$$\varepsilon(r) = \alpha_G(r) = \frac{\sum t_G(r,t)}{T(r)} = \frac{\int_0^t \alpha_G(r,t)dt}{T(r)} \qquad (6\text{-}1)$$

where t_G is the time when the probe detects the gas phase, T is the total measurement time, and α_G is the phase indicator function.

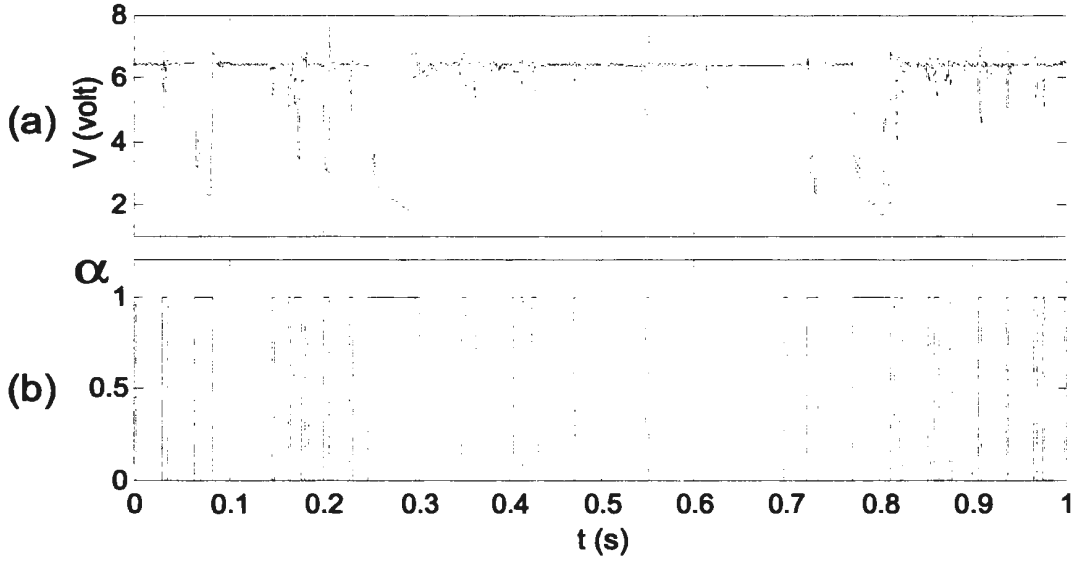

Figure 6.5 - Hot-film signal and its phase indicator function: (a) Hot-film signal; (b) Phase indicator function

The local void fraction distribution is illustrated in Figure 6.6. The data in this figure are the average of two independent measurements from the two probes in the streamwise direction. The local void fractions calculated from the two probes are within ±5% of each other, indicating that the influence of the upstream probe on the downstream probe is small.

The void fraction is a maximum in the central region of the pipe and decreases rapidly close to the wall. The void fraction is approximately constant up to r/R=0.7. It shows a profile similar to those obtained by Welle (1985) and Cheng et al. (1998). The average or global void fraction of the flow is obtained by integrating the local void fraction over the cross section of the pipe. The integration is performed by assuming

radial symmetry since the flow is vertically-upwards. The average void fraction for a circular pipe is calculated as:

$$\bar{\varepsilon} = \frac{\int_0^R \varepsilon(r)dA}{A} = \frac{2 \cdot \int_0^R \varepsilon(r) \cdot r dr}{R^2} \tag{6-2}$$

where A is the pipe cross sectional area, and R is the pipe radius. The resultant global void fraction (ε = 19.0%) is found to be less than the phase volume fraction (β = 19.2%) in this instance, and is consistent with the analysis.

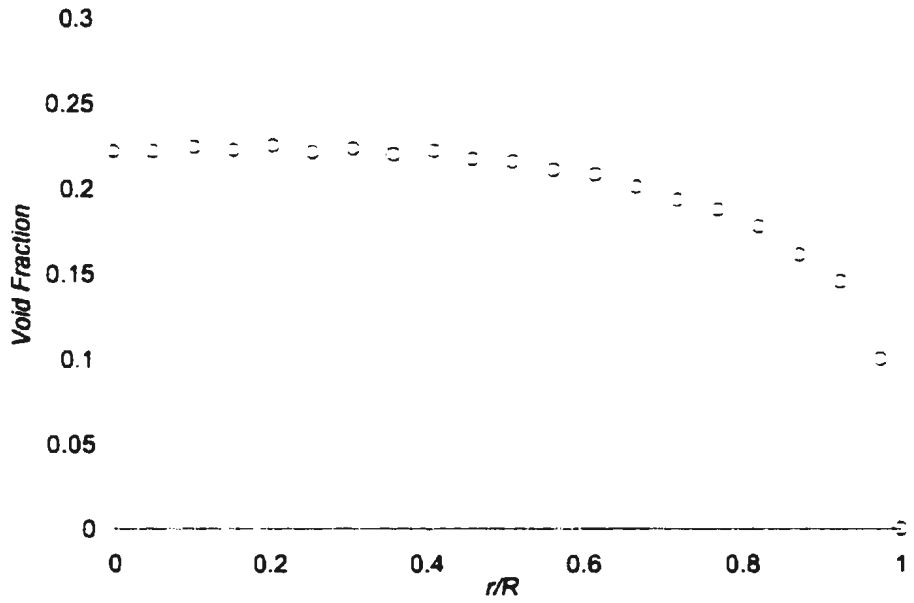

Figure 6.6 -Void fraction distribution for all bubbles

6.5 Wavelet Signal Decomposition

The passage of a gas slug/bubble over the hot-film is accompanied by a sudden decrease in the signal, because of the reduced heat transfer from the sensor to the fluid.

Intuitively, it may seem plausible that the signal could be suitably band-pass filtered to elicit the distinguishing features of the slugs and bubbles and remove noise. However, the signal of bubble/slug flow (see Figure 6.5a) is non-stationary in nature. Classical Fourier filtering techniques are not suitable, because of the different phase shifts they impose on the different frequency components. Consequently, the cross-correlation will not reflect the true time shift between the signals. Unlike Fourier transforms, wavelet transforms are well suited to the analysis of non-stationary signals. In wavelet analysis, both the time and frequency information is well preserved, and hence, accurate temporal localization of each event is possible; in Fourier analysis, the time information is lost when the signal is transformed from the time domain to the frequency domain. This time information is generally not important when dealing with stationary signals where the frequency content of the signal does not change significantly over time. When the signal is non-stationary, a better physical understanding of the signal can only be obtained if its frequency components are localized in time.

Short-Time Fourier Transforms (STFT) permits the signal to be represented as a function of time and frequency by analyzing the signal over a small time window. STFT provides both temporal and frequency information on signal events. However, this information has limited time and frequency resolution that is constrained by the size of the window. Wavelet transforms overcome the resolution problems of STFT to a great extent by enabling a multi-resolution analysis (MRA). The MRA allows the signal to be analyzed at different frequencies with different resolutions. It gives good time resolution and poor frequency resolution at high frequencies, and good frequency resolution and poor time resolution at low frequencies. Therefore, wavelet analysis is well suited for

signals with high frequency components for a short duration and low frequency components for a long duration, which is similar to the hot-film signal for gas-liquid two-phase slug flows.

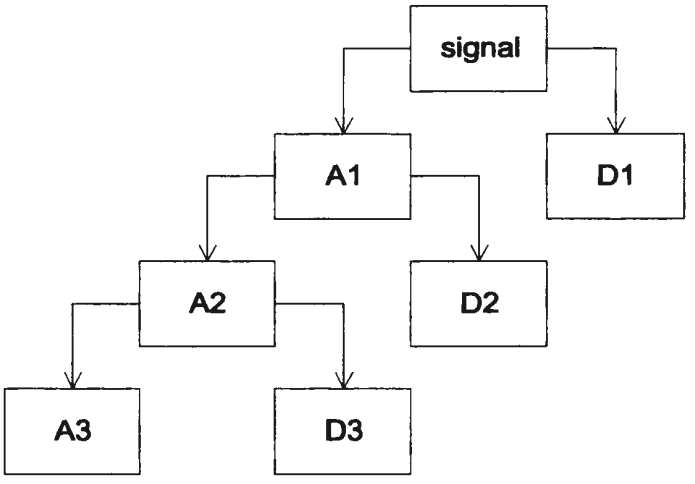

Figure 6.7 - Wavelet decomposition tree showing three level wavelet decomposition

In wavelet analysis, a wavelet prototype function, called mother wavelet, is used to decompose the signal into a scaled and shifted version of the mother function. The wavelet function is a waveform of effectively limited time duration that has an average of zero, and, therefore, allows a better description of local features. The temporal analysis is performed with a contracted, high frequency version of the mother wavelet, while frequency analysis is performed with a dilated low frequency version of the same wavelet (Graps 1995). The signal is often represented in terms of a wavelet expansion.

Wavelet decomposition splits the signal into an approximation and a detail. The approximation is the low frequency components of the signal, and the detail is the high frequency components. The decomposition process can be iterated, with successive approximations being decomposed in turn, so that one signal is broken down into many

lower resolution components, called a wavelet decomposition tree (Figure 6.7), where A refers to approximations and D refers to details. Then the signal is reconstructed from the selected approximations and details to achieve the desired signal filtering. Theoretically, the decomposition process can be processed until the individual details consist of a single sample point. In practice, a suitable number of levels is selected based on the nature of the signal.

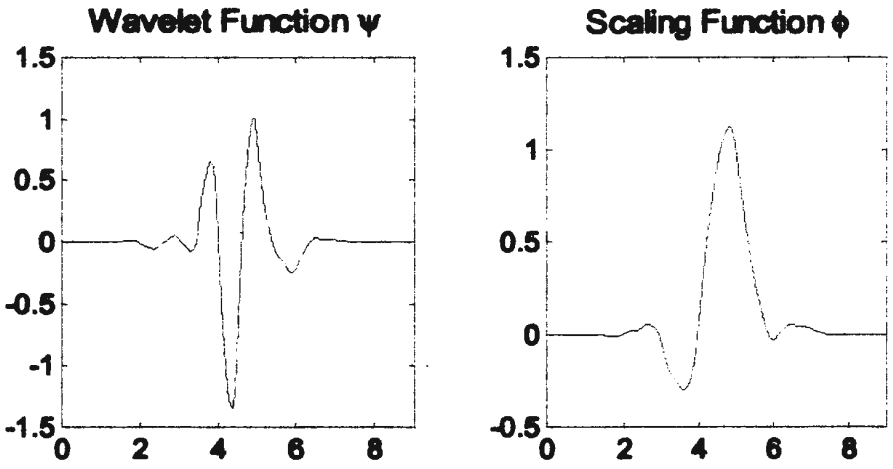

Figure 6.8 - Fifth-order Symlet wavelet function and scale function

In this research, the hot-film signal is decomposed using a fifth-order Symlet wavelet function (Figure 6.8) to facilitate the extraction of the slugs/bubbles. The wavelet decomposition represents the signal as the superposition of the scaled and shifted version of the mother function. A continuous wavelet transform yields localized frequency information on the hot-film output. The mother function is translated over the time domain and dilated over a range of scales. The wavelet transform of the signal in Figure 6.5a is provided in Figure 6.9, along with the original signal. The wavelet transform

indicates the time localized frequency content of the signal and can also be interpreted as the time series record of the signal frequency (or scale). The magnitudes of the resultant coefficients are reflected through a gray level scale. Figure 6.9b shows that the passages of slugs and bubbles are accompanied by a substantial frequency change at these instances. Such characteristics can be used to localize the occurrences of those events. For example, the passages of slugs at 0.248 and 0.772 seconds are precisely reflected in the wavelet transform plot at the same temporal locations.

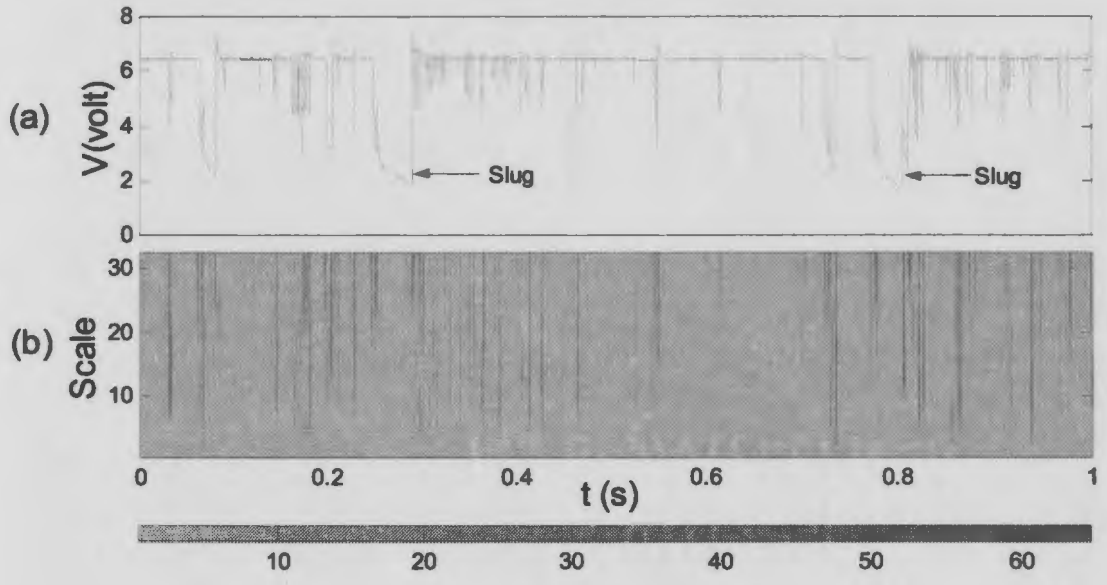

Figure 6.9 - Typical hot-film signal and wavelet transformation: (a) Hot-film signal; (b) Wavelet transformation plot

The wavelet decomposition is used to remove the high frequency noise from the signal. Figure 6.10 show levels two and three of the wavelet decompositions, together with the original signal. While the time information of the local events is well preserved at both levels, the high frequency components (noise) are progressively removed, and the signal of small bubbles is also suppressed. Spectrum analysis is used as an effective tool

to determine the number of wavelet decomposition levels. Figure 6.11 shows the power spectrum density function of the original hot-film signal. Over 92% of the total signal energy is distributed within the frequency range 0 - 437.5 Hz. This low-frequency part of the signal is deemed to characterize its main features. This part of the signal corresponds exactly to the signal approximation remaining in the level-three wavelet decomposition.

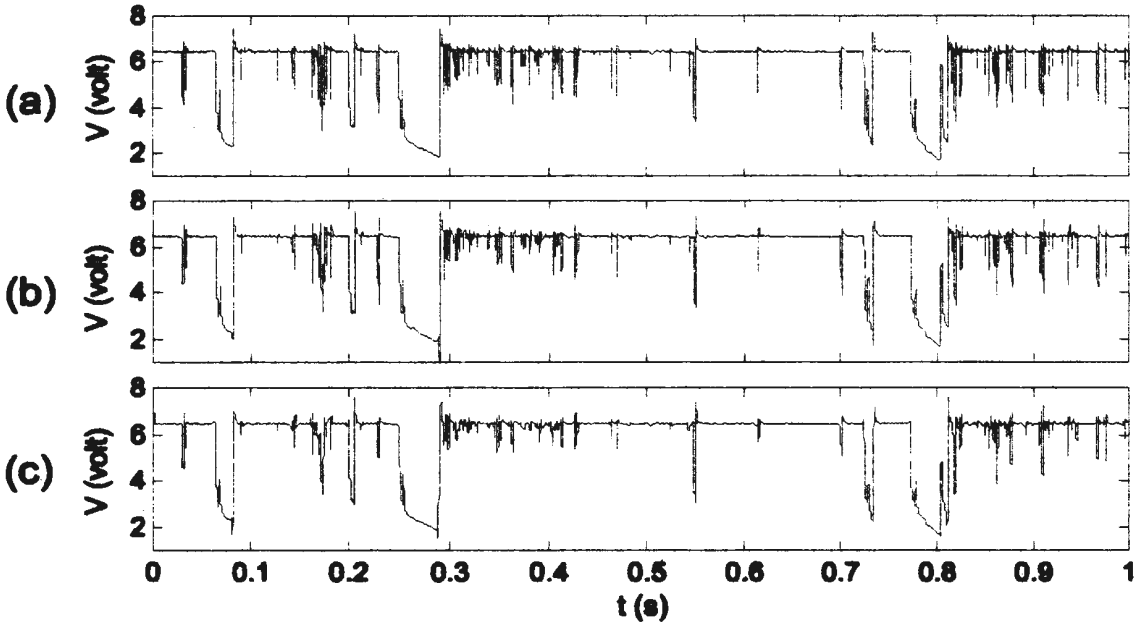

Figure 6.10 - Hot-film signal and corresponding wavelet decomposition approximations (a) Original hot-film signal; (b) Level two wavelet approximation; (c) Level three wavelet approximation

The selection of a three-level decomposition ensures that the dominant features of the signal are well preserved, while a sufficient amount of high-frequency noise is removed. Further decomposition of the signals could possibly distort the gross features of the events and, therefore, is not performed.

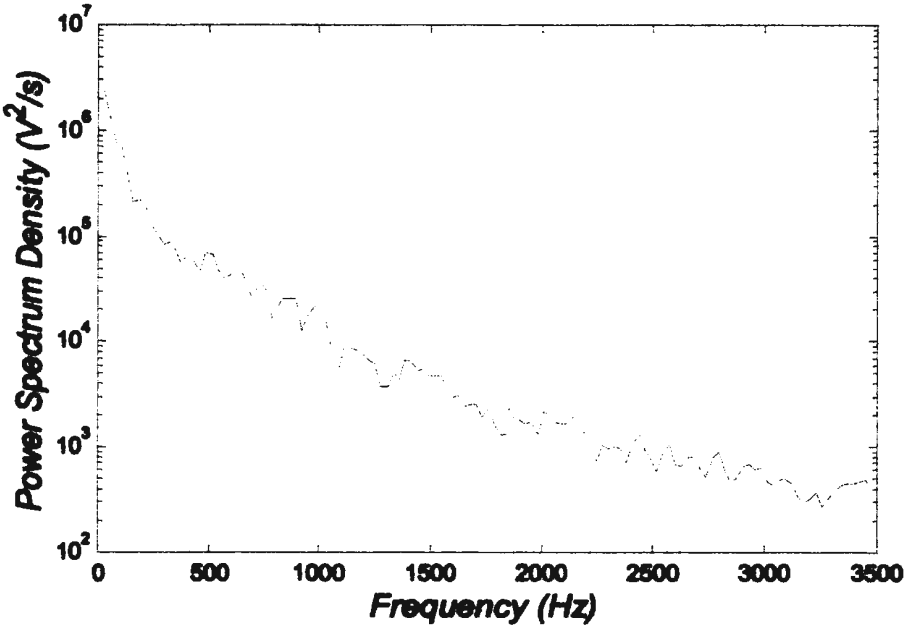

Figure 6.11 - Power spectrum density function of hot-film signal

6.6 Bubble and Slug Velocities

In this study, two velocities corresponding to different slug/bubble size groups have been estimated. The bubble size groups are delineated as slugs if $l/D > 1/2$ and as bubbles otherwise. The bubble/slug discrimination scheme is based on the slug and bubble streamwise length. This dimension is estimated as the product of a velocity calculated from the original signals and the residence time of the probe in the slug/bubble.

The combined amplitude and first-order time derivative technique described in section 6.3 is applied on the resultant level-three approximation to detect slugs and bubbles. These smaller bubbles are reflected as shallow and narrow troughs in the signal. Once the slug signal is extracted, the signal corresponding to the smaller bubbles can be obtained by removing the slugs from the original signal. Consequently, two signals are

obtained, one corresponding to the slug and the other corresponding to the smaller bubbles. Accordingly, two velocities corresponding to the two bubble size groups are estimated.

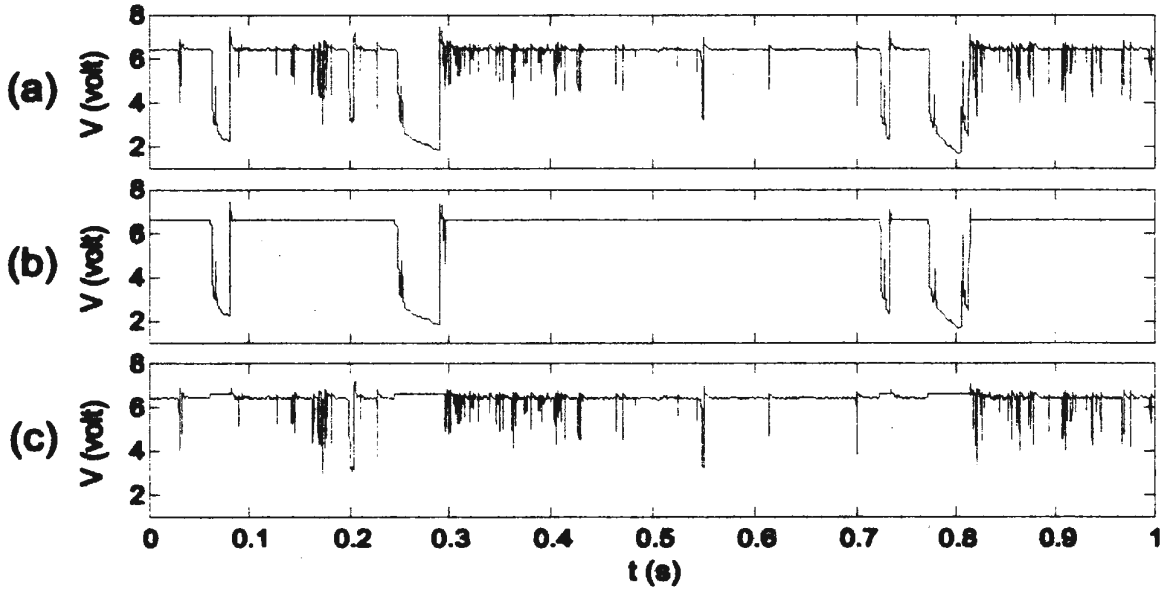

Figure 6.12 - Separated slug and bubble signals: (a) Original signal; (b) Slug signal; (c) Bubble signal

Figure 6.12 shows the decomposed signals, together with the original signal. Figure 6.12c is obtained by removing the slug signal from the original signal, therefore, the signal of the small bubbles is recovered completely. This process clearly shows that it is possible to extract the signal due to different bubble size groups using the method discussed above.

The time-difference-of-arrival of a particular bubble size group is estimated through a direct cross correlation of the discriminated signals from the two probes. The cross correlation function R_{xy} is calculated as:

$$R_{xy}(\tau) = \frac{1}{T}\int_0^T \frac{V_1(t)\cdot V_2(t-\tau)}{\sqrt{V_1(t)^2 \cdot V_2(t)^2}}\,dt \qquad (6\text{-}3)$$

where $V_1(t)$ and $V_2(t)$ are the discriminated signal outputs from the primary and secondary probes, respectively. There is a distinct peak in the cross-correlation function, which makes it easy to determine the time delay τ. Figure 6.13 shows the cross correlation functions for the entire bubble population (Figure 6.13a), slugs (Figure 6.13b) and small bubbles (Figure 6.13c) of the sample flow. The peak values of the three cross-correlation functions are about 0.87, 0.95 and 0.63, respectively.

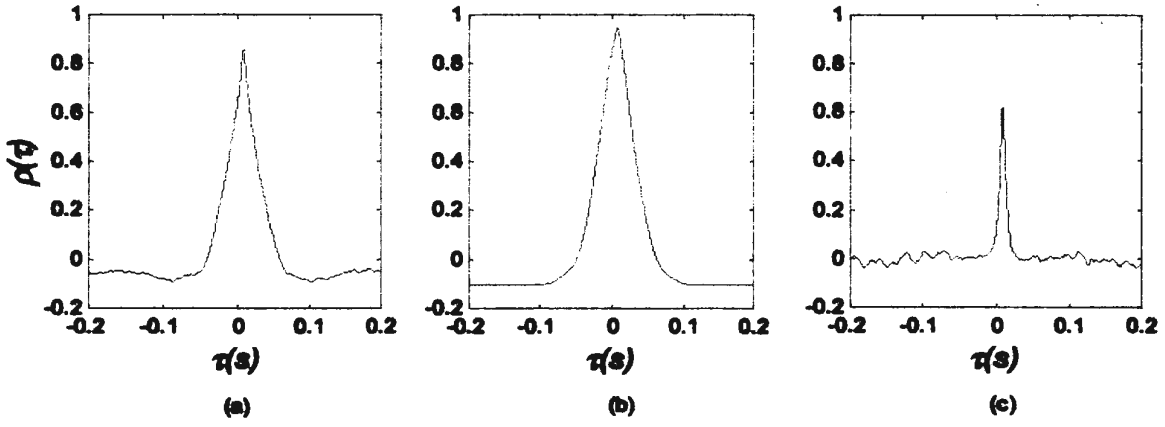

Figure 6.13 - Typical cross correlation function for:
(a) entire bubble population; (b) slugs; (c) small bubbles

The high peak value for the slug signal implies that the gas slugs change very little over the distance between the probes, while the relatively lower peak value for small bubbles implies that not all the bubbles striking the primary probe hit the secondary

probe. As expected, the peak cross-correlation value for the entire bubble population lies between those of the slugs and small bubbles.

The time delay from the cross-correlations can be interpreted as a mean time delay for the specific bubble group concerned. The velocity is estimated from the probe spacing, L_P, and the resultant time delay, τ_m, as:

$$u_G = \frac{L_P}{\tau_m} \tag{6-4}$$

Once the velocity for each bubble size group has been estimated, the bubble chord length for each bubble group is calculated as:

$$l = u_G \cdot \Delta t_{12} \tag{6-5}$$

where l is the bubble chord length and Δt_{12} is the time that the probe is within the gas bubble/slug.

Figure 6.14 shows the velocity profiles of the sample flow. The slug velocity is greater than the bubble velocity, while the average gas velocity lies between the slug and bubble velocities. This is consistent with the flow physics, since one would expect the slugs to have a higher velocity than the smaller bubbles due to the larger buoyancy force on the slugs. As expected, the slug velocity profile is constant across the cross section of the pipe. The bubble and average bubble velocity profiles are similar to that of the void fraction. The profiles are more or less uniform up to about $r/R = 0.4$, and then decrease as

the wall is approached. Along the centerline of the pipe (r/R=0), the slug velocity is greater than the bubble velocity by about 14.9%. The difference between the slug and bubble velocity increases as the wall is approached due to the increasing influence of the wall on the smaller gas bubbles. For example, at r/R=0.8, the difference between the slug, and bubble velocities increases to 41.5%. The average gas bubble velocity and the bubble velocity have similar profiles except that the average gas bubble velocity is slightly higher than the bubble velocity. On average, the average bubble velocity is greater than the bubble velocity by about 5% for this flow.

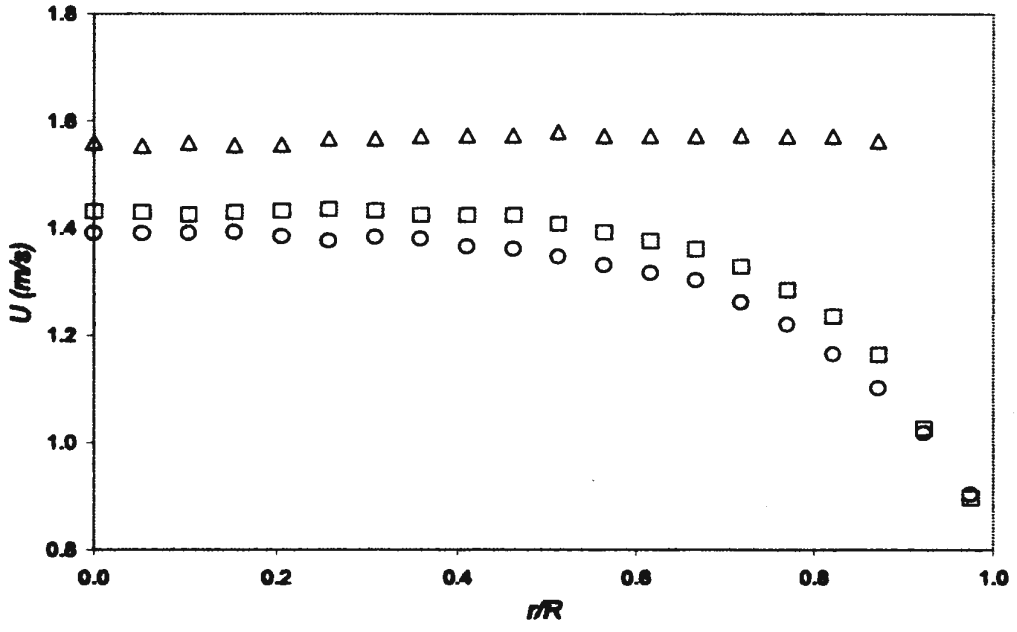

Figure 6.14 - Velocity distributions [Δ Slug; o Bubble; □ Average]

The sample flow (slug flow) is a liquid continuous flow, in which the gas bubbles are essentially carried by the liquid. The gas bubble velocity is primarily determined by the liquid velocity and the buoyancy force. To obtain some qualitative information on the

differences between the gas bubble velocity in two-phase flow and the velocity in single-phase flow, the bubble velocity profiles are compared with the power-law fully developed turbulent velocity profile (Figure 6.15). The Reynolds number is approximated from the total gas and liquid flow rates. The bubble velocity profile is flatter than the power-law distribution, and lies above the power-law distribution due to the buoyancy force experienced by the bubbles. Similar bubble velocity profiles were also reported by Cheng et al. (1998), and Liu and Bankoff (1993a, b).

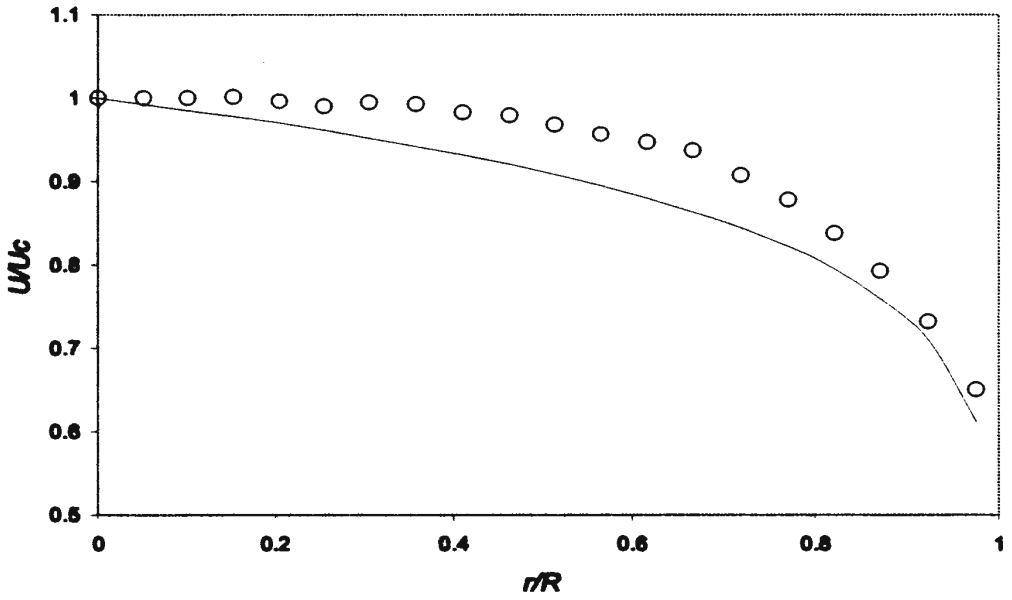

Figure 6.15 - Comparison of gas bubble velocity profiles with the power-law fully developed turbulent velocity profile

6.7 Slug and Bubble Lengths, Distributions and Frequencies

A better understanding of the flow can be achieved by relating velocities to different bubble size groups. The mean length of the slug can be interpreted directly as the slug length since the slug has a fairly uniform streamwise dimension. However, this is

not the case for a bubble, because the probe does not always penetrate the bubble along its diameter. A chord length varying from zero to the bubble diameter is typically measured, which results in a bubble chord length distribution. A typical bubble chord length histogram for the sample flow is provided in Figure 6.16.

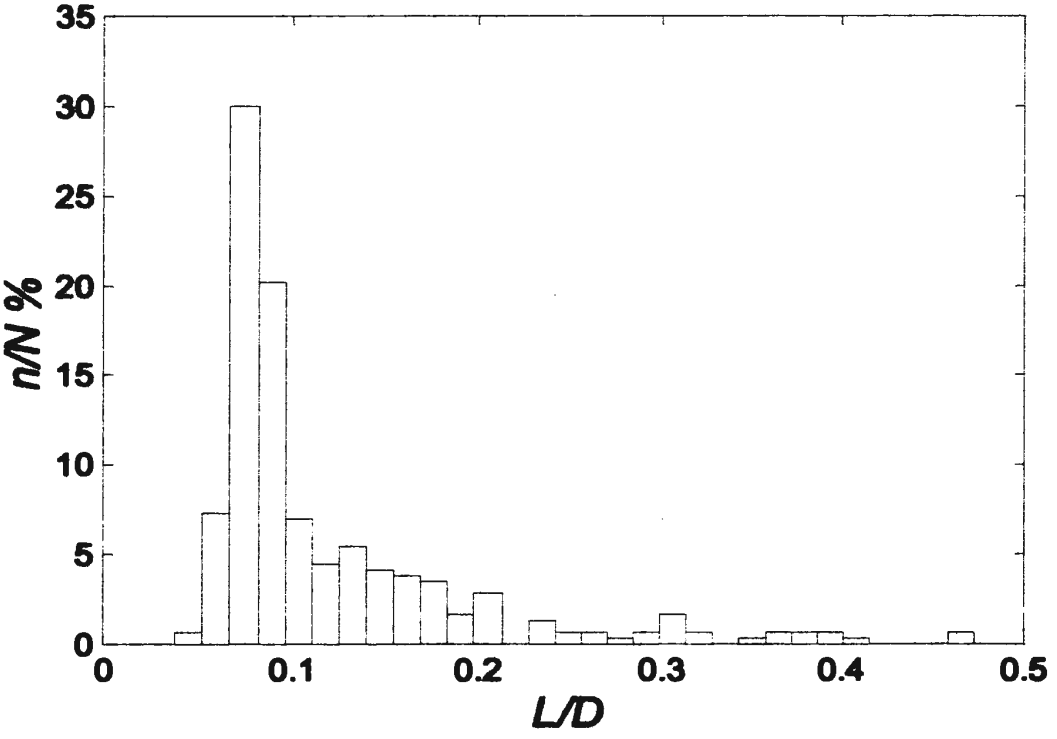

Figure 6.16 - Bubble chord length distributions

Statistical techniques have been developed to estimate the mean bubble diameter from the bubble chord length distribution (Uga 1972, Herringe and Davis 1976, Clark and Turton 1988). Thang and Davis (1979) developed a simple technique to estimate the mean bubble diameter from the bubble chord length distribution. They showed that the mean bubble diameter $\bar{d}$ can be approximated from the mean bubble chord length probability density function $g(x)$ as:

$$\bar{d} = 1.5\int_0^x x \cdot g(x)dx \qquad (6\text{-}6)$$

It should be noted that equation 6-6 is derived based on the following assumptions (Thang and Davis 1979):

1. All bubbles are spherical;
2. The probe has equal probability of piercing any point on the projected front area of bubbles; and
3. All bubbles travel in the same direction with the same average velocity.

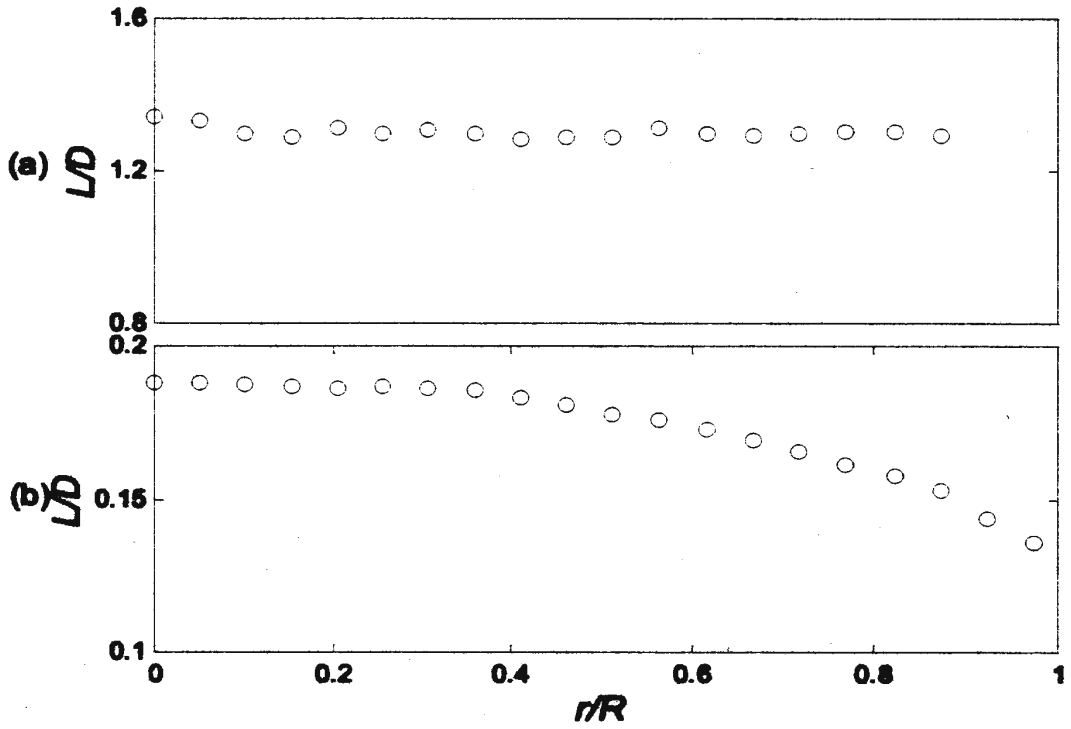

Figure 6.17 - Slug and bubble length distributions (a) Slug; (b) Bubble

The mean slug length and bubble diameter distributions corresponding to the velocities in Figure 6.14 are shown in Figure 6.17. As expected, the size of the gas slug is more or less uniform across the cross section of the pipe, having a variation within ±5% (Figure 6.17a). The mean bubble diameter is a maximum (0.18D) in the pipe center region and gradually decreases (0.14D) as the wall is approached (Figure 6.17b). This can be explained as follows:

1. The large bubbles tend to migrate to the central region of the pipe, because of the reduced drag in this region. Another reason for this central migration is the radial lift force generated due to the lower velocity on the side of the bubble near the wall. This lift force tends to induce the bubbles into the central region of the pipe.
2. Large bubbles are more prone to form in the pipe central region, because of the increased likelihood of bubble coalescence due to the higher gas and bubble concentration in this region (see Figure 6.6 for void fraction distribution, and Figure 6.19 for bubble frequency distribution discussed in the following paragraphs).

The average dimensions of slugs and bubbles can be calculated by weighting the length of the slugs/bubbles with the slug/bubble population. Also, a gas flow rate (or gas superficial velocity) can be estimated by integrating the resultant void fraction and gas velocity distributions as:

$$U_G^* = \frac{\int_A u_G(r) \cdot \varepsilon(r) dA}{A} \qquad (6\text{-}7)$$

where $u_G(r)$ is the average bubble velocity at location r. To check the accuracy of the hot-film measurement, the gas velocity estimated from equation 6-7 was compared with the

superficial gas velocity directly measured from the gas flow meters (Table 6.2). The discrepancy (below 8.7 %) is probably due to the uncertainty associated with the measurements of void fraction as well as slug/bubble velocities.

Table 6.2 Comparison of Superficial Velocities

U_G (m/s)	U_G^* (m/s)	$\lvert\frac{U_G - U_G^*}{U_G}\rvert \times 100\%$
0.23	0.25	8.7

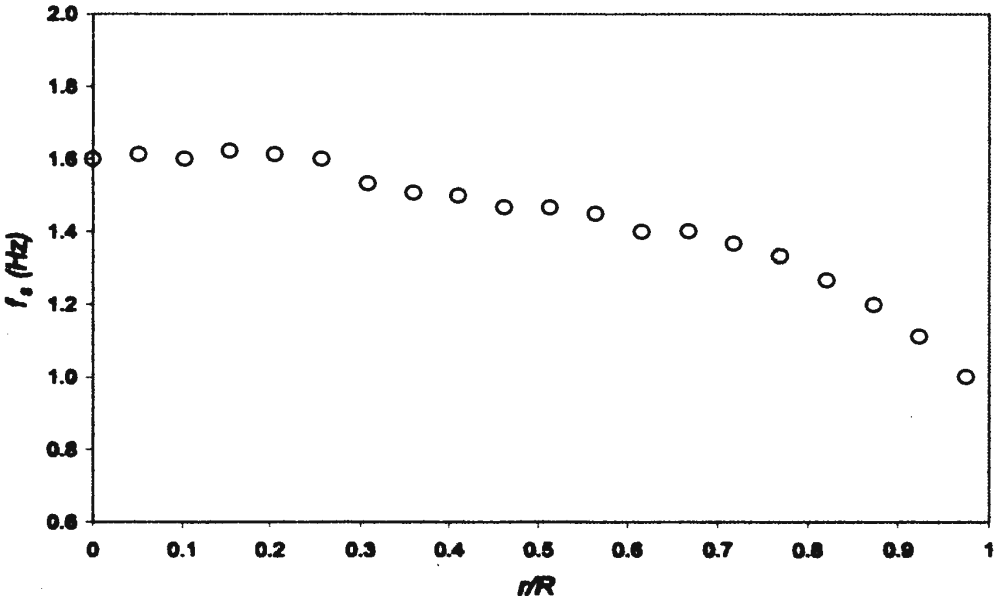

Figure 6.18 - Slug frequency distribution

A more complete description of the flow can be accomplished if the bubble/slug frequency is known. The local bubble/slug frequency is defined as the number of bubbles/slugs passing through a specific location in unit time. Figures 6.18 and 6.19 provide the local frequencies of the slugs and bubbles respectively for the sample flow.

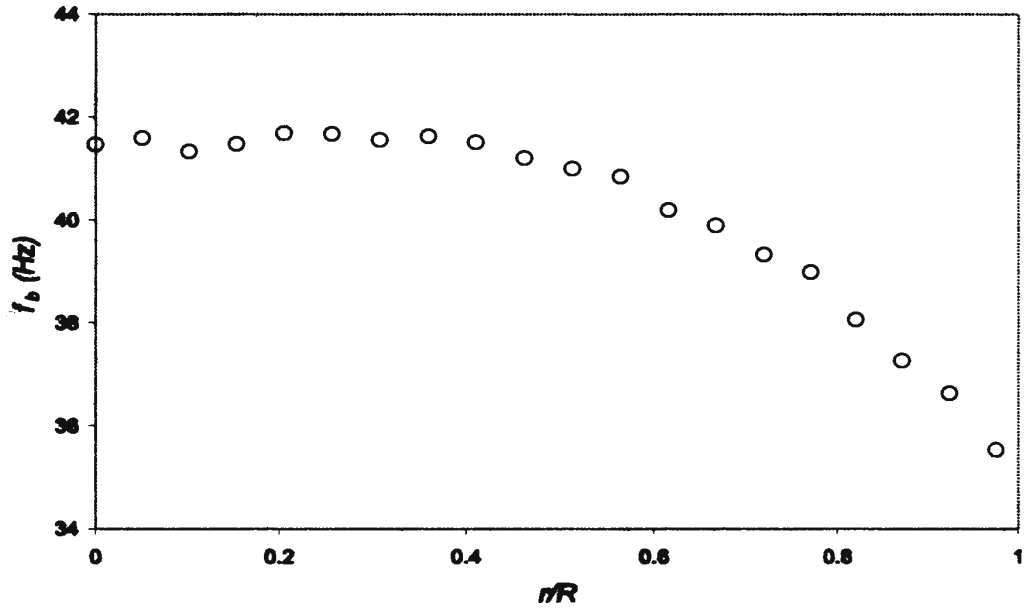

Figure 6.19 - Bubble frequency distribution

In general, the bubble has a much higher local frequency than the slug. On average, the local bubble to slug frequency ratio is about 30. However, globally, this ratio is expected to be much higher, because the detection of a slug is global while the detection of a bubble is relatively local. Both the slug and bubble frequencies achieve a maximum in the pipe central region. The frequencies decrease as the wall is approached. For this particular flow, the slug frequency varies from 0.85 Hz in the wall region to about 1.61 Hz in the central region, while the bubble frequency varies from 36.1 Hz to 41.5 Hz between these two regions. The higher bubble frequency at the pipe central region promotes bubble coalescence at this region. This coalescence is reflected by the higher slug frequency in the pipe central region. Similar trends for bubble frequency distribution were also reported by Cheng et al. (1998).

6.8 Phase Interfacial Area

Although a number of studies have been performed on two-phase flow, the interfacial area concentration has not been sufficiently investigated, either experimentally or analytically. There is still only limited information available on local values of interfacial area concentration. This information is, however, important for two- or three-dimensional flow analyses using two-fluid models. Most of the reported interfacial area concentration measurements were conducted on bubble flow. Kataoka et al. (1986) gave a comprehensive discussion on the formulations and measurements of local interfacial area concentration for bubble flow. The measurement often requires the knowledge of the direction of the normal vector of each interface (Kataoka et al. 1986). Accordingly, Hibiki et al. (1998) measured the interfacial area concentration using a double-sensor probe hot-film anemometry method for bubble flow. However, this information is not available from the single normal probe measurement used in the current study. A much simpler approach for predicting local interfacial area concentration for bubble flow was proposed by Akida and Yoshida (1974). This technique allows estimating the interfacial area concentration from a single normal probe measurement, without considering the normal vector of each interface. By assuming spherical bubbles, the local interfacial area concentration, $a_i(r)$, can be related to the local bubble void fraction, $\varepsilon(r)$, and bubble mean diameter, $\bar{d}(r)$ as (Akida and Yoshida 1974, Okawa et al. 1998):

$$a_i(r) = \frac{6 \cdot \varepsilon(r)}{\bar{d}(r)} \tag{6-8}$$

Equation 6-8 permits the estimation of the interfacial area concentration for bubble flow from the knowledge of void fraction and bubble diameter, which can readily be determined from a single normal probe measurement. Very little information is available on the interfacial area measurements and modeling for slug flow. In the current study, a classical model of the slug flow is used to estimate the interfacial area concentration. A slug flow can be approximated as a series of Taylor bubbles having a regular bullet-like shape separated by liquid slugs containing small spherical gas bubbles. The liquid slugs are assumed to have similar flow characteristics to bubble flow, and, therefore, are modeled as bubble flow. Under the above assumptions, a simple technique for estimating the interfacial area concentration can be derived. Mathematically, the phase interfacial area for slug flow can be considered as the sum of both the bubble surface area, A_b, and slug surface area, A_s, therefore, the phase interfacial area concentration for slug flow can be written as:

$$a_i = \frac{A_{ig}}{V_T} = \frac{A_b + A_s}{V_T} \tag{6-9}$$

where V_T is the total flow volume. Let the flow volume occupied by the Taylor bubbles be V_s and the remaining flow volume be V_b ($V_b = V_T - V_s$). Equation 6-9 can be expressed as:

$$a_i = \frac{V_s \frac{A_s}{V_s} + (V_T - V_s)\frac{A_b}{V_b}}{V_T} = \frac{V_s}{V_T} \cdot \frac{A_s}{V_s} + (1 - \frac{V_s}{V_T}) \cdot \frac{A_b}{V_b} \tag{6-10}$$

$\frac{V_s}{V_T}$ is equivalent to the void fraction of the Taylor bubbles, denoted by ε_s, and $\frac{A_b}{V_b}$ is the interfacial area concentration of the small bubbles in the liquid slugs. Accordingly, equation 6-10 can be simplified as:

$$a_i = \varepsilon_s \cdot \gamma_s + (1-\varepsilon_s) \cdot a_{ib} \tag{6-11}$$

where $\gamma_s = \frac{A_s}{V_s}$ is the surface/volume ratio of the Taylor bubbles, and $a_{ib} = \frac{A_b}{V_b}$ is the interfacial area concentration of the small bubbles in the liquid slugs.

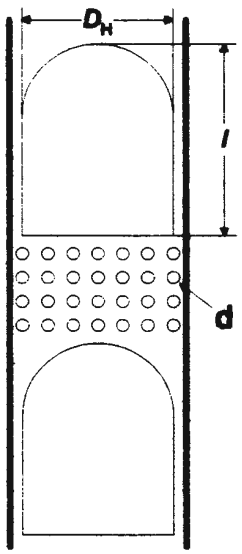

Figure 6.20 – Bullet-like shape Taylor bubble

The total interfacial area of the flow is made up of Taylor bubbles with an interface ratio of γ_s, and of small spherical bubbles with a diameter of $\bar{d}$ in the liquid

slugs. The diameter of a Taylor bubble can be approximated by the flow channel diameter, D_H, and its surface/volume ratio, γ_s, is often approximated as $4.5/D_H$ (Levy 1999). By taking into account the geometry of the Taylor bubble, which is assumed as a regular bullet-like shape (Figure 6-21), a more accurate surface/volume ratio for Taylor bubbles can be expressed as:

$$\gamma_s = \frac{A_s}{V_s} = \frac{24 \cdot l}{D_H(6 \cdot l - D_H)} \tag{6-12}$$

where l is the length of the Taylor bubble. Since the remaining flow (liquid slugs) is modeled as bubble flow, equation 6-8 is valid for this part of the flow provided the void fraction is taken as the void fraction of the remaining liquid slugs.

By substituting equation 6-8 into equation 6-11, the total interfacial area concentration can be expressed as:

$$a_i = \varepsilon_s \cdot \gamma_s + (1 - \varepsilon_s) \cdot \frac{6 \cdot \varepsilon_b}{\bar{d}} \tag{6-13}$$

where ε_b is the bubble void fraction in the liquid slugs. Accordingly, the local interfacial area concentration can be written as:

$$a_i(r) = \varepsilon_s(r) \cdot \gamma_s(r) + [1 - \varepsilon_s(r)] \cdot \frac{6 \cdot \varepsilon_b(r)}{\bar{d}(r)} \tag{6-14}$$

In addition to the bubble diameter and slug length, the local information of the slug void fraction and bubble void fraction in the liquid slugs must be determined in order to estimate the interfacial area concentration. Figures 6-21 and 6-22 show the void fraction distributions for the slugs and bubbles respectively. Note that the bubble void fraction shown in Figure 6-22 is the fraction of air in the liquid slugs. The void fractions are calculated from the discriminated slug and bubble signals (see Figure 6-12). The void fraction for slugs shows a maximum in the pipe central region and decreases toward the wall. It varies from 0.11 in the pipe central line to 0.081 at the wall and shows a trend similar to the slug frequency. This is expected because the slug void fraction is more or less proportional to the slug frequency. The void fraction distribution for bubbles is quite uniform (about 0.125) until r/R=0.7 and shows a steep decrease in the wall region. In spite of the fact that the slug has a much lower frequency than the bubble, it accounts for almost half of the total gas volume for this particular flow condition.

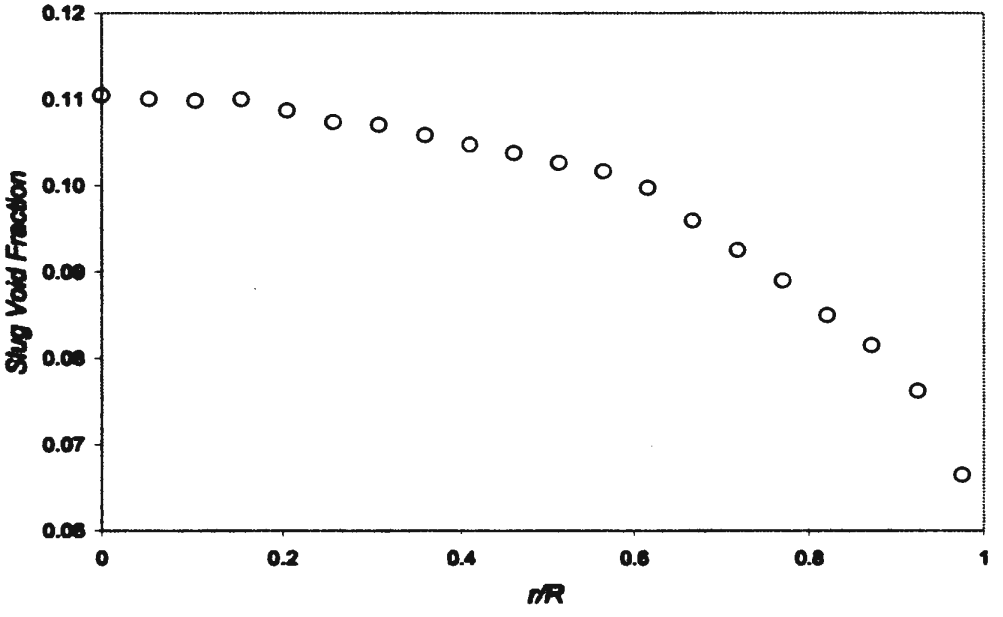

Figure 6.21 - Slug void fraction distribution

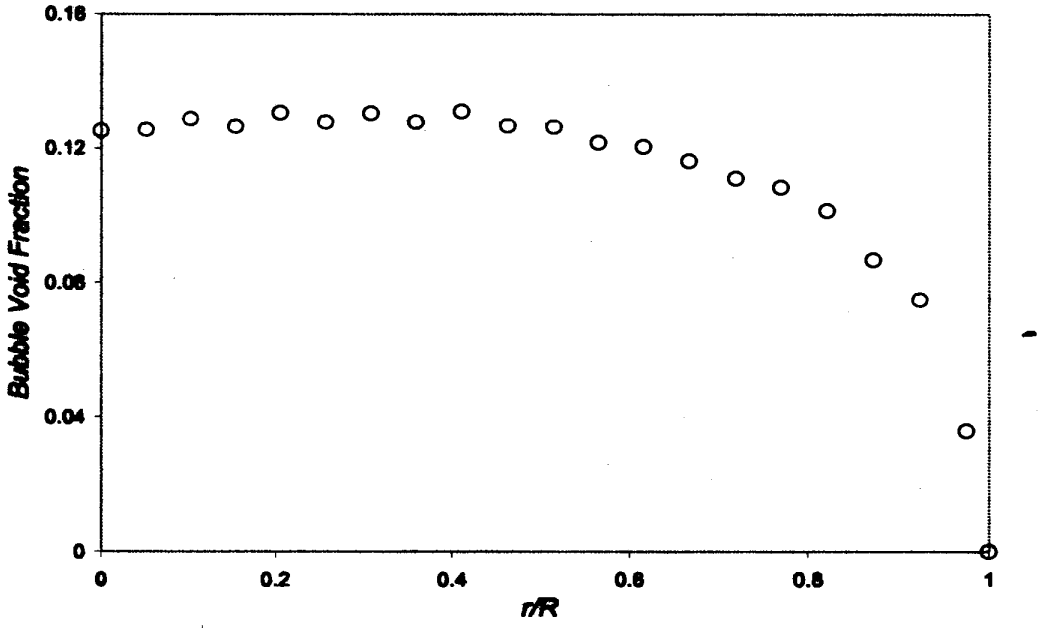

Figure 6.22 - Bubble void fraction distribution

Having determined the bubble diameter, slug length, local slug and bubble void fractions, it is possible to calculate the interfacial area concentration for this flow by using equation (6-14). Figure 6.23 shows the resultant distributions for interfacial area concentration. Both the simplified method ($\frac{4.5}{D_H}$) and geometry method (Equation 6-12) were attempted to estimate the interfacial area concentration for the Taylor bubbles using equation 6-14. The two schemes show remarkable agreement, with an average discrepancy below 4 %. The interfacial area concentration shows rather uniform values in the central region (r/R<0.7) and rapidly reduced values near the wall. A similar profile was also reported by Serizawa et al (1975a, b, c) for slug flow. However, the flow data were measured using double- and multiple-sensor probe techniques.

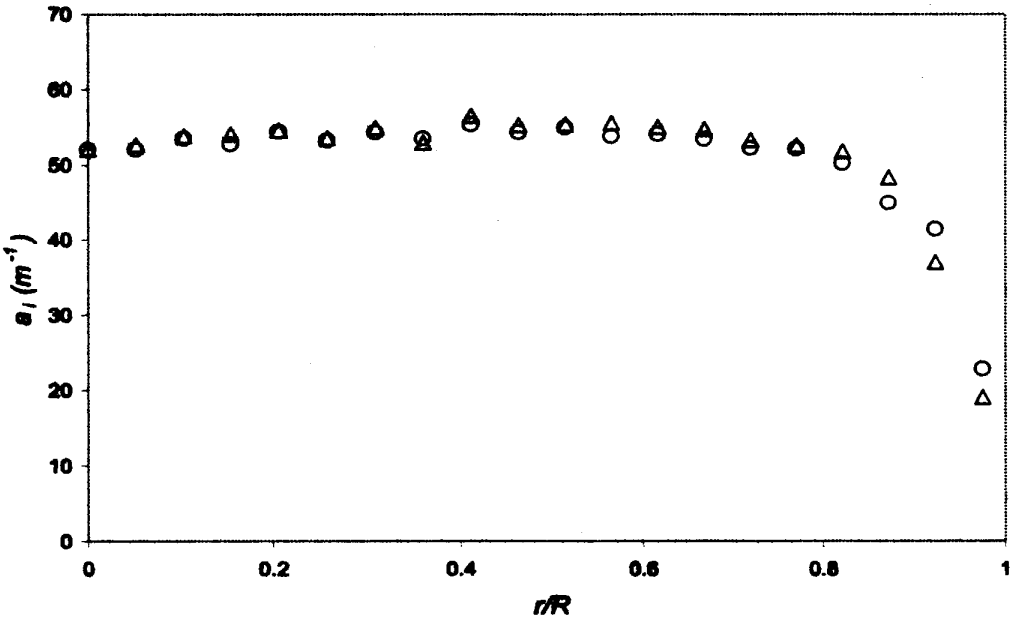

Figure 6.23 - Interfacial area concentration distribution [o $\frac{4.5}{D_H}$; Δ Geometry]

The area averaged interfacial area concentration can be calculated by integrating the interfacial area concentration distribution by assuming radial symmetry of the flow distribution.

$$a_i = \frac{\int_A a_i(r) \cdot dA}{A} \tag{6-15}$$

6.9 Verification with High Speed Flow Visualization

Simultaneous measurements of the gas slug/bubble velocities were obtained using the hot-film anemometry system and a quantitative flow visualization system to verify the hot-film data reduction techniques. Figure 6.24 shows a typical dual-probe hot-film signal response to the passage of a single gas slug, with the corresponding high-speed

flow images. The points of contact of the slug front and back with the probes (points A, B and C, D in the two traces) are clearly seen in the flow images, and occur at the same temporal locations as the hot-film traces.

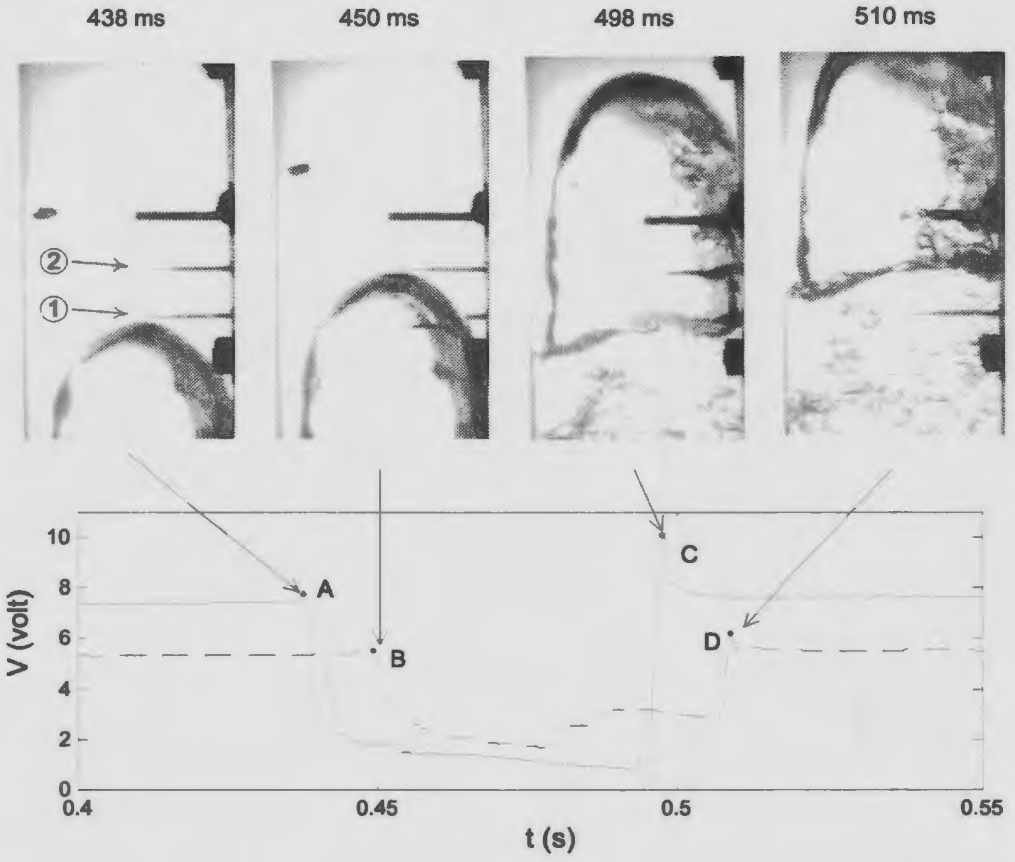

Figure 6.24 - Simultaneous flow visualization and hot-film signal

Digital image processing algorithms were used to obtain slug/bubble velocities from the high-speed flow images. The gas slug and bubble velocities were estimated using two separate image processing algorithms: a supervised motion tracking algorithm and an edge detection cross-correlation algorithm. The supervised motion tracking algorithm allows the user to identify and track the movement of distinguishable flow entities (bubbles and slugs) by manually selecting corresponding entity coordinates on

consecutive frames of the flow. The algorithm segments the identified fluid entities using a triangular mesh and tracks displacement and shape deformation over multiple frames. The gas bubble/slug velocities are estimated from the displacement and known time step between the frames (Ching et al. 1999a).

Figure 6.25 provides a sample image showing the selected gas bubbles. The calibration scale is also displayed in this figure. The accuracy of the velocity estimation can be improved by placing more landmarks around the perimeter of the bubbles and slugs. Although this algorithm provides an effective method for capturing the details of the motion, it is difficult and laborious to accurately determine the corresponding entity coordinates on consecutive frames of the flow (Ching et al. 1999a).

Figure 6.25 - Bubble selection for supervised motion tracking

The edge detection cross-correlation algorithm developed by Hiscock (2000) was used to remove the subjectivity associated with the supervised motion tracking algorithms. It provides detailed bubble velocity information for the entire image. The principle of this algorithm is illustrated in Figure 6.26.

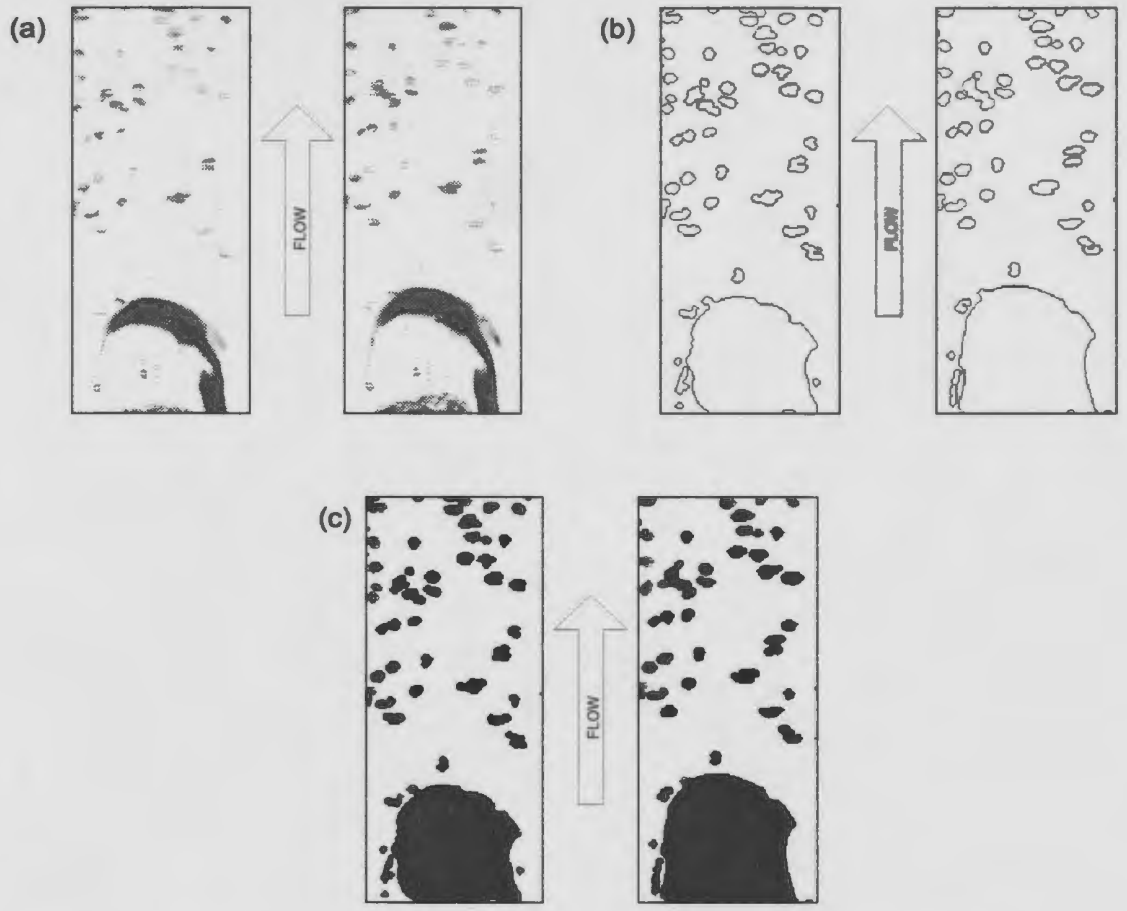

Figure 6.26 - Edge detection cross-correlation algorithm: (a) Consecutive frames; (b) Application of edge detection; and (c) Application of morphological operations

Two consecutive frames of a flow sequence are shown in Figure 6.26a. The clusters of bubbles and one air slug are clearly distinguishable in the images. The vertical lines of the image border represent the pipe walls of the test section while the horizontal lines are the limits of the field of view of the camera. The quality of the acquired image determines the level of image enhancement required, and may include a combination of histogram equalization, adaptive noise removal and linear filtering. The image filtering helps to make the bubbles sharper and easier to detect by highlighting points, lines and edges and suppressing uniform and smoothly varying regions. Edge detection routines are applied on the enhanced images to demarcate bubble and slug boundaries (Figure 6.26b).

Image enhancement and edge detection routines rarely produce images that can be successfully used for cross-correlation analysis. In order to match pixel patterns by a correlation method, images with distinct and consistent surfaces are required. Morphological operations are applied to the edge detected images to obtain such images. Morphological operations are methods for processing binary images based on shapes and are fundamentally neighbor operations that involve adding (dilation) or removing (erosion) pixels from a binary image according to certain patterns or rules. A combination of a dilation operation followed by an erosion operation using the same structuring element is used to close the bubble edges (Figure 6.26c) (Hiscock et al. 2000).

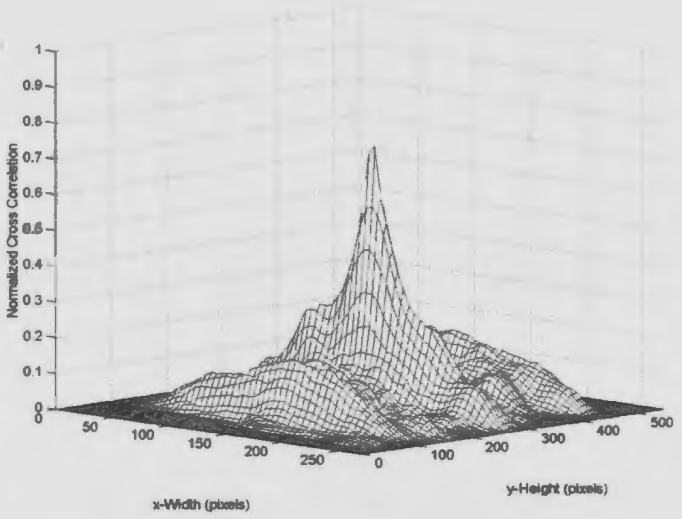

Figure 6.27 - Cross-correlation function between two consecutive flow images

The average displacement of the gas bubbles is determined through a cross correlation between the two processed images (Figure 6.27). The signal peak is clearly distinguishable from the noise peaks, allowing an accurate estimation of the gas bubble displacement. The location of the peak in the cross-correlation function corresponds to

the displacement of the gas bubbles between the two images. The velocity is calculated from the resultant displacement and the time interval between the two consecutive frames.

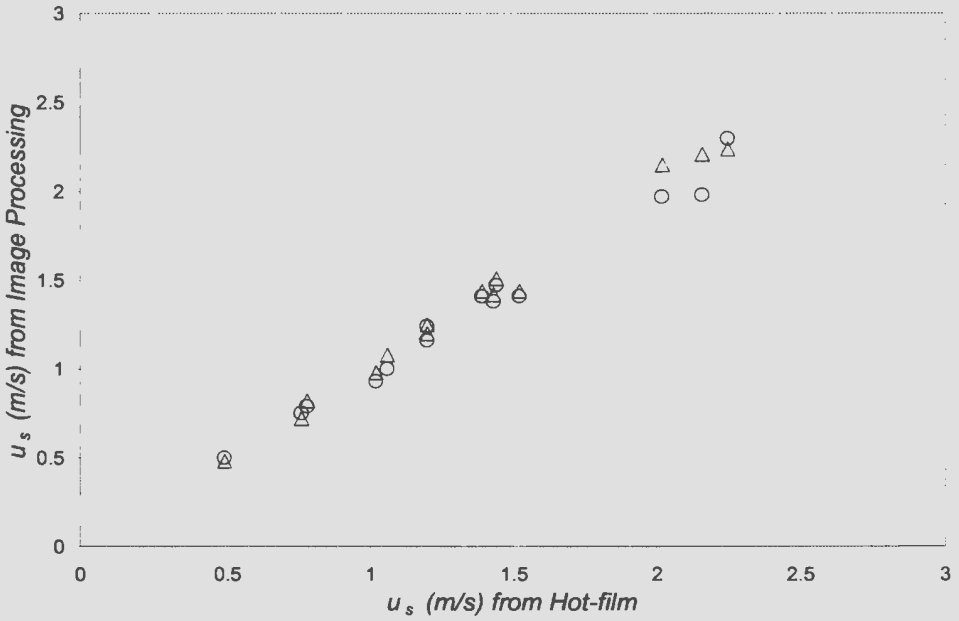

Figure 6.28 - Comparison of slug velocity between hot-film and image processing algorithms [Δ Supervised motion tracking; o Edge detection cross correlation]

A number of comparisons, covering a significant flow range, were conducted to verify the measurements from hot-film anemometry with those from the two image processing algorithms. The results of these comparisons are provided in Figures 6.28 and 6.29 for slugs and bubbles respectively. For the supervised motion tracking system, the bubble velocities are calculated as the mean of several tracked bubbles. On average, the discrepancy for slug velocity is below 4% and the discrepancy for bubble velocity is 9.5% between the two systems. However, the agreement is expected to improve by increasing the number of tracked bubbles and slugs. The discrepancies between the two

image processing algorithms are 3% for slugs and 6% for bubbles. The good agreement between the two measurement systems indicates that the dual-probe hot-film anemometry system is a viable technique for obtaining a significant amount of information of the gas flow in gas-liquid flows.

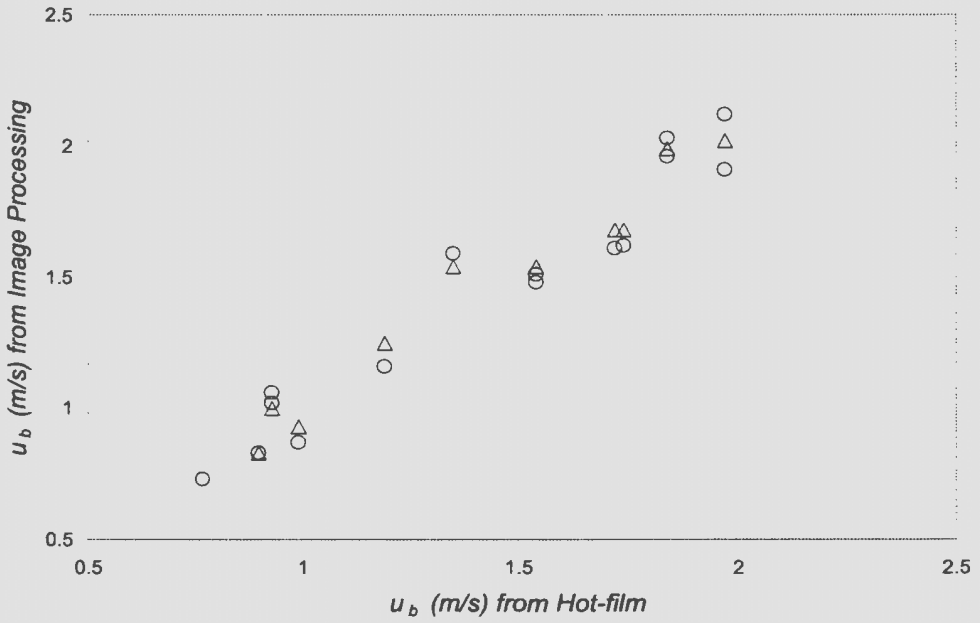

Figure 6.29 - Comparison of bubble velocity between hot-film and image processing algorithms [Δ Supervised motion tracking; o Edge detection cross correlation]

6.10 Experimental Uncertainty Analysis

A complete uncertainty analysis was performed based on the method of Moffat (1988). The uncertainty attributed to a measurement is an estimate of the possible residual error in that measurement after all proposed corrections have been made. An error source is usually categorized as fixed or random depending on whether the error it introduces is steady or changes during the time of one complete experiment (Moffat 1988).

The fixed error is reproducible and usually due to incorrect calibration of the measurement instruments, hence it is often called calibration (or bias) error. Normally, the fixed error can be eliminated by re-calibration. On the other hand, the random error (precision error) is due to the limited precision of the measurement instruments as well as the scatter in the repeated measurements.

The uncertainties of the measurements discussed in this thesis are associated with the phase flow rates, phase velocities, bubble lengths, bubble frequencies and interfacial area concentration. In this study, each measurement instrument is carefully calibrated for each series of flow measurements. In this manner, the calibration errors can mostly be eliminated, therefore, the uncertainty analysis in this thesis is focused on the precision errors.

If the result R of an experiment is calculated from a set of independent measurements X_i, the precision index of the result S_R is affected by the precision index of each measurement S_i as (Moffat 1988):

$$S_R = \left\{ \sum_{i=1}^{N} \left(\frac{\partial R}{\partial X_i} S_i \right)^2 \right\}^{1/2} \tag{6-15}$$

In the current study, the uncertainty is calculated using the multiple-sample analysis methodology, since each measurement is a multiple sample of the quasi-steady state flow. Additionally, the results are calculated from the mean of several measurements. The precision index of the mean is, therefore, what is needed in the uncertainty analysis. It can be calculated as (Moffat 1988):

$$S_{\bar{x}_i} = \frac{S_{x_i}}{\sqrt{N}} \tag{6-16}$$

From the uncertainty of each flow measurement series, the overall uncertainty for a single measurement can be calculated as:

$$(U_R)_{95} = (tS_R) \tag{6-17}$$

where t is the student's multiplier for 95% confidence.

Table 6.3 Experimental Uncertainy

Parameter	Uncertainty	
	Max. %	Min. %
Q_L	1.08	1.08
Q_G	1.72	1.72
$\frac{q_G}{q_L}$	2.03	2.03
$\frac{q_L}{D^{5/2} g^{1/2}}$	1.08	1.08
Void Fraction	5.9	3.2
u_G	3.2	1.7
f_s	8.1	4.3
f_b	6.4	3.4
l/D	7.7	4.2
d/D	4.0	2.1
a_i	8.5	4.5

The void fraction, phase velocities, bubble frequencies, bubble lengths and interfacial area concentration presented in this study are calculated as the averages of 20 data series. The mean liquid and gas flow rates are the averages of over 1000 sample points. The uncertainties of these measurements can be calculated using the methodology

described above. For example, the accuracy of the 3-inch flow meter is 1%, which can be interpreted as an uncertainty of 0.5% for 95% confidence (Moffat 1988). The typical precision index of the mean liquid volume flow rate is 0.2% (equation 6-16). Therefore, the precision index of the measured liquid volume flow rate can be estimated from equation 6-15 as 0.54%. The Max./Min. student multipliers for 95% confidence are 2 for large number of sampling points, and therefore, the Max./Min. overall uncertainties are 1.08% (equation 6-17). Table 6.3 provides the experiment uncertainty of all the measured flow parameters.

6.11 Summarizing Remarks

A relatively simple dual-probe hot-film anemometry technique has been developed to measure void fraction, gas bubble velocities, bubble size and bubble frequency. An innovative data reduction technique using wavelet analysis combined with a phase detection scheme was developed to discriminate the hot-film output into signals corresponding to different bubble size groups. The desired flow information corresponding to each bubble group can be obtained by cross correlation analysis of the discriminated signals. The bubble diameter is estimated from the bubble chord length information. By modeling the slug flow as discrete Taylor bubbles separated by liquid slugs, which are modeled as bubble flows, a technique for estimating the interfacial area concentration for slug flow from a single normal probe measurement has been proposed. The measurements from the hot-film anemometry were corroborated using a quantitative flow visualization system.

Chapter 7

Results and Discussion of the Flow Pattern Model

New flow pattern mapping parameters for vertically upward gas-liquid flows have been formulated from dimensional arguments of the flow pattern functional equations in section 5.2. This chapter presents the development of a new dimensionless flow pattern map using the data from the MUN flow loop, as well as six additional sets of data from the literature. Once the flow pattern map is generated, pattern recognition techniques are used to systematically determine the transition boundaries between the neighboring flow patterns. Finally, the new flow pattern map is validated using oil-water-gas multiphase flow data from the National Engineering Laboratory (NEL) in Glasgow, U.K.

7.1 Dimensionless Flow Pattern Map

Experiments were performed using air-water two-phase flow in the MUN 3-inch flow loop to generate different flow patterns for superficial liquid and gas velocities in the range of 0.15-3.5 m/s and 0.05-10.5 m/s, respectively. The flow pattern identification was done at a distance of 50 pipe-diameters $(\frac{L}{D} = 50)$ downstream from the nearest elbow with the assistance of the high-speed flow visualization system. This allows the

flow pattern to be identified in slow motion at a later stage, and minimizes the uncertainty due to direct visual observation of the flow pattern.

The flow pattern observations from the MUN flow loop are in good agreement with Hewitt and Hall-Taylor's classification of the two-phase flow patterns (Hewitt and Hall-Taylor 1970). Four distinct flow patterns, bubble, slug, churn and annular, were observed with transition bands between slug/churn, churn/annular and bubble/annular. In order to develop a more accurate flow pattern map, six additional sets of flow pattern data over a range of flow dimensions and fluid properties were used from the literature.

Table 7.1 lists the data sources, the fluids and respective densities and pipe diameters of the data set. The pipe diameters vary in the range from 10-mm to 92-mm. The two flow phases include air-water, steam-water and R113 vapor-liquid. The density for the gas phase varies in the range of 1 - 36.5 kg/m^3 while the density for the liquid phase is in the range of 740 - 1386 kg/m^3. All the four major flow patterns were observed in each data series. The seven sets of data spread over a significant range of flow conditions and therefore should give a broad representation of the flow patterns. Note that the different data sources are distinguished by different colors in Figures 7.1, 7.2 and 7.3 as described in Table 7.1.

Table 7.1 Flow pattern data sources

Data Source	Fluid	D_{Pipe} (m)	ρ_G (kg/m^3)	ρ_L (kg/m^3)	Fig. 7.1, 7.2 and 7.3
MUN 3-inch Flow Loop	Air-Water	0.078	1	1000	Red
Taitel et. al (1980)	Air-Water	0.025	1.29	1000	Pink
Annurgiates and Giradi (1983)	Air-Water	0.092	1.29	1000	Green
Baker (1965)	Steam-Water	0.01	32.2	1307	Black
Bergles and Suo (1966)	Steam-Water	0.01	17.5	816	Blue
Bergles and Suo (1966)	Steam-Water	0.01	36.5	740	Yellow
Weisman and Kang (1981)	R113 vapor/liquid	0.025	27.2	1386	Turquoise

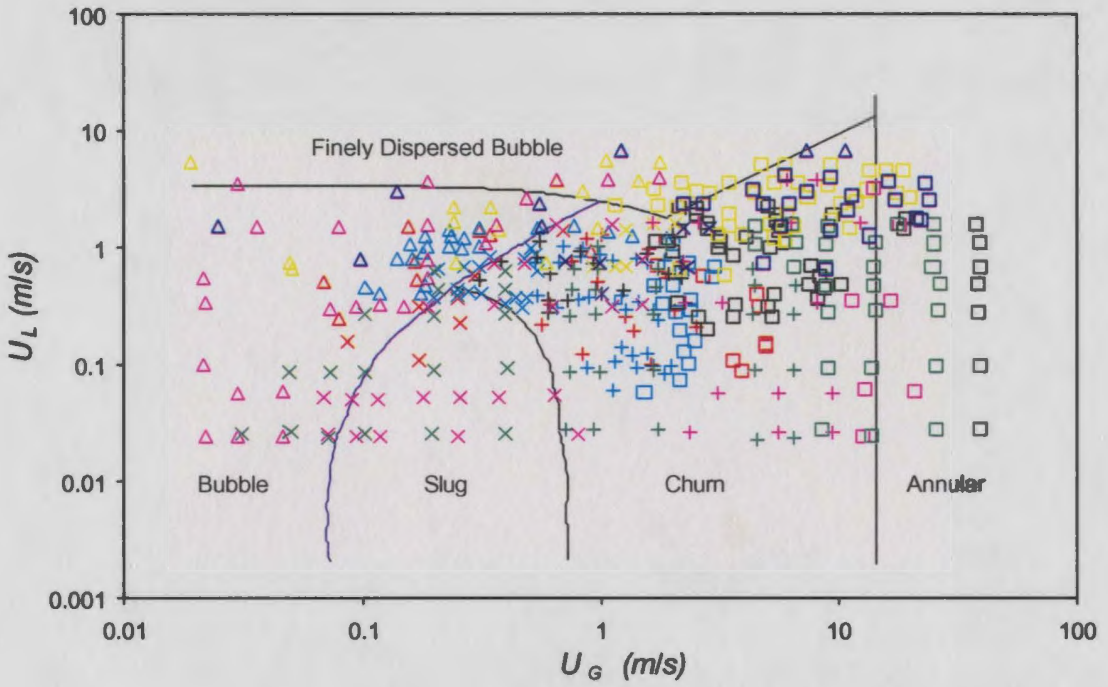

Figure 7.1 - Data comparison with flow pattern map of Taitel et al. (1980)
[Δ Bubble; × Slug; + Churn; □ Annular]

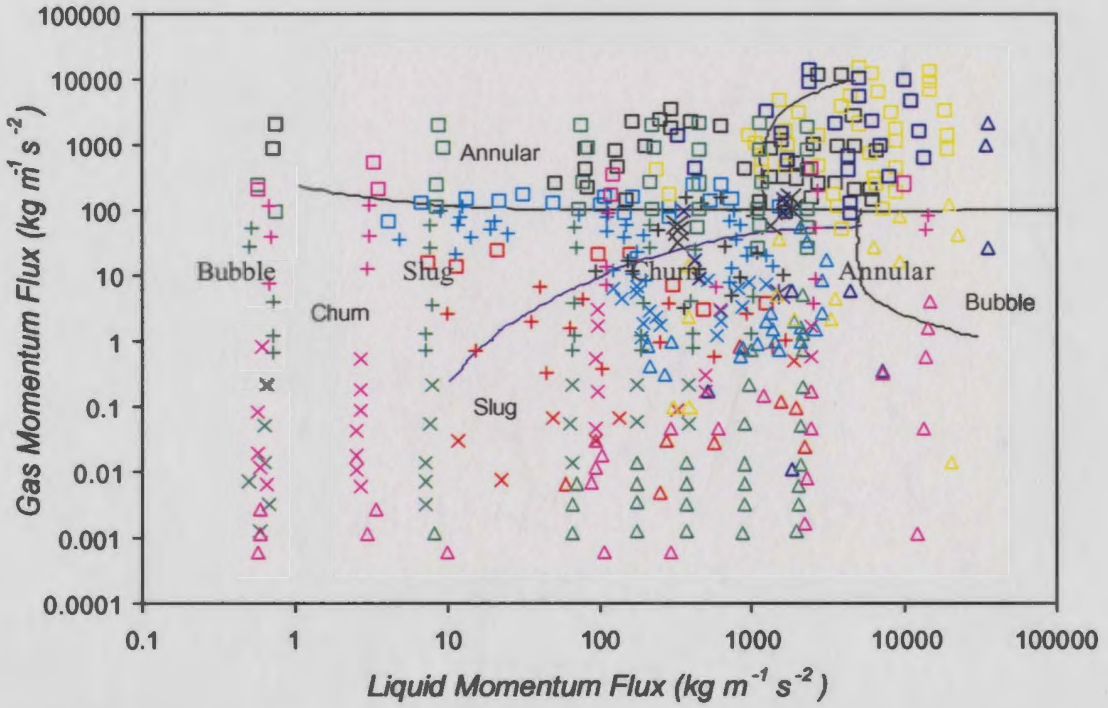

Figure 7.2 - Data comparison with flow pattern map of Hewitt and Roberts (1969)
[Δ Bubble; × Slug; + Churn; □ Annular]

The data are firstly presented using the two traditional mapping techniques: superficial velocities (Figure 7.1) and momentum fluxes (Figure 7.2). The two flow pattern maps used for comparsion are those proposed by Taitel et al. (1980) for l_E/D=50 and Hewitt and Robert (1969), which are the two most commonly used flow pattern maps. In both cases, there is significant overlap between different flow patterns from the different facilities. The regions associated with each flow pattern are not readily distinguishable. In addition, the data show poor agreement with the two flow pattern maps, especially in the annular flow regime for the map of Taitel et al. (1980), and in the bubble flow regime for the map of Hewitt and Roberts (1969).

A review of the flow pattern maps in section 2.2 has indicated that most of them show little convergence for different flow facilities and fluid properties. This is evident in the above comparisons. Tests with data from different diameter pipes indicate that none of the discussed flow pattern maps can successfully accommodate changes in flow geometry and fluid properties. The primary reason is the inappropriate use of flow pattern mapping parameters. Other possible reasons may include:

1. The subjective nature of flow pattern identification. Although the flow patterns are well defined, there is some inconsistency in interpretation of the visual observations by different authors.
2. The flow pattern not being fully developed at the observation location. A flow pattern observed at one location could eventually evolve into another pattern at some downstream location.
3. The difficulty in the identification of transition flow patterns.

4 The dependency of the flow pattern on the upstream phase mixing method (McQuillan and Whalley 1984).

The proper standardization of the flow pattern mapping parameters is an initial step to approaching a universal flow pattern map. Such a flow pattern map can significantly simplify the flow pattern identification method.

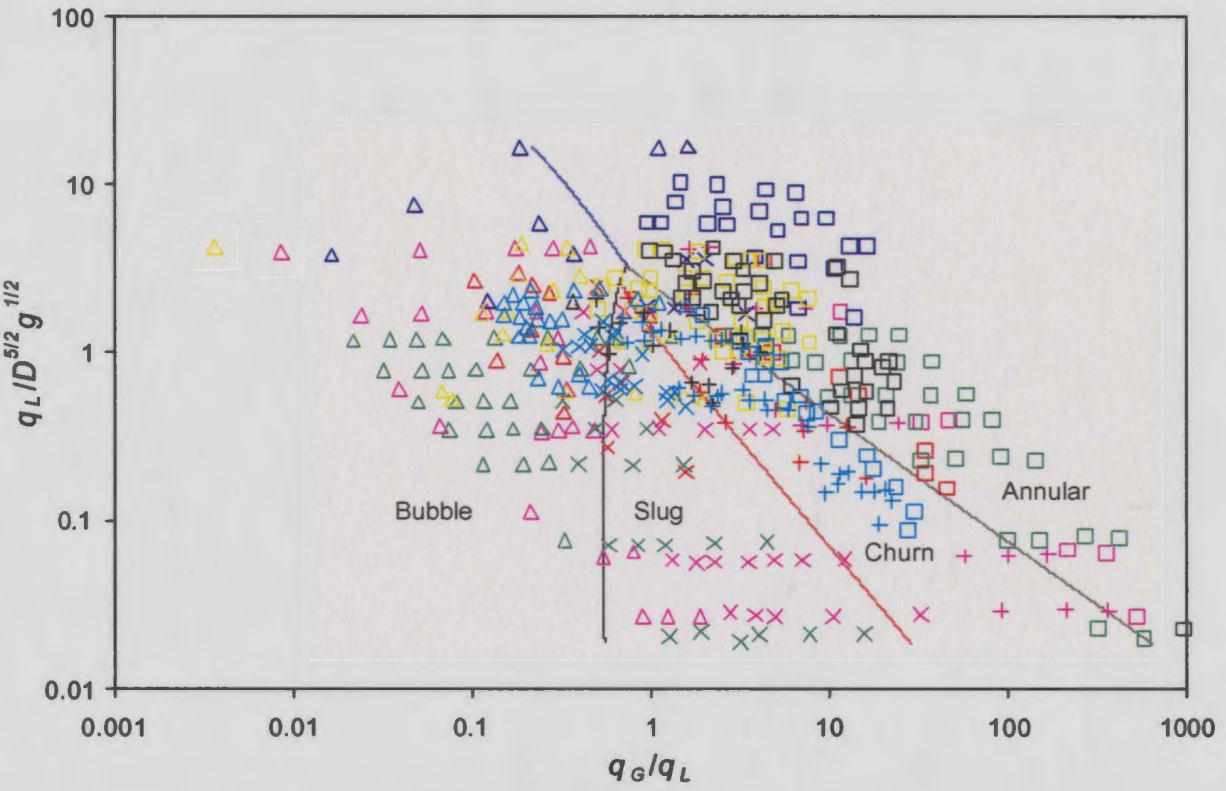

Figure 7.3 – Proposed flow pattern map with $\frac{q_G}{q_L}$ and $\frac{q_L}{D^{5/2}g^{1/2}}$ as mapping parameters [Δ Bubble; × Slug; + Churn; □ Annular]

The flow pattern data when plotted using the dimensionless parameters, $\frac{q_G}{q_L}$ and $\frac{q_L}{D^{5/2}g^{1/2}}$, display fairly distinct regions for each flow pattern (Figure 7.3). There is less

overlap between the different flow patterns. This is accomplished with the use of dimensionless mapping parameters, where the effect of pipe diameter and fluid properties has been incorporated into the mapping parameters, making the data less dependent on them. The use of dimensionless mapping parameters for the presentation of flow patterns is an important step towards a universal flow pattern map, as it allows comparison of flow pattern maps from different flow facilities and fluids.

7.2 Flow Pattern Transition Boundaries

A complete flow pattern map also requires a systematic method to define the transition boundaries between the different flow patterns. The dimensionless flow pattern data (Figure 7.3) fall into several regimes that correspond to an ensemble of closely linked data points. The separation between the neighboring regimes is not readily observable and thus pattern recognition techniques can be used to effectively classify the flow patterns. The classification process highlights the defining attributes of each regime, which is then used to determine the pattern boundaries. The Minimum Intra-Class Distance Classifier (MICD) method (Tou and Gonzales 1974), based on Bayesian decision theory, is used to extract the pattern boundaries. For the case of flow pattern classification, where w_i represents the occurrence of flow pattern I, and x are the flow pattern map data set ($\frac{q_G}{q_L}$, $\frac{q_L}{D^{5/2}g^{1/2}}$), the a priori probability, $P(w_i)$, and the conditional probability, $P(x|w_i)$, are readily available. The posteriori probability can be estimated using Bayesian theory as:

$$P(w_i \mid x) = \frac{P(x \mid w_i)P(w_i)}{P(x)} \tag{7-1}$$

where $P(x) = \sum_{i=1}^{n} P(x \mid w_i)P(w_i)$. It is necessary to classify a new observation, x, using a methodology that attempts to minimize the classification error. The following Bayesian decision rule minimizes the probability of error:

$$\textit{Decide } w_1 \textit{ if } P(w_1 \mid x) > P(w_2 \mid x), \quad \textit{otherwise decide } w_2 \tag{7-2}$$

The flow pattern classification is determined primarily by the conditional probability densities $P(x \mid w_i)$ and in general is derived for the case of the multivariate normal density function:

$$P(x) = \frac{1}{(2\pi)^{\frac{n}{2}} |\Sigma|^{\frac{1}{2}}} \exp[-\frac{1}{2}(x-\mu)' \Sigma^{-1}(x-\mu)] \tag{7-3}$$

where μ is the mean vector of the flow pattern data, Σ is the 2×2 covariance matrix of the flow pattern data, and $|\Sigma|$ is the determinant of Σ. In the MICD distance based classification method, a new observation is classed within the class to which it bears closest proximity. The MICD classifier measures an Euclidean distance, d, of the new observation to two neighboring flow patterns using standard deviation based on the following decision rule (Tou and Gonzales 1974):

$$x \in w_i \textit{ if } d_m^2(x, w_i) < d_m^2(x, w_j) \tag{7-4}$$

Hence, for two adjacent flow patterns denoted by 1 and 2, the flow pattern decision is determined from:

$$(x-\mu_1)^t \Sigma_1^{-1}(x-\mu_1) \underset{>}{\overset{<}{}}_2 (x-\mu_2)^t \Sigma_2^{-1}(x-\mu_2) \tag{7-5}$$

The boundaries are formed by the locus of intersections of equidistant contours. This distance-based classifier characterizes the flow patterns solely based on the mean of the flow patterns and covariance matrices. Therefore, the flow pattern boundary using the MICD classifier can be expressed as:

$$x^t(\Sigma_1^{-1}-\Sigma_2^{-1})x + 2(\mu_2^t\Sigma_2^{-1}-\mu_1^t\Sigma_1^{-1})x + \mu_1^t\Sigma_1^{-1}\mu_1 - \mu_2^t\Sigma_2^{-1}\mu_2 = 0 \tag{7-6}$$

By applying equation 7-6 on each neighboring flow pattern pair, the resultant flow pattern boundaries are determined and presented in Figure 7.3. Figure 7.4 is the final dimensionless flow pattern map showing only the transition boundaries in Figure 7.3.

It is useful to have mathematical expressions for the flow pattern transition boundaries in order to be able to incorporate them into the MPFM flow pattern identification algorithm. With $\Phi = \log_{10}(\frac{q_G}{q_L})$ and $\Psi = \log_{10}(\frac{q_L}{D^{5/2}g^{1/2}})$, the mathematical expressions for the boundaries from equation 7-6 are as follows:

Boundary between bubble and slug flow:

$$4.47\Phi^2 + 5.91\Phi\Psi + 0.24\Psi^2 - 4.99\Phi + 2.03\Psi - 1.45 = 0 \quad (7\text{-}7)$$

where $0.55 < \frac{q_G}{q_L} < 0.67$.

Boundary between slug and churn flows:

$$0.45\Phi^2 + 12.07\Phi\Psi + 9.33\Psi^2 - 6.64\Phi - 6.04\Psi + 0.62 = 0 \quad (7\text{-}8)$$

where $0.66 < \frac{q_G}{q_L} < 28.25$.

Boundary between churn and annular flows:

$$2.62\Phi^2 + 6.42\Phi\Psi + 3.79\Psi^2 + 6.93\Phi + 9.15\Psi - 4.32 = 0 \quad (7\text{-}9)$$

where $0.67 < \frac{q_G}{q_L} < 570.27$.

Boundary between bubble and annular flows:

$$2.30\Phi^2 + 11.56\Phi\Psi + 5.78\Psi^2 - 18.56\Phi - 13.17\Psi + 3.50 = 0 \quad (7\text{-}10)$$

where $0.19 < \frac{q_G}{q_L} < 0.67$.

The resultant flow pattern map (Figure 7.4) can be considered as a preliminary universal flow pattern map, though more flow pattern data are required to improve its accuracy. Developing a universal flow pattern map is important, as this should lead to a simpler and more robust method of flow pattern identification. The dimensionless flow

pattern map was further verified and validated with two sets of data from NEL (Hall 1997). This comparison is important to determine the validity of the flow pattern map for oil-water-gas three-phase flow.

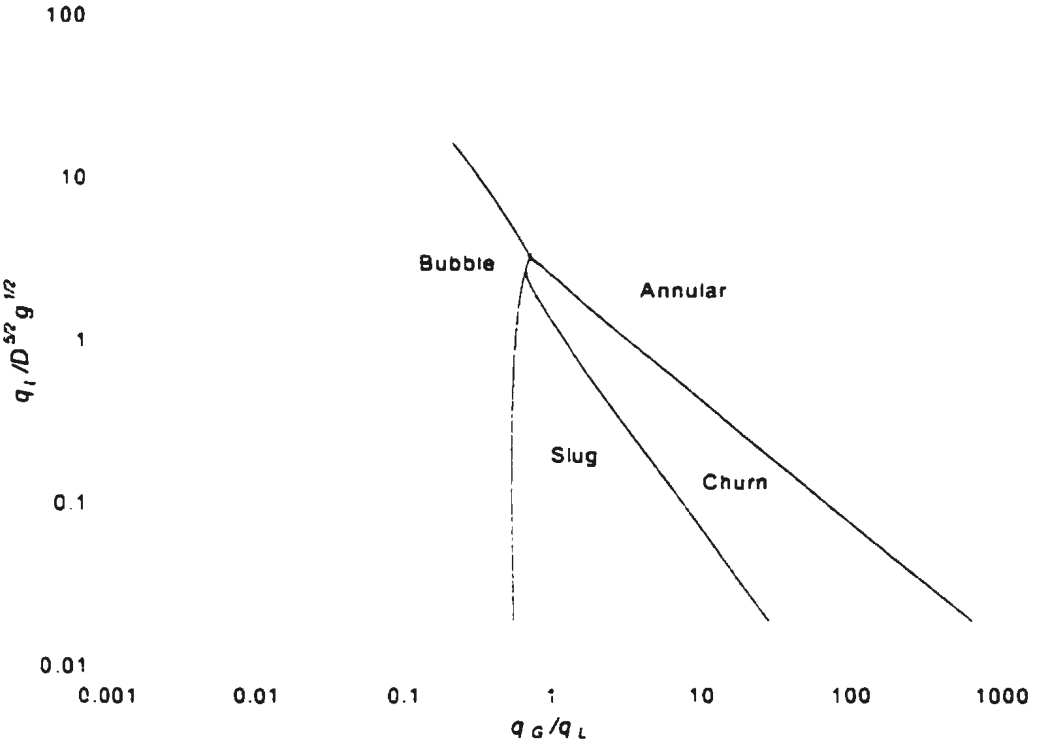

Figure 7.4 – Proposed dimensionless flow pattern map for vertical-up gas liquid flows

The NEL data is for oil-water-gas three-phase flow in 4-inch and 6-inch ID pipes. Nitrogen is used for the gas phase, and is supplied by the evaporation of liquid nitrogen on demand. The gas phase is metered upstream of the phase mixing section through a choice of three turbine meters according to the flow rate. The oil and water are supplied from a large gravity separator and pumped through the oil and water metering circuit respectively. Both metering circuits have a choice of two turbine meters according to the

flow rate required. This allows accurate flow metering in the concerned flow range with desired resolution. After metering, the three phases are passed into the multiphase mixing and measurement section. Different inlet devices are used according to whether the flow to be tested is horizontal or vertical. In the vertical configuration, two of the fluids are introduced through arrangements of injector tubes, with the gas phase flowing around the outside of the tubes. This configuration allows a stable flow pattern to be generated within a relatively short vertical length. Several pressure transducers and thermocouples are installed along the loops to monitor the in line flow condition. Operational control and data acquisition is implemented through a fully automated computer control system.

A mixture of topped Forties crude and kerosene is used for the oil phase and a solution of magnesium sulphate for the water phase. Experiments covering water cut from 3% to 100% were conducted for gas superficial velocity ranging between 0.5 to 24 m/s, and liquid superficial velocity between 0.03 to 2 m/s. The observation location for the 4-inch and 6-inch flow loops were $\frac{L}{D}$=50 and 33, respectively. Flow patterns were recorded by still photography, video, and by visual observation. Table 7.2 lists detailed flow dimensions and physical properties of the NEL data.

Table 7.2 NEL flow data

Fluid	D_{Pipe}(m)	ρ_G (kg/m^3)	ρ_L (kg/m^3)
Air-Water-Kerosene	0.102	1.17-5.05	854-1008
Air-Water-Kerosene	0.152	1.33-4.29	850-1029

The liquid density shown in Table 7.2 is the density of water and oil homogenous mixture. Geometry similarity ($\frac{L}{D}$) between the two cases is not satisfied since $\frac{L}{D}$ is 33

and 50 for the smaller and larger loops, respectively. However, if the flow patterns in the larger flow loop are assumed to be essentially unchanged from $\frac{L}{D}$=33 to 50, which is true in general, the geometry similarity restriction can be relaxed.

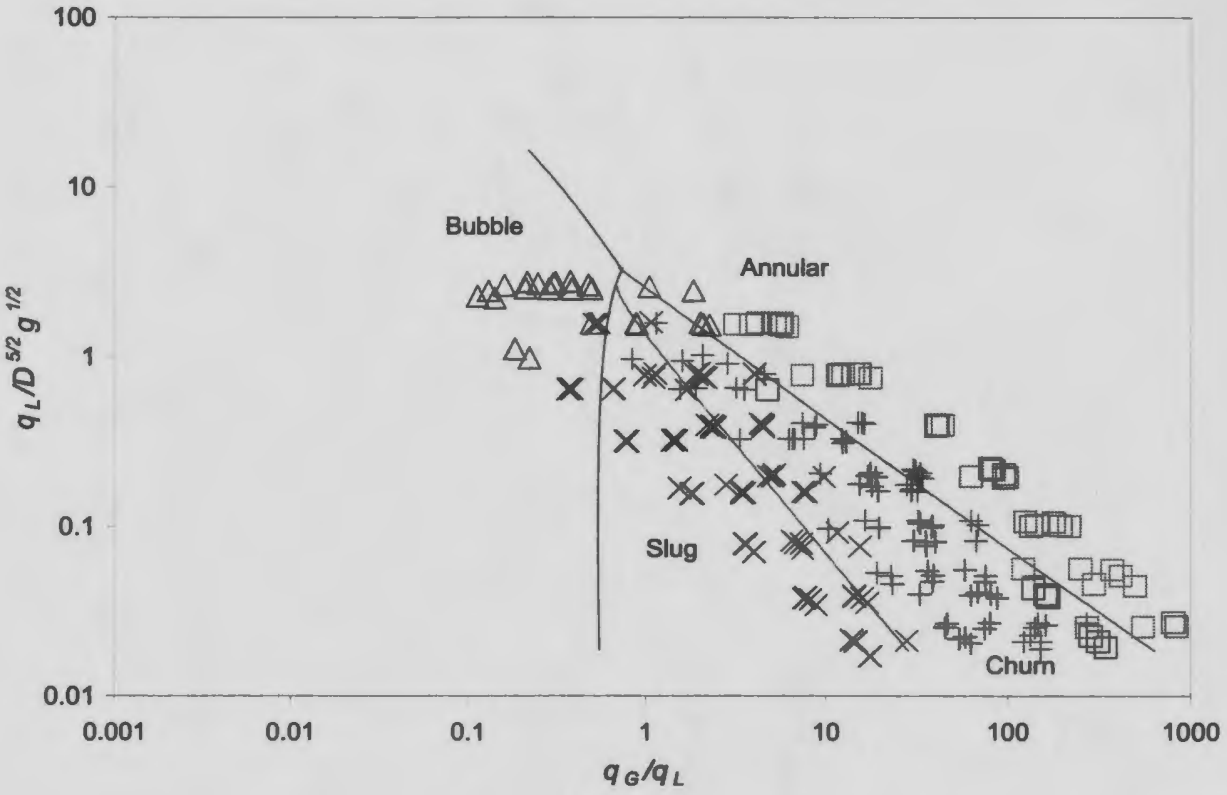

Figure 7.5 - Verification of the proposed dimensionless flow pattern map with NEL flow data [Δ Bubble; × Slug; + Churn; □ Annular]

The NEL data are plotted on the new dimensionless flow pattern map in Figure 7.5. The agreement of the two sets of data and the new flow pattern map is good. The good collapse of the two data sets can be attributed to both the use of dimensionless mapping parameters and the relative consistency of the flow pattern identification by a single flow observer. It also implies that the assumption of ingoring the surface tension

proposed in section 5.1 is reasonable. In addition, the good agreement between the new flow pattern map and the NEL flow data indicates that the new flow pattern map can be used to predict the flow patterns for vertically upward concurrent oil-water-gas multiphase flow.

7.3 Concluding Remarks

A new flow pattern mapping technique for vertical-up concurrent two-phase flows has been developed based on dimensional analysis. Dimensional analysis has yielded partial solutions and has provided the proper plotting parameters for the generalized two-phase flow pattern map. Great care must be taken in selecting the dominant variables for the flow functional equation. Oversimplification will limit the scope of application of the equation, but the unnecessary introduction of trivial variables will complicate the problem, and make the analysis difficult. The appropriate plotting parameters for vertically upward two-phase gas-liquid flow patterns are $\frac{q_G}{q_L}$ and $\frac{q_L}{D^{5/2} g^{1/2}}$. The two parameters suggest that the flow patterns are primarily dependent on the ratio of the gas-to-liquid flow rates and the Froude number of the liquid phase. By including the pipe diameter, fluid density and viscosity into the final dimensionless two-phase flow functional equation, the flow map is independent of these parameters, and hence should lead to a universal flow pattern map.

A pattern recognition technique was used to define the transition boundaries between the flow patterns. Although the flow pattern map was developed based on data for two-phase flows, it is equally valid for oil-water-gas multiphase flow. This is indicated by the good agreement between the new flow pattern map and oil-water-gas

multiphase flow data. From the MPFM project point of view, the development of the new flow pattern map will simplify its flow pattern identification algorithm, and, therefore, lead to a more robust MPFM.

Chapter 8

Results and Discussion on Slug Flow

The investigation of slug flow, and development of an interfacial area concentration correlation are the other major contributions of this study. A systematic analysis of the distributions of void fraction, slug void fraction, slug/bubble velocities, slug/bubble sizes, slug/bubble frequencies and interfacial area concentration are presented for several different flow conditions. Based on the results, correlations for predicting these flow parameters have been developed. Comparisons of the new correlations with those reported in the literature were also discussed.

8.1 Variation of Slug Flow Characteristics

A series of flow measurements was carried out on vertically upward slug flow under different flow conditions at the MUN 3-inch flow loop. The flow conditions cover a superficial liquid velocity range of 0.97–2.63 m/s, and a superficial gas velocity range of 0.18–0.46 m/s. Flow rates, temperature and pressure readings of the flow were continuously recorded during each measurement. Viscosity and density of the two phases were determined from the temperature and pressure measurements. For each flow case, hot-film measurements were performed at 20 radial locations along the pipe cross

section. The flow conditions are listed in Table 8.1 and are hereafter referred to by their case numbers. The data presented in the table are average values for the entire measurement period. The Froude number is defined as $Fr = V_m / \sqrt{gD}$, where V_m is the superficial mixture velocity, which is the sum of superficial gas and liquid velocities. Results were calculated using the data reduction techniques presented in chapter 6.

Table 8.1 Flow Conditions

Case	U_L (m/s)	U_G (m/s)	$\frac{v_G}{v_L}$	$\frac{v_L}{D^{\frac{3}{2}} g^{\frac{1}{2}}} \times 10^{-5}$	$\frac{q_L}{v_L D} \times 10^5$	$\frac{q_G}{q_L}$	$\frac{\Delta\rho}{\rho_G}$	Fr	$\frac{\sigma_L}{g\Delta\rho D^2}$
1	0.97	0.23	14.5	1.3383	0.7025	0.62	708.66	1.4	0.0012
2	1.07	0.21	16.3	1.3648	0.7011	0.82	727.87	1.5	0.0012
3	1.14	0.43	15.3	1.3801	0.7411	1.72	665.68	1.8	0.0012
4	1.48	0.20	17.8	1.3293	1.0017	0.69	750.92	1.9	0.0012
5	1.47	0.34	16.4	1.5118	0.8744	1.41	688.04	2.1	0.0012
6	1.50	0.46	17.1	1.3527	0.9967	1.83	712.35	2.2	0.0012
7	1.68	0.20	17.4	1.3392	1.1253	0.68	849.13	2.2	0.0012
8	1.64	0.37	17.8	1.3090	1.1286	1.48	664.96	2.3	0.0012
9	1.62	0.45	16.3	1.2848	1.1312	1.77	615.44	2.4	0.0012
10	2.07	0.18	16.8	1.2871	1.4484	0.70	653.24	2.6	0.0012
11	2.04	0.28	16.2	1.3810	1.3291	1.12	719.77	2.7	0.0012
12	2.04	0.38	16.5	1.3684	1.3392	1.61	620.19	2.8	0.0012
13	2.06	0.45	16.9	1.3254	1.3976	1.81	580.38	2.9	0.0012
14	2.30	0.22	16.7	1.3768	1.5037	0.81	591.89	2.9	0.0012
15	2.40	0.29	16.6	1.3555	1.5884	1.17	716.06	3.1	0.0012
16	2.35	0.45	16.3	1.4477	1.4557	1.75	529.98	3.2	0.0012
17	2.63	0.23	16.9	1.3482	1.7503	0.90	576.26	3.4	0.0012
18	2.60	0.38	16.2	1.3816	1.6940	1.64	412.02	3.4	0.0012

8.1.1 Effect of Superficial Gas Velocity on Slug Flow

Flow data for four test series: cases 4, 5, 6, cases 7, 8, 9, cases 10, 11, 12, 13 and cases 14, 15, 16, were collected at different superficial gas velocities for a constant liquid flow rate. The discrepancy in superficial liquid velocity among the cases for each flow

series is within ±3% of the desired value. The gas superficial velocity ranges from 0.18 m/s to 0.46 m/s.

Figures 8.1 and 8.2 show the slug velocity and length distributions for the four test series. Similar to the results presented in Figures 6.14 and 6.17 of chapter 6, the slug velocity and length profiles are fairly uniform across the pipe cross section for all the flow cases. The increase in gas flow under a constant liquid flow increases the slug velocity and slug length.

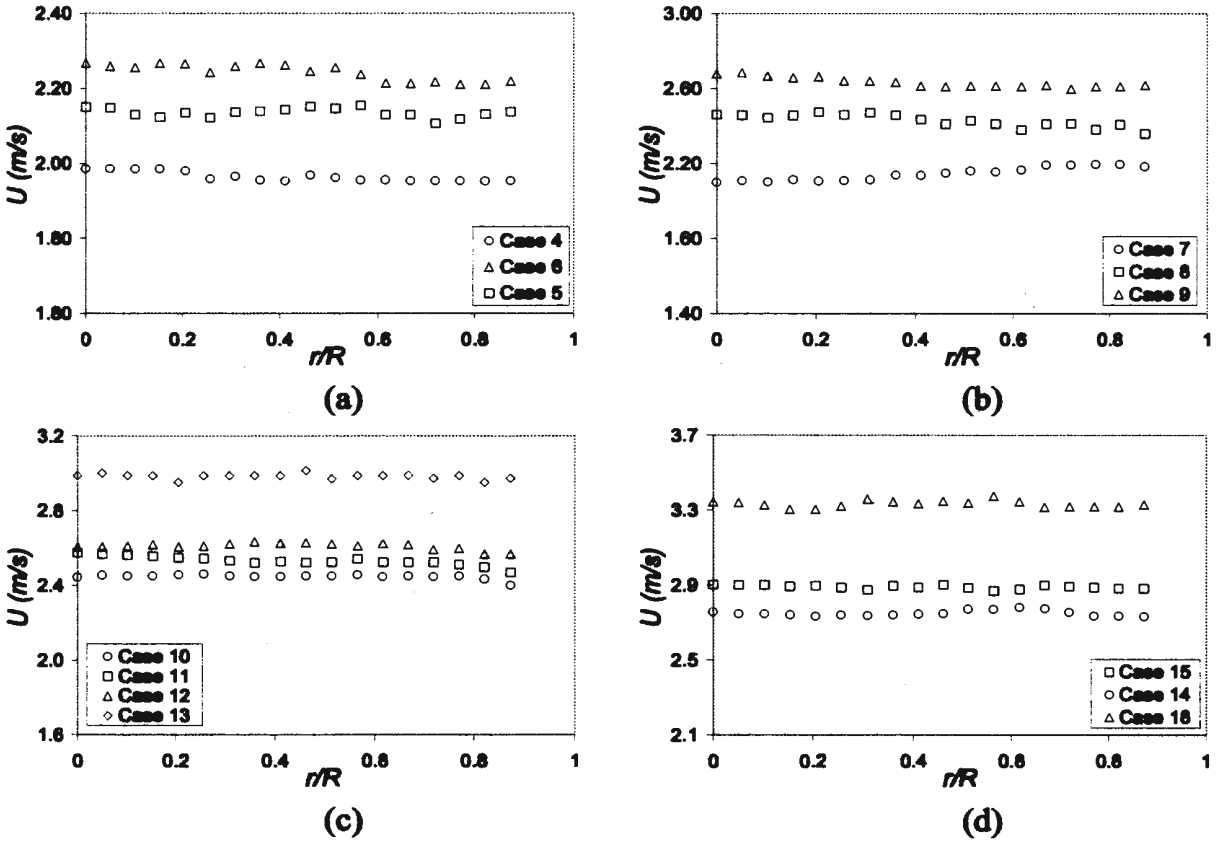

Figure 8.1 - Slug velocity distribution for different U_G
(a) U_L=1.5 m/s: U_G= O 0.2 m/s, □ 0.34 m/s, Δ 0.46 m/s
(b) U_L= 1.65 m/s: U_G= O 0.2 m/s, □ 0.37 m/s, Δ 0.45 m/s
(c) U_L=2.05 m/s: U_G= O 0.18 m/s, □ 0.28 m/s, Δ 0.38 m/s, ◊ 0.45 m/s
(d) U_L=2.35 m/s: U_G= O 0.22 m/s, □ 0.29 m/s, Δ 0.45 m/s

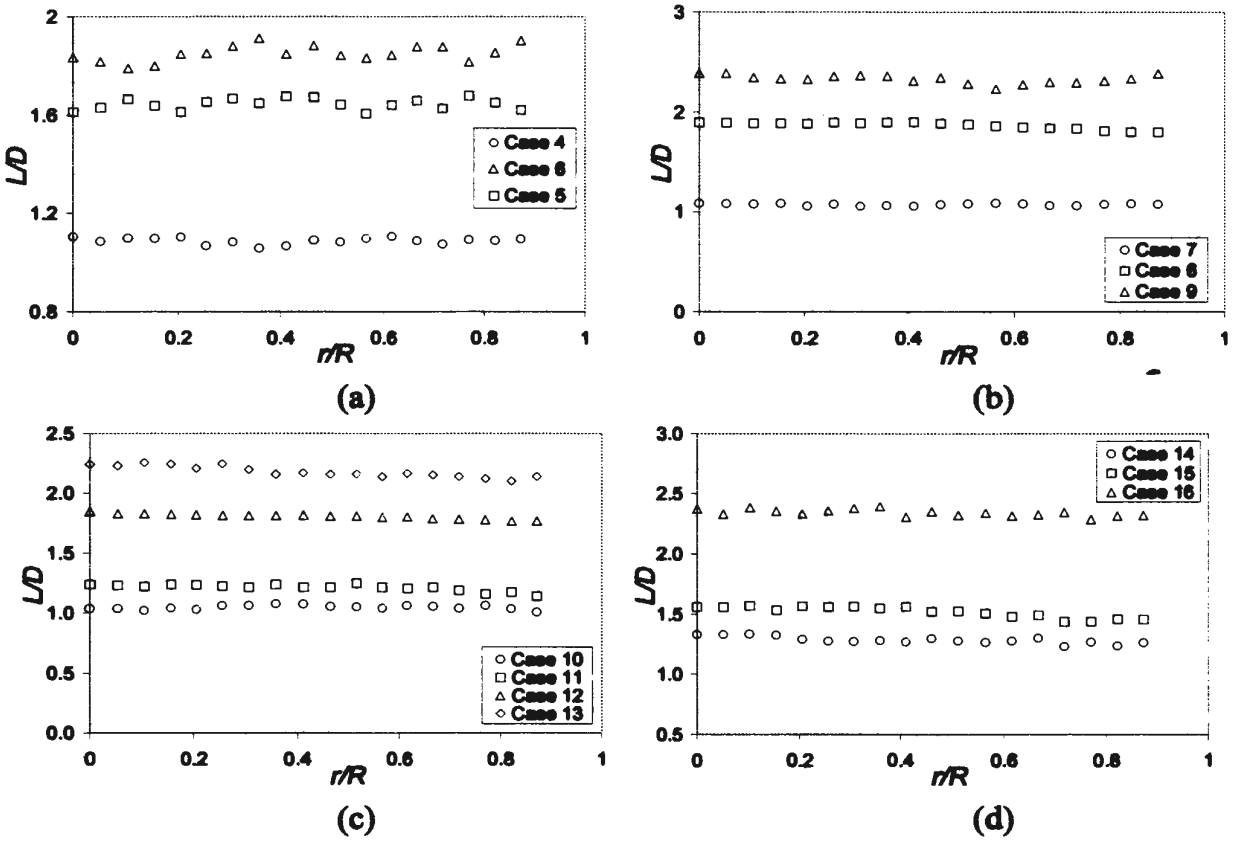

Figure 8.2 - Slug length distribution for different U_G

(a) U_L=1.5 m/s: U_G= O 0.2 m/s, □ 0.34 m/s, Δ 0.46 m/s

(b) U_L= 1.65 m/s: U_G= O 0.2 m/s, □ 0.37 m/s, Δ 0.45 m/s

(c) U_L=2.05 m/s: U_G= O 0.18 m/s, □ 0.28 m/s, Δ 0.38 m/s, ◊ 0.45 m/s

(d) U_L=2.35 m/s: U_G= O 0.22 m/s, □ 0.29 m/s, Δ 0.45 m/s

Figures 8.3 and 8.4 show the bubble and average slug/bubble velocity distributions for the four flow series. For each flow series, the two velocities show a similar trend, with the average slug/bubble velocity slightly higher than the bubble velocity. The bubble and average slug/bubble velocity distributions are fairly constant in the central region of the pipe and decrease rapidly as the wall is approached. The increase in gas flow increases both the bubble and average slug/bubble velocities. This increase is more pronounced in the central region of the pipe.

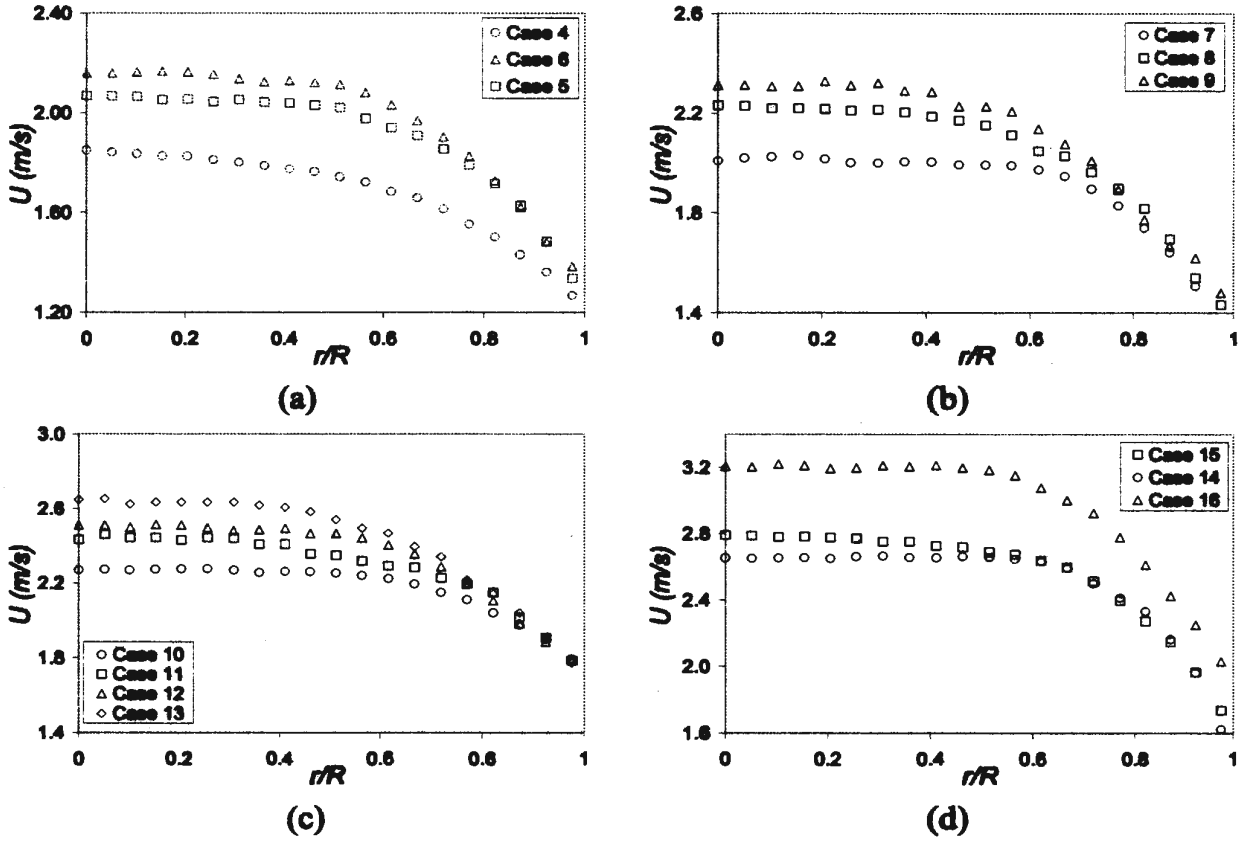

Figure 8.3 - Bubble velocity distribution for different U_G

(a) U_L=1.5 m/s: U_G= O 0.2 m/s, □ 0.34 m/s, Δ 0.46 m/s

(b) U_L= 1.65 m/s: U_G= O 0.2 m/s, □ 0.37 m/s, Δ 0.45 m/s

(c) U_L=2.05 m/s: U_G= O 0.18 m/s, □ 0.28 m/s, Δ 0.38 m/s, ◊ 0.45 m/s

(d) U_L=2.35 m/s: U_G= O 0.22 m/s, □ 0.29 m/s, Δ 0.45 m/s

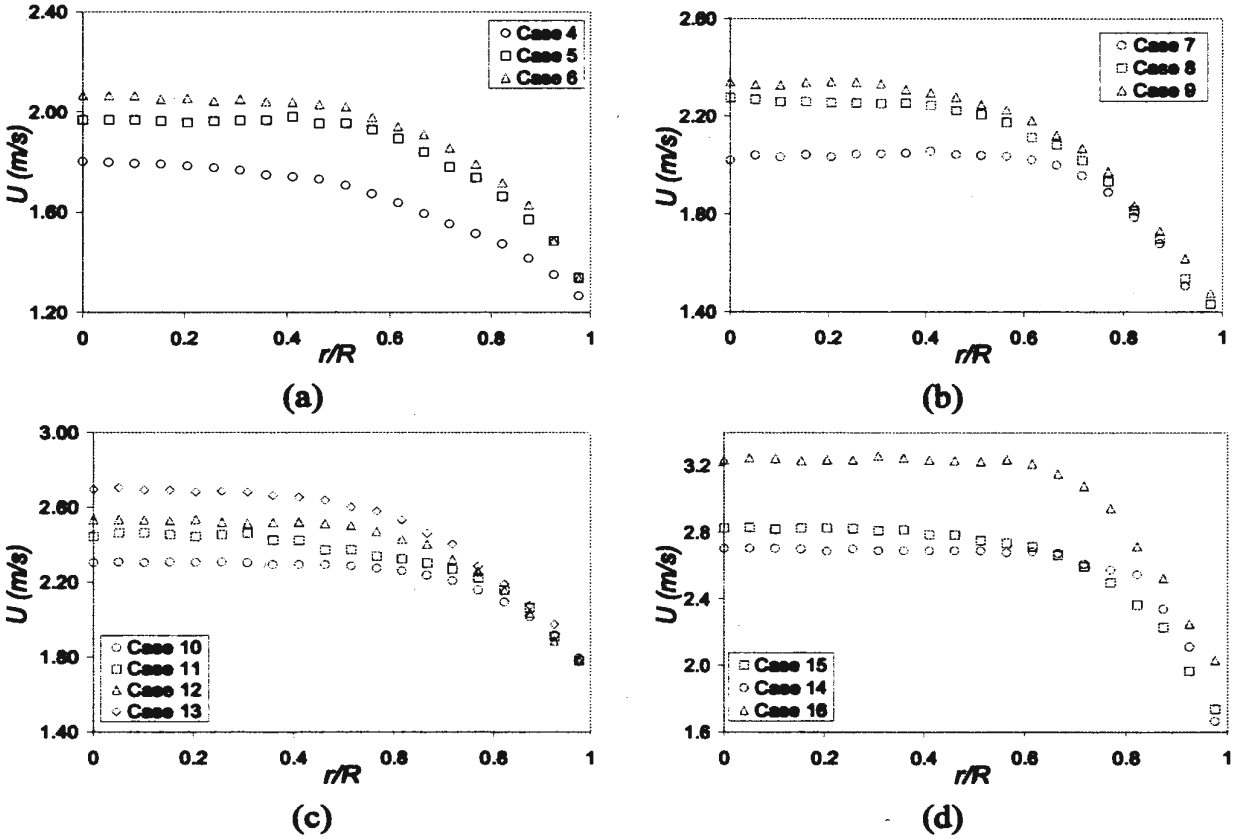

Figure 8.4 – Average slug/bubble velocity distribution for different U_G

(a) U_L=1.5 m/s: U_G= O 0.2 m/s, □ 0.34 m/s, Δ 0.46 m/s

(b) U_L= 1.65 m/s: U_G= O 0.2 m/s, □ 0.37 m/s, Δ 0.45 m/s

(c) U_L=2.05 m/s: U_G= O 0.18 m/s, □ 0.28 m/s, Δ 0.38 m/s, ◊ 0.45 m/s

(d) U_L=2.35 m/s: U_G= O 0.22 m/s, □ 0.29 m/s, Δ 0.45 m/s

With an increase in gas flow at a constant liquid flow, the bubble diameter increases (Figure 8.5). This is likely due to the increasing bubble coalescence resulting from the increasing gas concentration in the liquid. The same mechanism also accounts for the increase of slug length with the increasing gas flow (Figure 8.2). The bubble diameter distribution shows a central maximum, which is probably due to the fact that the larger bubbles tend to migrate into the central region of the pipe (Welle 1985).

The void fraction distributions are relatively constant in the central region and show steeper decrease as the measurement position traverses towards the wall (Figure

8.6). Generally, the effect of increasing the gas flow at constant liquid flow is to increase the void fraction, and this increase is more significant in the central region. The above phenomenon implies that the gas becomes more centrally concentrated at higher void fraction, which is also reflected by the distributions of bubble velocity and slug/bubble lengths. The central-maximum void fraction distribution was also reported by Welle (1985), and Moujaes and Sparks (1998) for vertically upward slug flows.

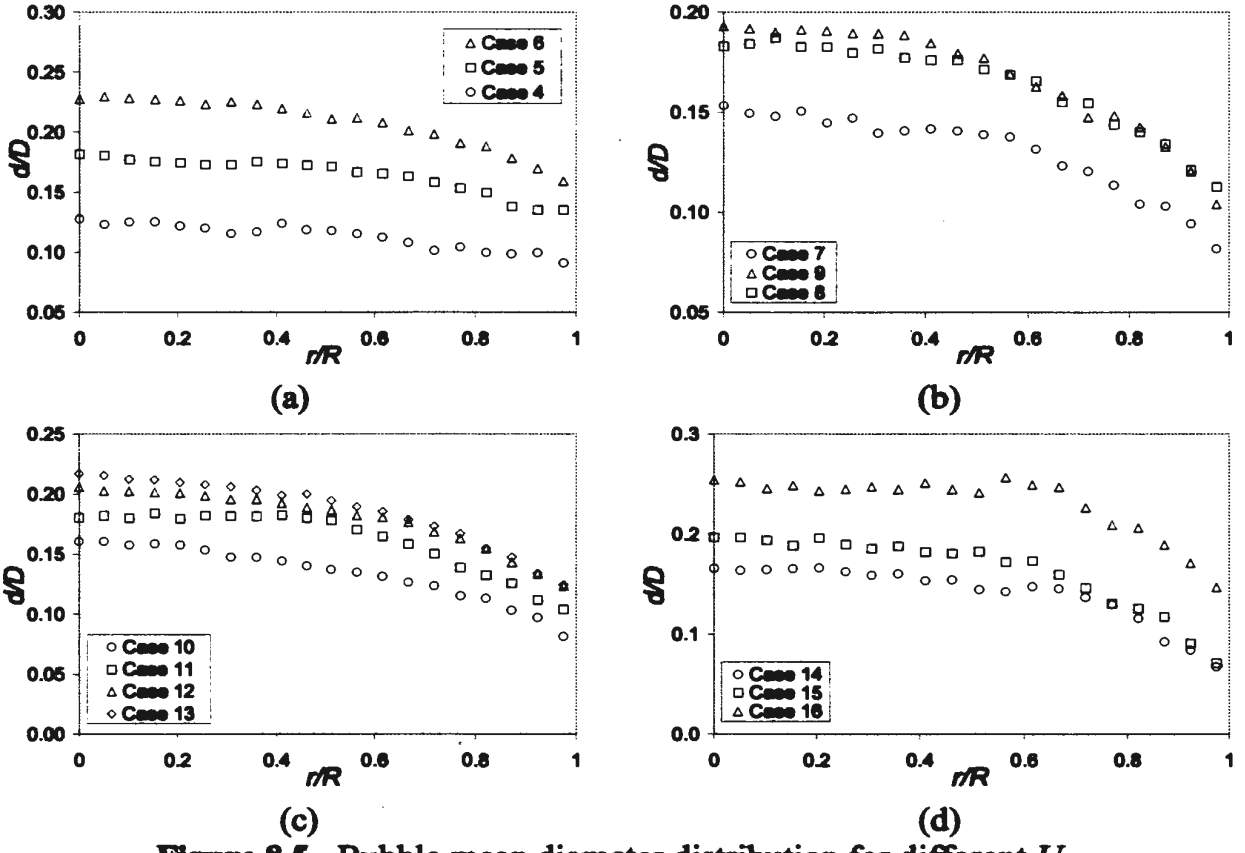

Figure 8.5 - Bubble mean diameter distribution for different U_G

(a) U_L=1.5 m/s: U_G= O 0.2 m/s, □ 0.34 m/s, Δ 0.46 m/s

(b) U_L= 1.65 m/s: U_G= O 0.2 m/s, □ 0.37 m/s, Δ 0.45 m/s

(c) U_L=2.05 m/s: U_G= O 0.18 m/s, □ 0.28 m/s, Δ 0.38 m/s, ◊ 0.45 m/s

(d) U_L=2.35 m/s: U_G= O 0.22 m/s, □ 0.29 m/s, Δ 0.45 m/s

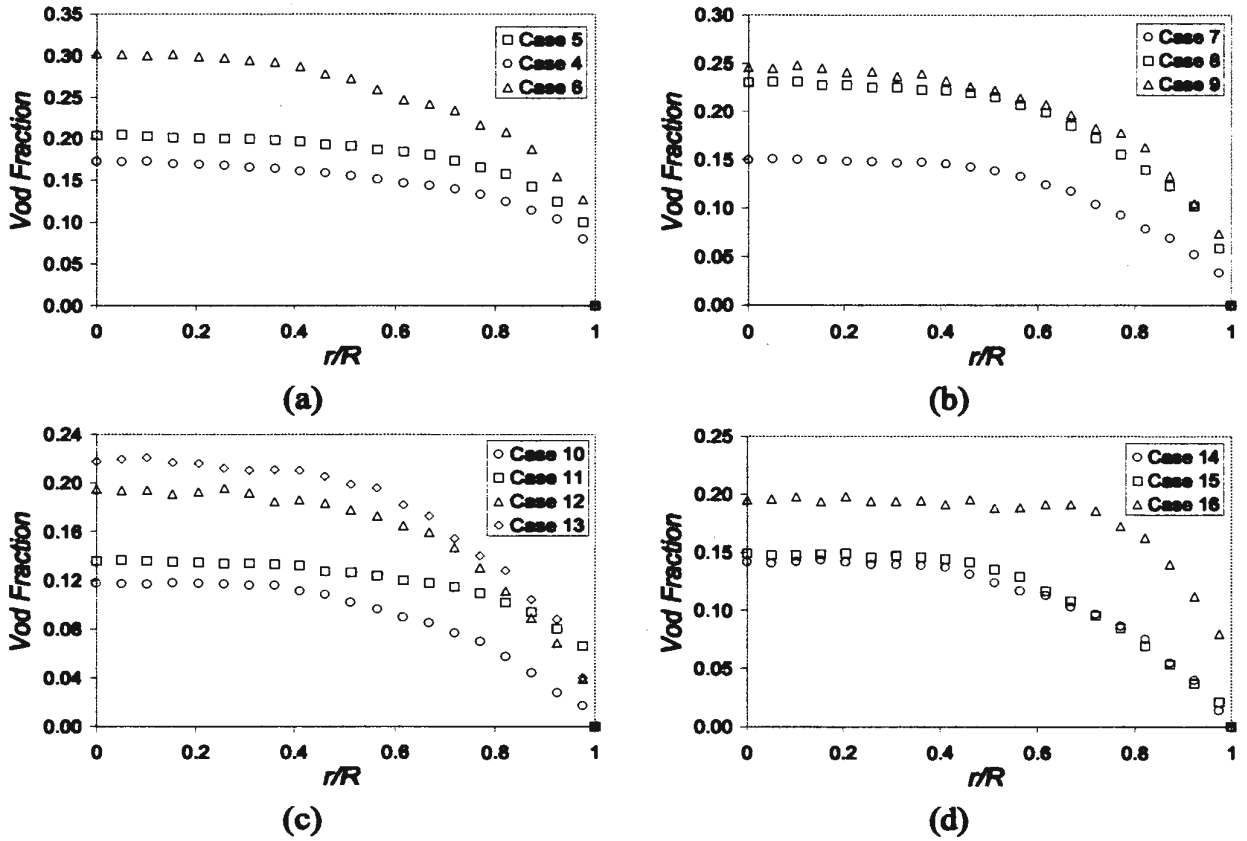

Figure 8.6 - Void fraction distribution for different U_G

(a) U_L=1.5 m/s: U_G= O 0.2 m/s, □ 0.34 m/s, Δ 0.46 m/s

(b) U_L= 1.65 m/s: U_G= O 0.2 m/s, □ 0.37 m/s, Δ 0.45 m/s

(c) U_L=2.05 m/s: U_G= O 0.18 m/s, □ 0.28 m/s, Δ 0.38 m/s, ◊ 0.45 m/s

(d) U_L=2.35 m/s: U_G= O 0.22 m/s, □ 0.29 m/s, Δ 0.45 m/s

Slug and bubble frequencies for the four flow series are provided in Figures 8.7 and 8.8, respectively. The slug frequency distributions achieve a maximum in the central region, whereas the bubble frequency distributions are relatively flat. The increase in gas flow increases both the slug and bubble frequencies. Consequently, this promotes the coalescence of air bubbles, which results in larger slug/bubbles at higher gas flow (see Figures 8.2 and 8.5). The majority of the air bubbles are small bubbles, which can explain why the average bubble/slug velocity calculated by the cross correlation is closer to the bubble velocity.

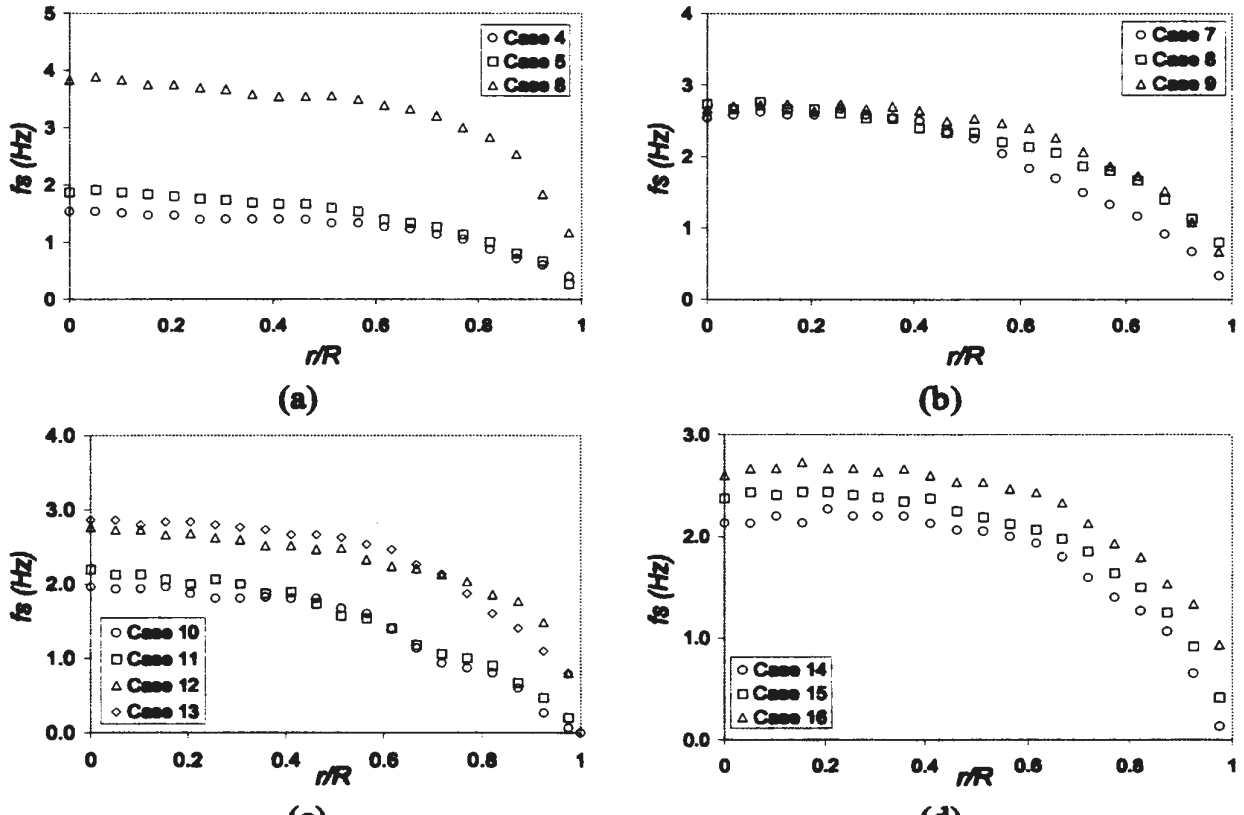

Figure 8.7 - Slug frequency distribution for different U_G

(a) U_L=1.5 m/s: U_G= O 0.2 m/s, □ 0.34 m/s, Δ 0.46 m/s

(b) U_L= 1.65 m/s: U_G= O 0.2 m/s, □ 0.37 m/s, Δ 0.45 m/s

(c) U_L=2.05 m/s: U_G= O 0.18 m/s, □ 0.28 m/s, Δ 0.38 m/s, ◊ 0.45 m/s

(d) U_L=2.35 m/s: U_G= O 0.22 m/s, □ 0.29 m/s, Δ 0.45 m/s

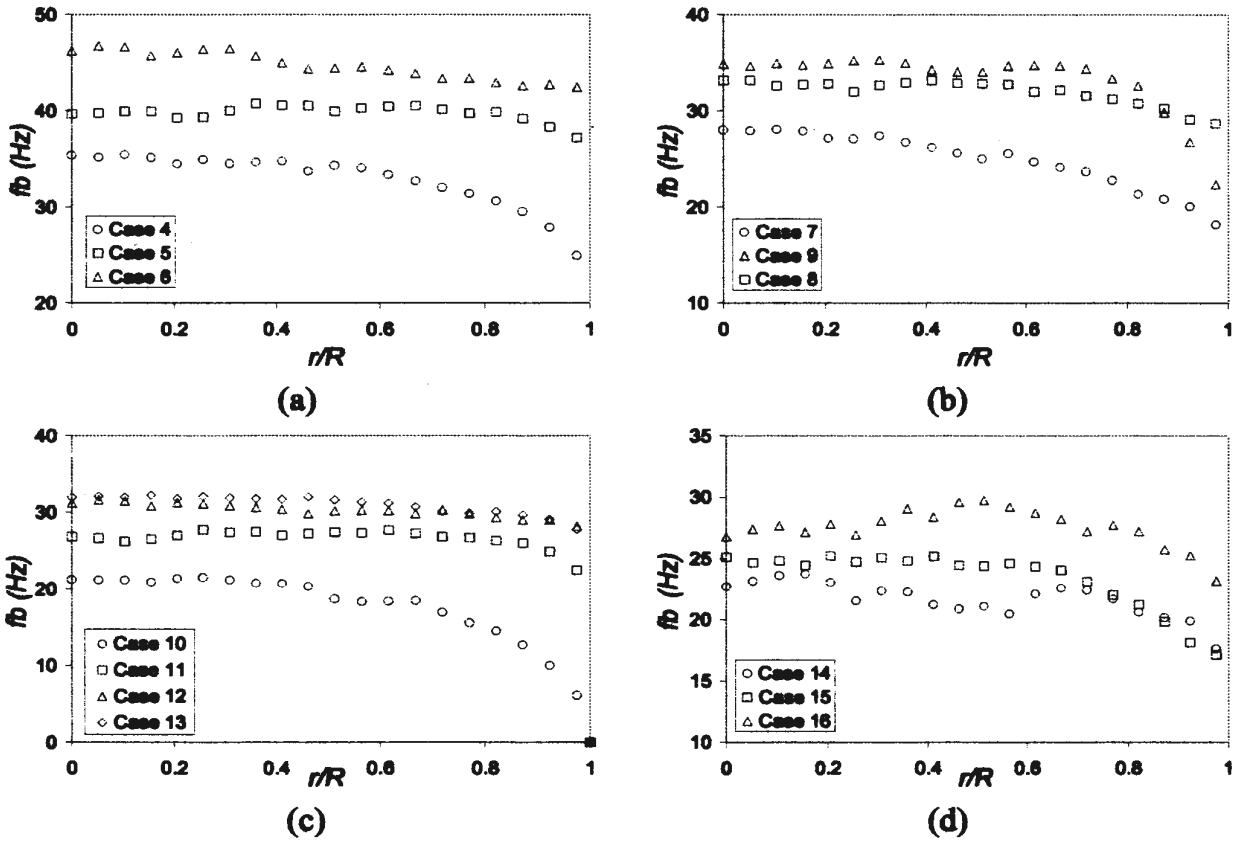

Figure 8.8 - Bubble frequency distribution for different U_G

(a) U_L=1.5 m/s: U_G= O 0.2 m/s, □ 0.34 m/s, Δ 0.46 m/s

(b) U_L= 1.65 m/s: U_G= O 0.2 m/s, □ 0.37 m/s, Δ 0.45 m/s

(c) U_L=2.05 m/s: U_G= O 0.18 m/s, □ 0.28 m/s, Δ 0.38 m/s, ◊ 0.45 m/s

(d) U_L=2.35 m/s: U_G= O 0.22 m/s, □ 0.29 m/s, Δ 0.45 m/s

The slug void fractions for the four flow series are presented in Figure 8.9. With the increase in gas flow, the slug void fraction increases. The central-maximum distribution of the slug void fraction provides further evidence for the central migration of gas slugs.

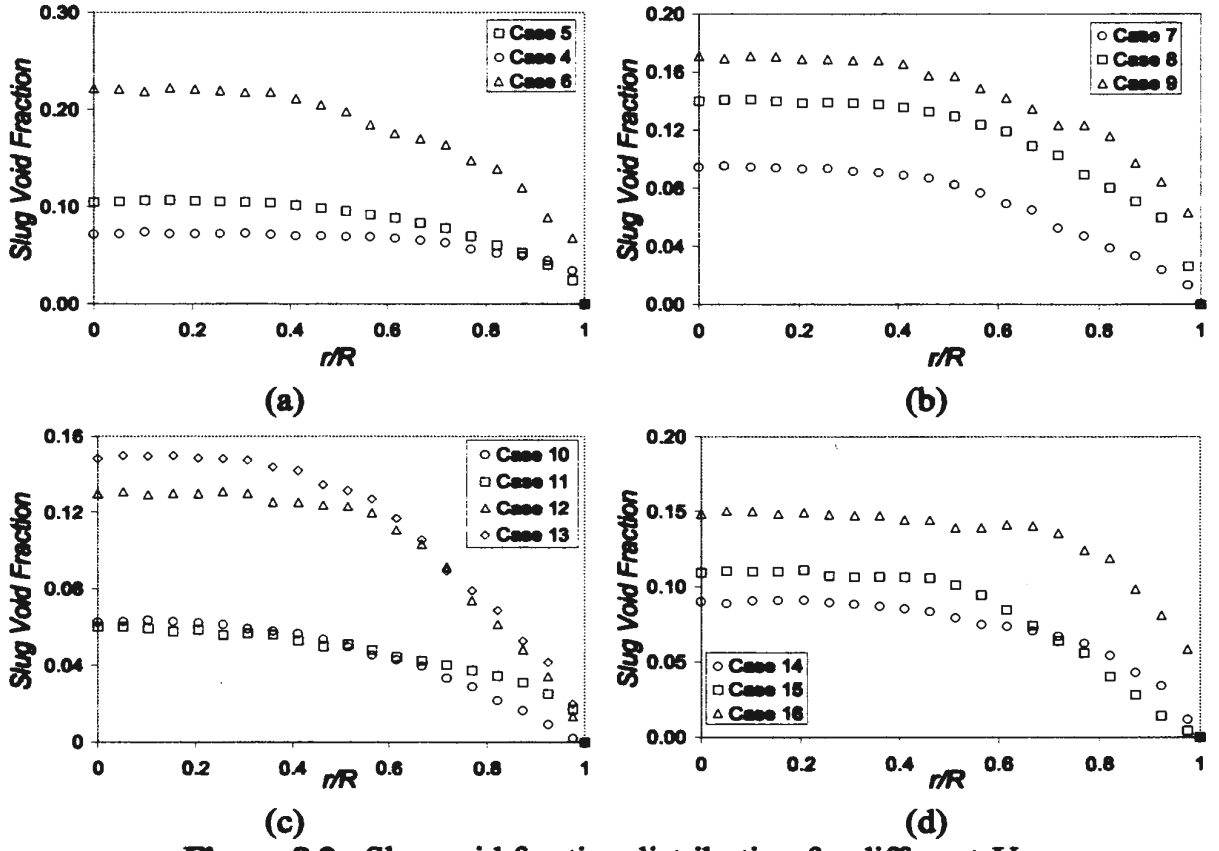

Figure 8.9 - Slug void fraction distribution for different U_G

(a) U_L=1.5 m/s: U_G= O 0.2 m/s, □ 0.34 m/s, Δ 0.46 m/s
(b) U_L= 1.65 m/s: U_G= O 0.2 m/s, □ 0.37 m/s, Δ 0.45 m/s
(c) U_L=2.05 m/s: U_G= O 0.18 m/s, □ 0.28 m/s, Δ 0.38 m/s, ◊ 0.45 m/s
(d) U_L=2.35 m/s: U_G= O 0.22 m/s, □ 0.29 m/s, Δ 0.45 m/s

Interfacial area concentrations for the four flow series are shown in Figure 8.10. A fairly uniform distribution with a relatively rapid decrease at the wall region is observed for all the four flow series. The increase in gas flow at a constant liquid flow generally increases the interfacial area concentration.

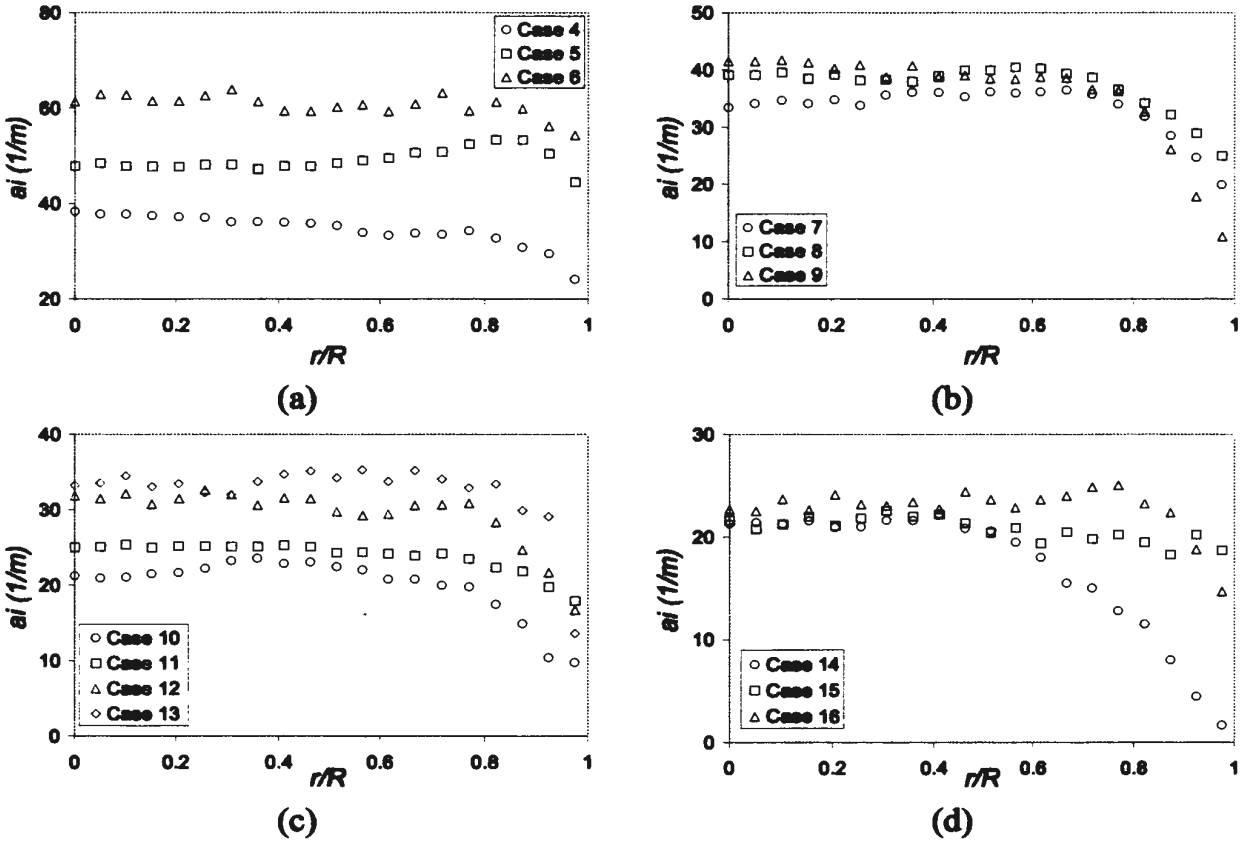

Figure 8.10 - Interfacial area concentration distribution for different U_G

(a) U_L=1.5 m/s: U_G= O 0.2 m/s, □ 0.34 m/s, Δ 0.46 m/s

(b) U_L= 1.65 m/s: U_G= O 0.2 m/s, □ 0.37 m/s, Δ 0.45 m/s

(c) U_L=2.05 m/s: U_G= O 0.18 m/s, □ 0.28 m/s, Δ 0.38 m/s, ◊ 0.45 m/s

(d) U_L=2.35 m/s: U_G= O 0.22 m/s, □ 0.29 m/s, Δ 0.45 m/s

Very little information has been found on the interfacial area concentrations for slug flow. The most relevant work is probably that performed by Tataoka et al. (1986). Tataoka et al. (1986) poropsed a three-probe measurement technique to estimate the interfacial area concentration of dispersed bubble flow in terms of the number of interfaces per unit length and the harmonic mean of $cos\theta_j$, where θ_j is the angle between the normal vector of the *jth* interface and the averaging direction. They also attempted to use this technique to measure the interfacial area concentration of a test slug flow case. They showed that for the slug flow with superficial liquid and gas velocities as 1.03 m/s and 0.402 m/s, the interfacial area concentration presents a central-maximum distribution,

about 200 m^{-1} in the pipe center and gradually decreasing to 130 m^{-1} close to the wall (Tataoka et al. 1986). The resultant interfacial area concentrations are significantly higher than those reported in the current work. The large discrepancy is natural as indicated by Tataoka et al. (1986) that the interfacial area concentration for slug flow is limited by the gas slugs, and that the three-probe method developed for bubble flows would overestimate the interfacial area concentration for slug flow.

8.1.2 Effect of Superficial Liquid Velocity on Slug Flow

Flow data for the following three flow series: cases 8, 12, 18, cases 2, 7, 14, 17 and cases 3, 6, 13, 16, were collected at different superficial liquid velocities for a constant gas flow rate to determine the effect of U_L on the flow characteristics. The discrepancy in superficial gas velocity among the cases for each flow series is within ±4% of the desired value. The liquid superficial velocity ranges from 1 m/s to 2.63 m/s.

As expected, the slug velocity and length are fairly uniform across the cross section of the pipe (Figures 8.11 and 8.12). The slug velocity increases with the increasing superficial liquid velocity for all the three series. With the increase in liquid flow, the slug length decreases for case 1. The increase in liquid flow at a constant gas flow reduces the gas volume fraction. This, in turn, reduces the probability of bubble coalescence, and results in smaller gas slugs at higher liquid flow rate.

Flow series 2 and 3 show a different flow behavior as the liquid flow increases. For flow series 2, the slug length decreases between cases 2 and 7 and between cases 14 and 17. For flow series 3, with increasing liquid flow, the slug length decreases between

cases 3 and 6, but increases between cases 13 and 16. There seems to be a discontinuity in flow regime between cases 7 and 14 as well as between cases 6 and 16.

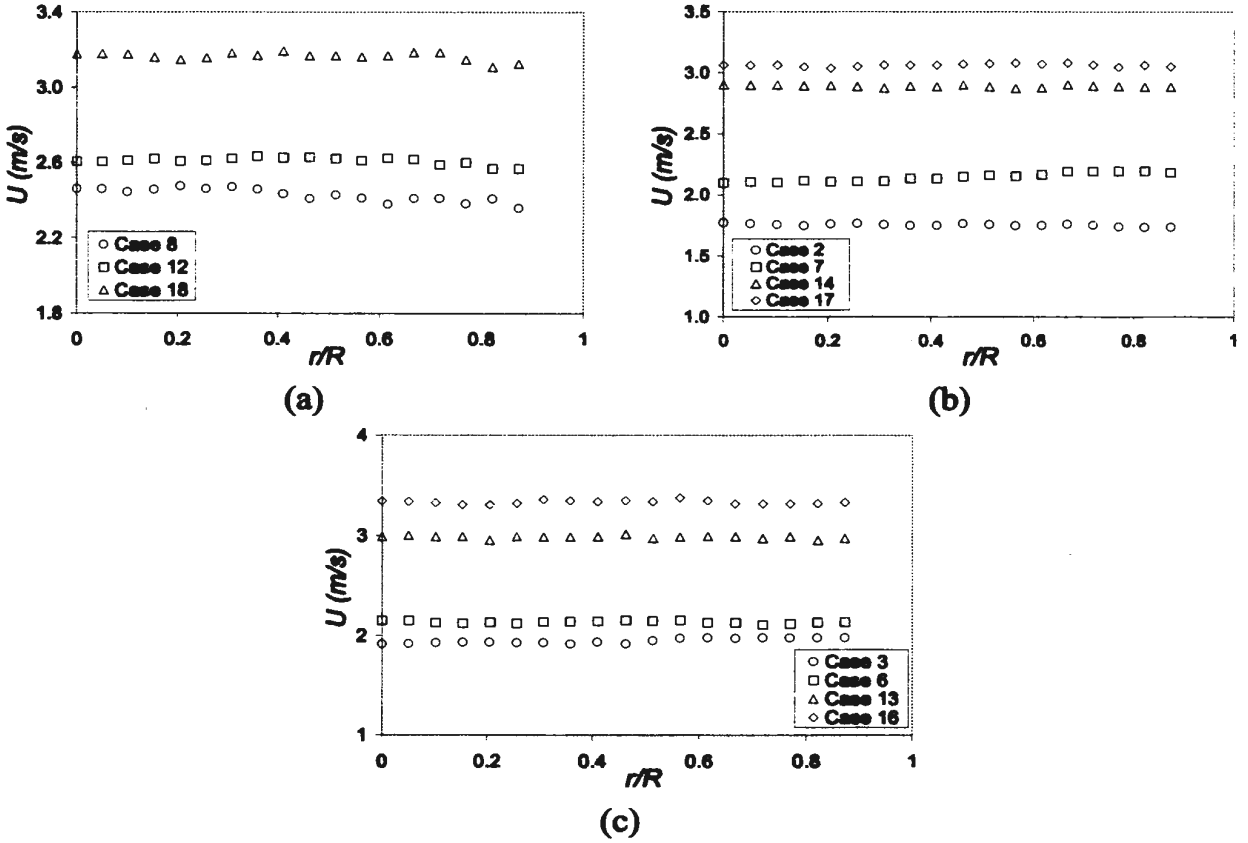

Figure 8.11 - Slug velocity distribution for different U_L
(a) U_G=0.37 m/s: U_L= O 1.64 m/s, □ 2.04 m/s, Δ 2.6 m/s
(b) U_G=0.21 m/s: U_L= O 1.07 m/s, □ 1.68 m/s, Δ 2.3 m/s, ◊ 2.63 m/s
(c) U_G=0.45 m/s: U_L= O 1.14 m/s, □ 1.5 m/s, Δ 2.06 m/s, ◊ 2.35 m/s

The flow regime difference (or discontinuity) in slug flow was noticed by Bendiksen (1984) for horizontal two-phase flow. He suggested that the slug flow may be more conveniently divided into two sub-regimes with different flow features. The flow features for the two sub-regimes have not yet been fully characterized or defined (Kokal and Stanislav 1989, Paglianti et al. 1996). Bendiksen (1984) proposed that the discontinuity between the two sub-regimes for horizontal slug flow could be

characterized by a critical Froude number of the mixture ($Fr = V_m / \sqrt{gD}$). Paglianti et al. (1996) also observed the different flow characteristics in horizontal slug flow and showed that the application of slug flow models to the whole slug flow regime may lead to errors in the estimation of slug length and other flow parameters. For air-water horizontal slug flow, Paglianti et al. (1996) suggested that the critical Froude number is about 3. The concept of sub-regime was also postulated to characterize the discontinuities in slug length and slug and bubble frequencies observed in the current work.

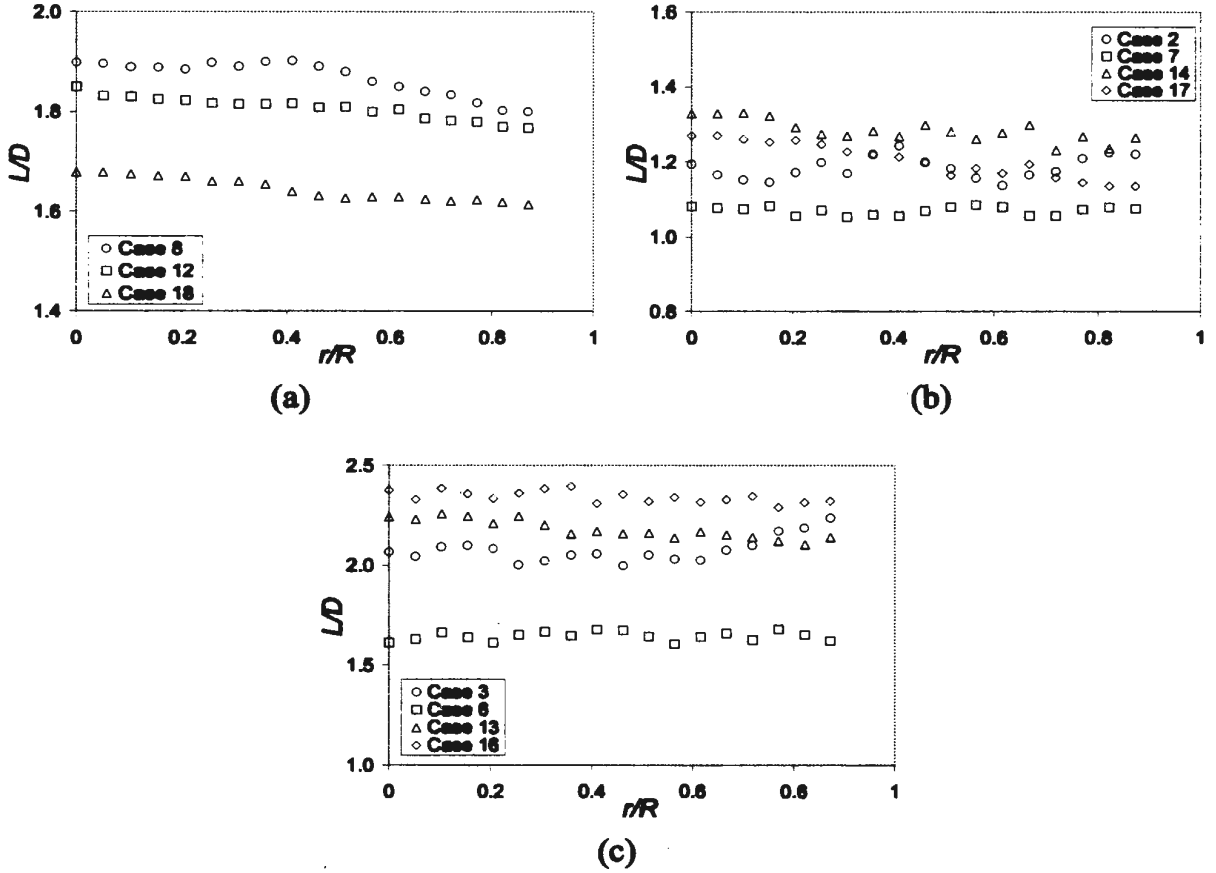

Figure 8.12 - Slug length distribution for different U_L

(d) U_G=0.37 m/s: U_L= O 1.64 m/s, □ 2.04 m/s, Δ 2.6 m/s

(e) U_G=0.21 m/s: U_L= O 1.07 m/s, □ 1.68 m/s, Δ 2.3 m/s, ◊ 2.63 m/s

(f) U_G=0.45 m/s: U_L= O 1.14 m/s, □ 1.5 m/s, Δ 2.06 m/s, ◊ 2.35 m/s

Cases 2 and 7 in series 2 may be in a different sub-regime with cases 14 and 17. For series 3, cases 3 and 6 may be in a different sub-regime with cases 13 and 16. The existence of these flow discontinuities is also evident in the slug and bubble frequencies presented later. A critical Froude number can also be used to define the discontinuity in the flow regime. Similar to the critical Froude number proposed by Paglianti et al. (1996), the critical Froude number for the current measurements is found to be in the vicinity of 3. The different characteristics for the different sub-regimes were not attempted to investigate since they are not the focus of the current work.

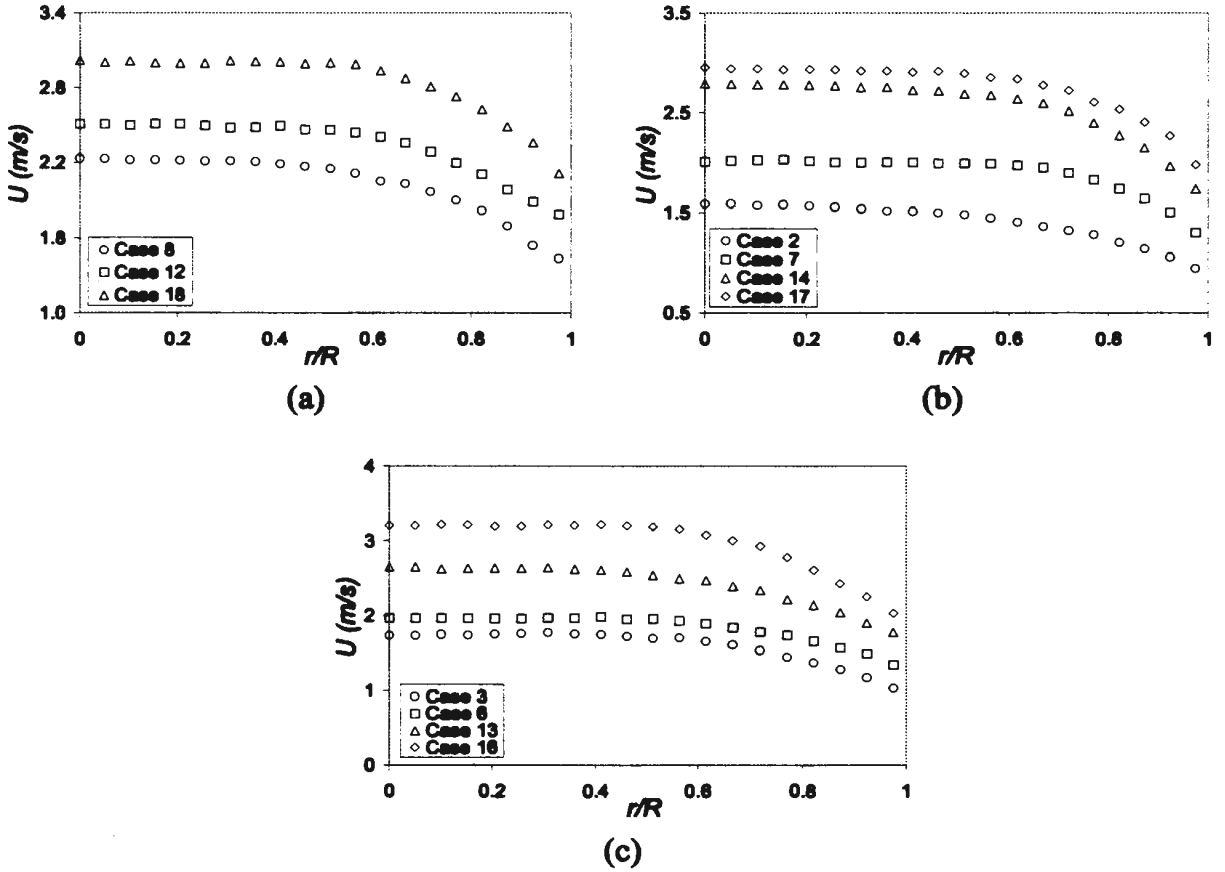

Figure 8.13 - Bubble velocity distribution for different U_L

(g) U_G=0.37 m/s: U_L= O 1.64 m/s, □ 2.04 m/s, Δ 2.6 m/s

(h) U_G=0.21 m/s: U_L= O 1.07 m/s, □ 1.68 m/s, Δ 2.3 m/s, ◊ 2.63 m/s

(i) U_G=0.45 m/s: U_L= O 1.14 m/s, □ 1.5 m/s, Δ 2.06 m/s, ◊ 2.35 m/s

The bubble velocity and average slug/bubble velocity distributions (Figures 8.13 and 8.14) of these flows have a similar profile as those presented in Figures 8.3 and 8.4 in section 8.11. The bubble and average slug/bubble velocity profiles are fairly uniform up to r/R=0.6, and then decrease rapidly as the wall is approached, due to the higher drag experienced in this region. With the increasing superficial liquid velocity, both the bubble and average slug/bubble velocities increase in general, and with more significant increases in the central region of the pipe.

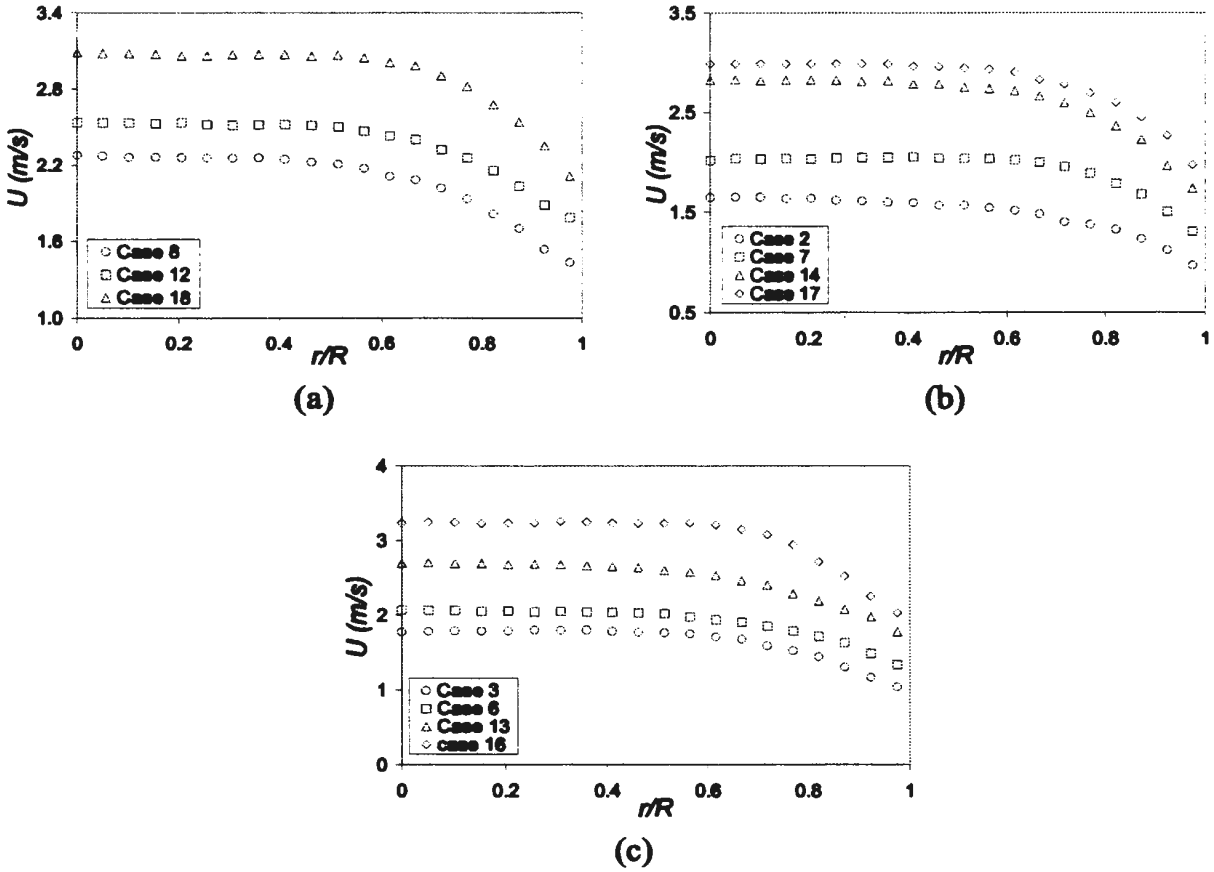

Figure 8.14 – Average slug/bubble velocity distribution for different U_L
(j) U_G=0.37 m/s: U_L= O 1.64 m/s, □ 2.04 m/s, Δ 2.6 m/s
(k) U_G=0.21 m/s: U_L= O 1.07 m/s, □ 1.68 m/s, Δ 2.3 m/s, ◊ 2.63 m/s
(l) U_G=0.45 m/s: U_L= O 1.14 m/s, □ 1.5 m/s, Δ 2.06 m/s, ◊ 2.35 m/s

At a constant gas flow rate, increasing the liquid flow rate reduces the gas volume fraction. The bubble diameter distribution seems to be closely related to the local gas volume fraction (Figure 8.15). The bubble diameter for flow series 1 increases as the liquid velocity increases (Figure 8.15a). It is also true for flow series 2 (Figure 8.15b) and 3 (Figure 8.15c), although there exists a flow regime discontinuity among the flow cases for the two flow series.

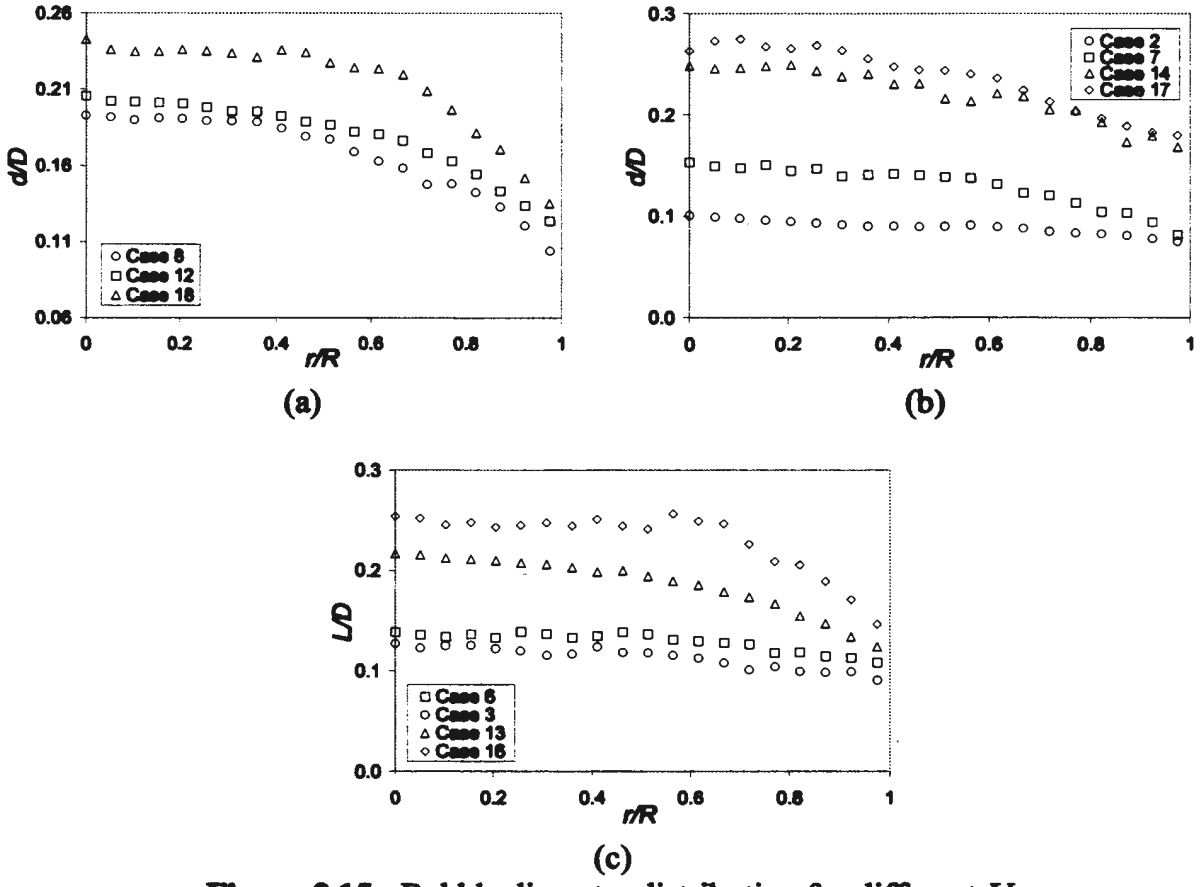

Figure 8.15 - Bubble diameter distribution for different U_L
(m) U_G=0.37 m/s: U_L= O 1.64 m/s, □ 2.04 m/s, Δ 2.6 m/s
(n) U_G=0.21 m/s: U_L= O 1.07 m/s, □ 1.68 m/s, Δ 2.3 m/s, ◊ 2.63 m/s
(o) U_G=0.45 m/s: U_L= O 1.14 m/s, □ 1.5 m/s, Δ 2.06 m/s, ◊ 2.35 m/s

Increasing the liquid flow at a constant gas flow rate decreases the void fraction (Figure 8.16). The void fraction distribution shows a maximum in the central region of

the pipe. Again, the distributions of the void fractions for the 3 series imply that the gas slugs and bubbles become more centrally concentrated at higher void fractions.

The local gas concentration shows an influence on both the slug and bubble frequency distributions. The slug and bubble frequency distributions for the three flow series show a maximum in the central region of the pipe (Figures 8.17 and 8.18). The frequency distribution of bubbles is flatter than that of slugs.

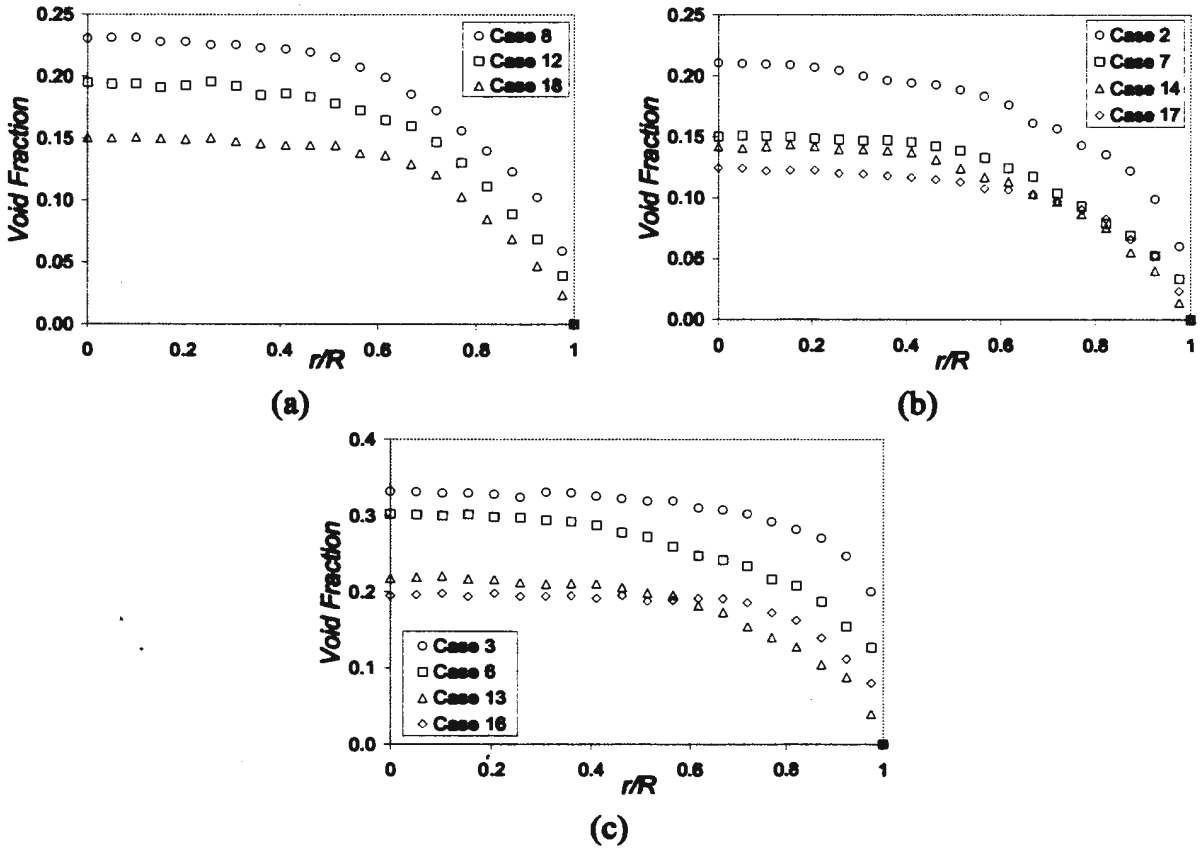

Figure 8.16 - Void fraction distribution for different U_L

(p) U_G=0.37 m/s: U_L= O 1.64 m/s, □ 2.04 m/s, Δ 2.6 m/s

(q) U_G=0.21 m/s: U_L= O 1.07 m/s, □ 1.68 m/s, Δ 2.3 m/s, ◊ 2.63 m/s

(r) U_G=0.45 m/s: U_L= O 1.14 m/s, □ 1.5 m/s, Δ 2.06 m/s, ◊ 2.35 m/s

With an increasing liquid flow, the slug frequency for series 1 is relatively constant (Figure 8.17a). The discontinuity between cases 7 and 14 for series 2 (Figure

8.17b) and cases 6 and 13 for series 3 (Figure 8.17c) is apparent, with the slug frequency increasing with increasing liquid flow within the two sub-regimes.

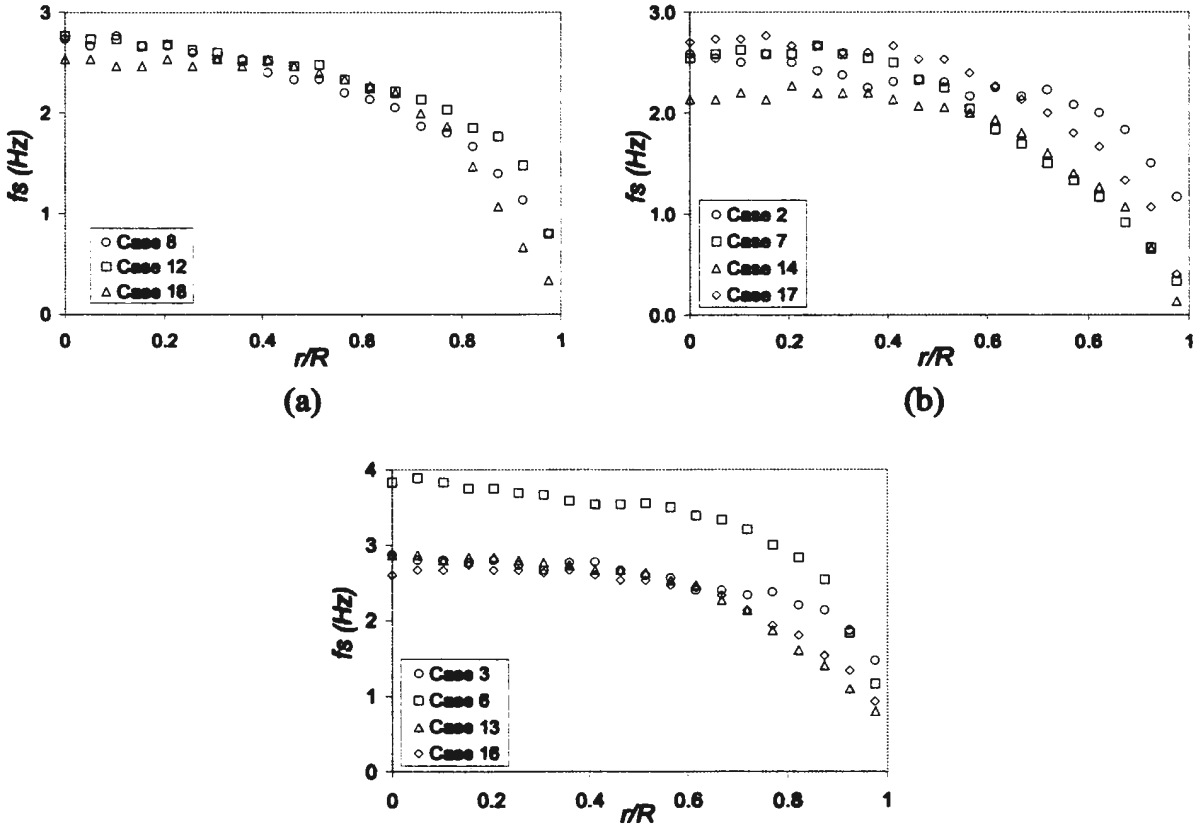

Figure 8.17 - Slug frequency distribution for different U_L
(s) U_G=0.37 m/s: U_L= O 1.64 m/s, □ 2.04 m/s, Δ 2.6 m/s
(t) U_G=0.21 m/s: U_L= O 1.07 m/s, □ 1.68 m/s, Δ 2.3 m/s, ◊ 2.63 m/s
(u) U_G=0.45 m/s: U_L= O 1.14 m/s, □ 1.5 m/s, Δ 2.06 m/s, ◊ 2.35 m/s

The bubble frequency decreases with increasing liquid flow for flow series 1 (Figure 8.18a) and within the two sub-regimes for series 3 (Figure 8.18c). However, for series 2 (Figure 8.18b), between cases 2 to 7, the bubble frequency decreases with increasing liquid flow, whereas between cases 14 and 17, the bubble frequency increases with increasing liquid flow. The reason for the different variations of bubble frequency within the sub-regimes for the two flow series is not clearly understood.

The slug void fraction distributions for the three flow series decrease with the increasing liquid flow (Figure 8.19). As expected, the distributions of the slug void fraction are similar to those in Figure 8.9. The gas slugs carry most of the gas volume for the three flow series. Considering the distributions of slug length, slug void fraction, slug frequency, bubble diameter and bubble frequency, a more central-maximum void fraction distribution at the higher gas flow as shown in Figure 8.16 is expected.

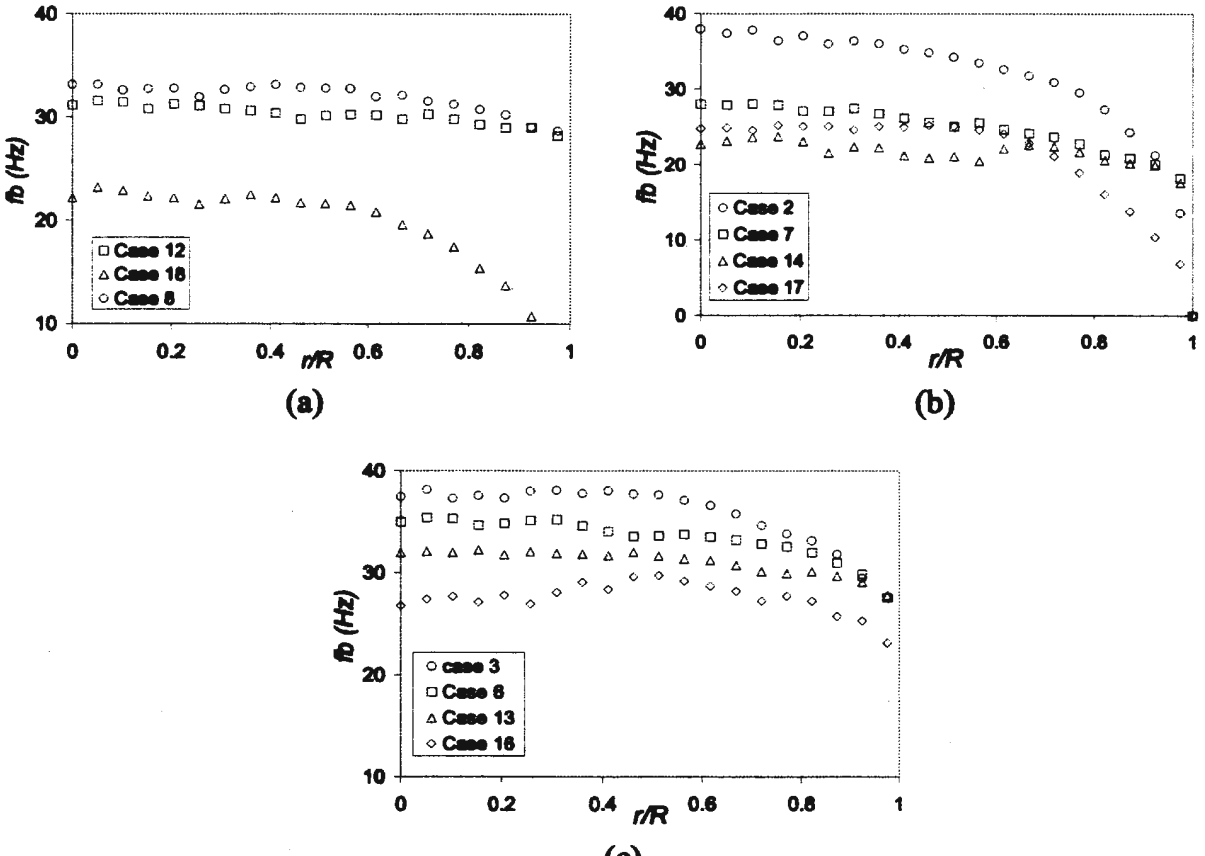

Figure 8.18 - Bubble frequency distribution for different U_L

(v) U_G=0.37 m/s: U_L= O 1.64 m/s, □ 2.04 m/s, Δ 2.6 m/s

(w) U_G=0.21 m/s: U_L= O 1.07 m/s, □ 1.68 m/s, Δ 2.3 m/s, ◊ 2.63 m/s

(x) U_G=0.45 m/s: U_L= O 1.14 m/s, □ 1.5 m/s, Δ 2.06 m/s, ◊ 2.35 m/s

The interfacial area concentrations for the three series are showed in Figure 8.20. Similar to the profiles shown in Figure 8.10, the distributions are fairly constant in the

central region of the pipe. The flow sub-regimes do not show a significant impact on the distribution of interfacial area concentration, as it continuously decreases with the increase in liquid flow.

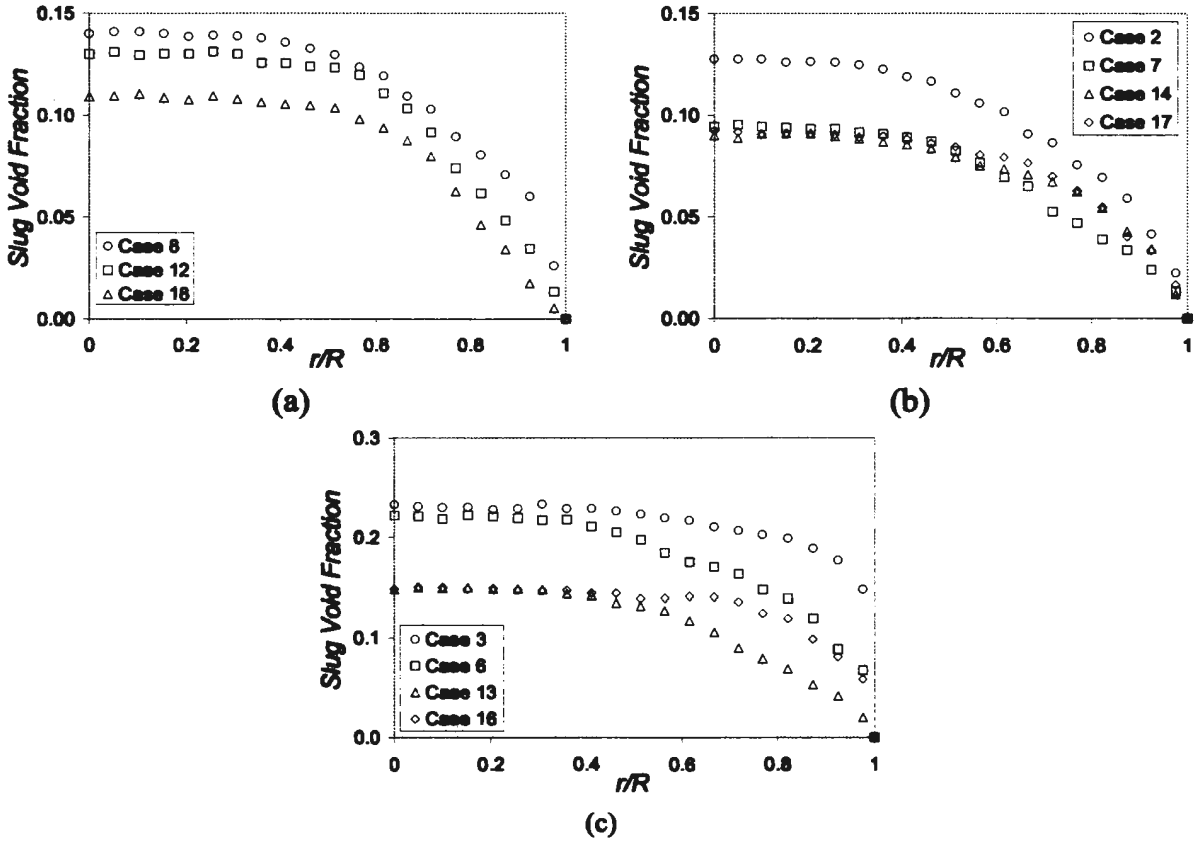

Figure 8.19 - Slug void fraction distribution for different U_L
(y) U_G=0.37 m/s: U_L= O 1.64 m/s, □ 2.04 m/s, Δ 2.6 m/s
(z) U_G=0.21 m/s: U_L= O 1.07 m/s, □ 1.68 m/s, Δ 2.3 m/s, ◊ 2.63 m/s
(aa) U_G=0.45 m/s: U_L= O 1.14 m/s, □ 1.5 m/s, Δ 2.06 m/s, ◊ 2.35 m/s

From the current measurements, the existance of flow sub-regimes for vertically upward slug flow is quite evident. Different flow behaviors, particularly in slug length, slug and bubble frequencies were observed in the two sub-regimes. Other flow paramters such as void fraction, slug velocity, average bubble/slug velocity, bubble diameter and interfacial area concentration seems to be insensitive to the flow sub-regimes. Since the

present flow conditions only cover a limited flow ranges, a general rule to charaterize the different sub-regimes cannot be derived.

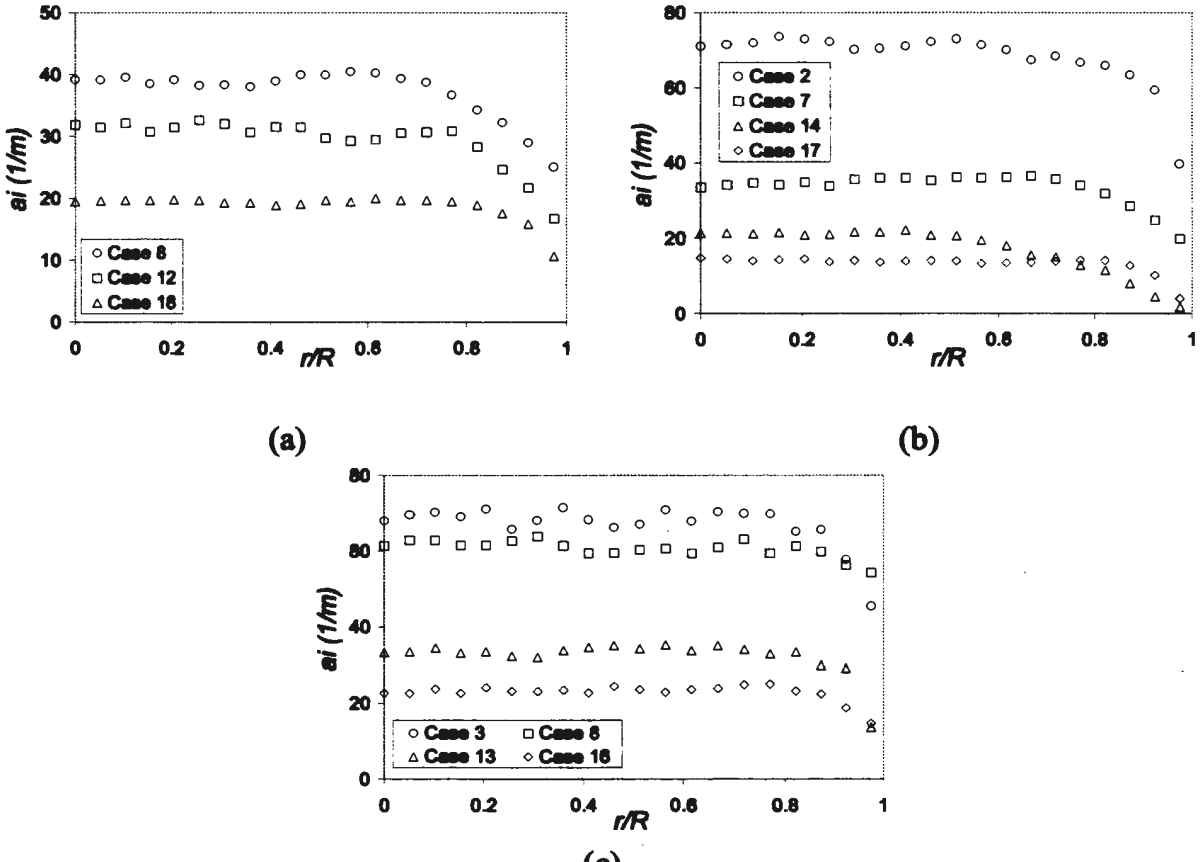

Figure 8.20 - Interfacial area concentration distribution for different U_L
(bb) U_G=0.37 m/s: U_L= O 1.64 m/s, □ 2.04 m/s, Δ 2.6 m/s
(cc) U_G=0.21 m/s: U_L= O 1.07 m/s, □ 1.68 m/s, Δ 2.3 m/s, ◊ 2.63 m/s
(dd) U_G=0.45 m/s: U_L= O 1.14 m/s, □ 1.5 m/s, Δ 2.06 m/s, ◊ 2.35 m/s

8.2 Correlations for Slug Flow

8.2.1 Void Fraction

The prediction of void fraction from the volume flow ratio is desirable, because the volume flow ratio is usually available. Figure 8.21 provides a correlation between the global void fraction and the volume flow ratio, β, for the 18 flow cases. The flow data

suggests a strong linear relationship. The coefficient of correlation is 0.93, and the standard deviation is 0.014. The resultant correlation equation is:

$$\varepsilon = 0.974 \cdot \beta \tag{8-1}$$

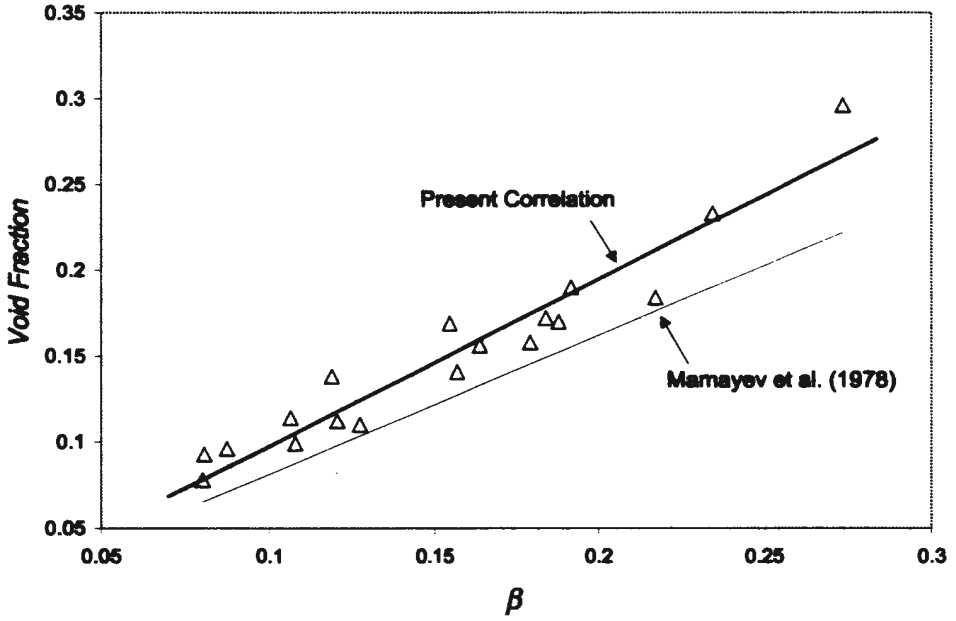

Figure 8.21 - Correlation between global void fraction and β [Δ Present data]

A linear correlation was also reported by Mamayev et al. (1978) and is provided in Figure 8.21. They showed that for large values of Froude number, a coefficient of 0.81 can be used to correlate the global void fraction with the volume flow ratio (Mamayev et al. 1978). It should be noted that the correlation proposed by Mamayev et al. (1978) underestimates the current void fraction. The discrepancy is natural, however, since this coefficient is measurement location dependent for vertical flow. The coefficient varies with phase slip (see equation 2-7), and the phase slip is expected to increase along the

streamwise direction. Also, the Froude number of the current work is relatively small (less than 3.5).

It is useful to correlate the slug void fraction, slug/bubble sizes and slug/bubble frequencies with the physical properties of the flow. The mean slug void fraction, ε_b, can be correlated with the global void fraction, ε, as:

$$\varepsilon_s = 0.61 \cdot \varepsilon \tag{8-2}$$

Figure 8.22 shows the above correlation, along with the current 18 flow data. The coefficient of this linear correlation is 0.82, and the standard deviation is 0.017.

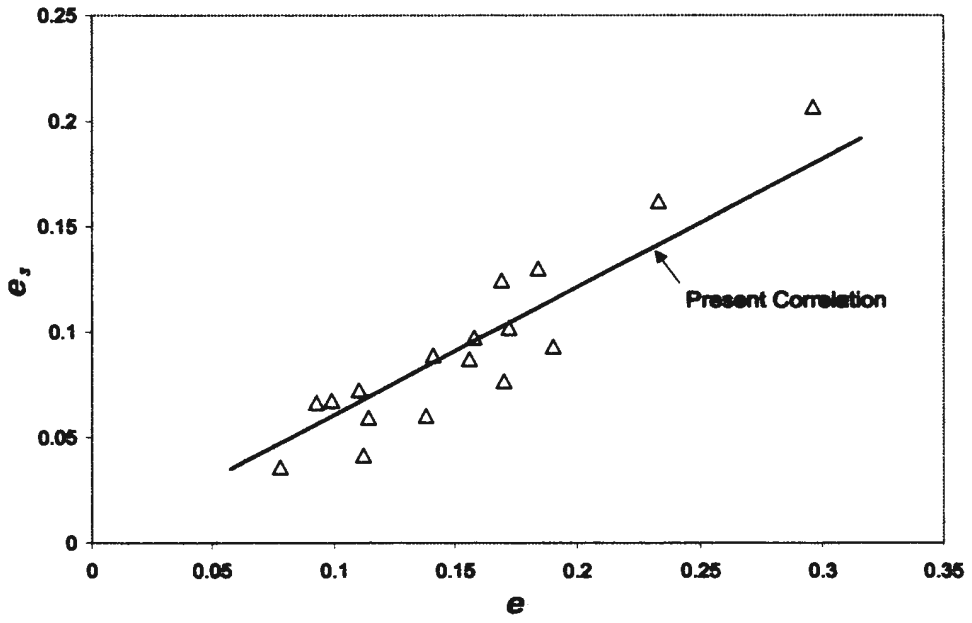

Figure 8.22 - Correlation between global void fraction and mean slug void fraction [Δ Present data]

8.2.2 Slug/bubble Length and Frequency

Slug flow is characterized by the stochastic alternation of large Taylor bubbles flowing over a thin liquid film and liquid slugs containing gas bubbles; it exhibits different flow characteristics depending on the value of the superficial velocity (Kokal and Stanislav 1989). Slug length and frequency have been used to study horizontal two-phase slug flow (Maron et al. 1982, Tronconi 1991). A model to calculate the slug length for horizontal gas-liquid slug flow was first proposed by Maron et al. (1982). Later, Dukler et al. (1985) improved this model by introducing a correction factor to account for the viscous wall effects. For horizontal gas-liquid slug flow, the slug length is often correlated with Froude number of the mixture in various forms (Dukler and Hubbard 1975, Dukler et al. 1985, Nicholson et al. 1978, Paglianti et al. 1996).

Prediction of bubble diameter under various flow conditions has been investigated for many years. Taylor (1934) probably made the first fundamental experiments on the break-up of drops and bubbles under the action of external viscous and surface stresses. Fundamental studies on the break-up of drops and bubbles by surface forces and dynamic pressures were also made by several other investigators (Hinze 1955, Kolmogorov 1949, Sevik 1973, Sleicher 1962). Recently, Kocamustafaogullari et al. (1994) investigated several bubble break-up mechanisms for horizontal two-phase flow and concluded that the average pressure fluctuations generated by turbulent liquid fluctuations acting across a bubble diameter are the only mechanism which causes distortion of a bubble. Based on this force, and the competing surface tension force, Kocamustafaogullari et al. (1994) developed a theoretical model for predicting the mean bubble size for horizontal two-phase bubble flow. They correlated bubble diameter with the Weber number of the

continuous phase, the ratio of kinematic viscosities of the two phases, and Kolmogorov length scale (Kocamustafaogullari et al. 1994). Although various correlations have been proposed to predict slug/bubble sizes and their frequencies, attempts to develop new correlations and improve the existing correlations have continued, because of the considerable errors associated with the existing models.

There has been very little research on the corresponding vertically upward slug flows. Without specifically dealing with the detailed flow mechanism and turbulent structure, a simple dimensional analysis indicates that the slug/bubble sizes and frequencies for air-water two-phase flow can be expressed as a function of the Froude number of the liquid, the superficial gas and liquid velocity ratio and a dimensionless density term. Based on this analysis, models for predicting slug/bubble sizes and bubble frequency were developed for vertical air-water slug flow. Figure 8.23 shows the correlation developed for slug length, which can be expressed as:

$$l/D = 1.271 \cdot Fr_L^{0.417} \cdot \left(\frac{U_G}{U_L}\right)^{1.046} \cdot \left(\frac{\Delta\rho}{\rho_G}\right)^{0.25} \tag{8-3}$$

or

$$l/D = 1.271 \cdot \frac{U_G^{1.046}}{(g \cdot D)^{0.417} U_L^{0.212}} \cdot \left(\frac{\Delta\rho}{\rho_G}\right)^{0.25} \tag{8-4}$$

The coefficient of correlation is 0.95, and the standard deviation is 0.09. Equation 8-4 indicates that the length of the gas slug increases with increasing superficial gas velocity and decreases with increasing superficial liquid velocity. The influence of superficial gas velocity on the slug length is more significant.

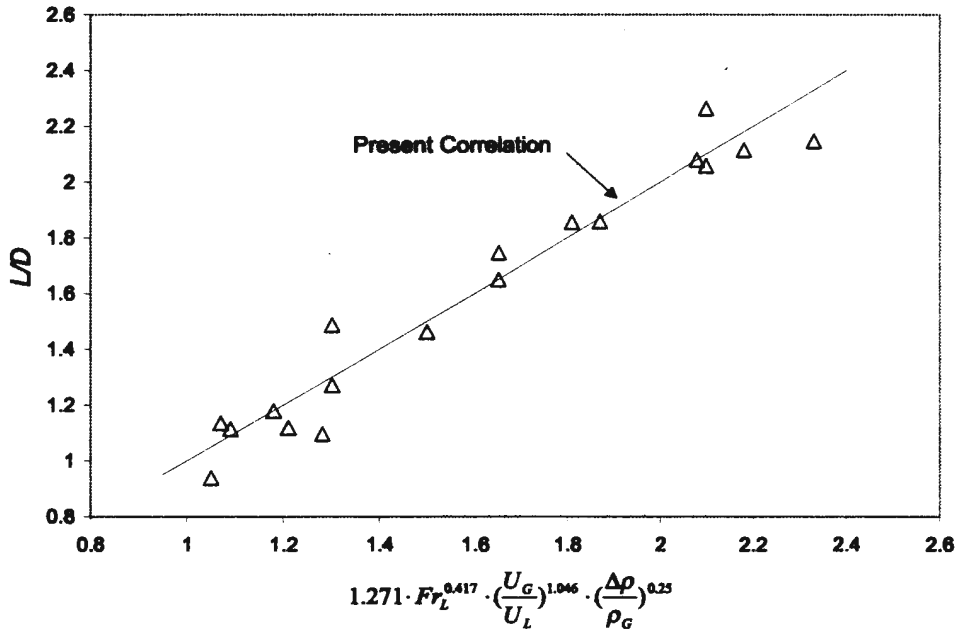

Figure 8.23 - Slug length correlation [Δ Present data]

It is difficult to use a single correlation to correlate the bubble diameter over the entire range of gas and liquid velocities of the current work. A better correlation accuracy can be achieved if the flow data are divided into two subgroups, based on the discontinuity among these flow cases as indicted in section 8.1.2. A Froude number of about 3 of the mixture is found to be appropriate for characterizing this discontinuity. The separation of flow sub-regimes with this Froude number is also reflected by the discussion presented in the previous sections. When $Fr < 3$, the bubble diameter can be estimated as:

$$d/D = 0.196 \cdot Fr_L^{-0.018} \cdot (\frac{U_G}{U_L})^{-0.473} \cdot (\frac{\Delta\rho}{\rho_G})^{-0.155} \qquad (8\text{-}5)$$

or

$$d/D = 0.196 \cdot \frac{U_L^{0.437}(gD)^{0.018}}{U_G^{0.473}} \cdot \left(\frac{\Delta\rho}{\rho}\right)^{-0.155} \tag{8-6}$$

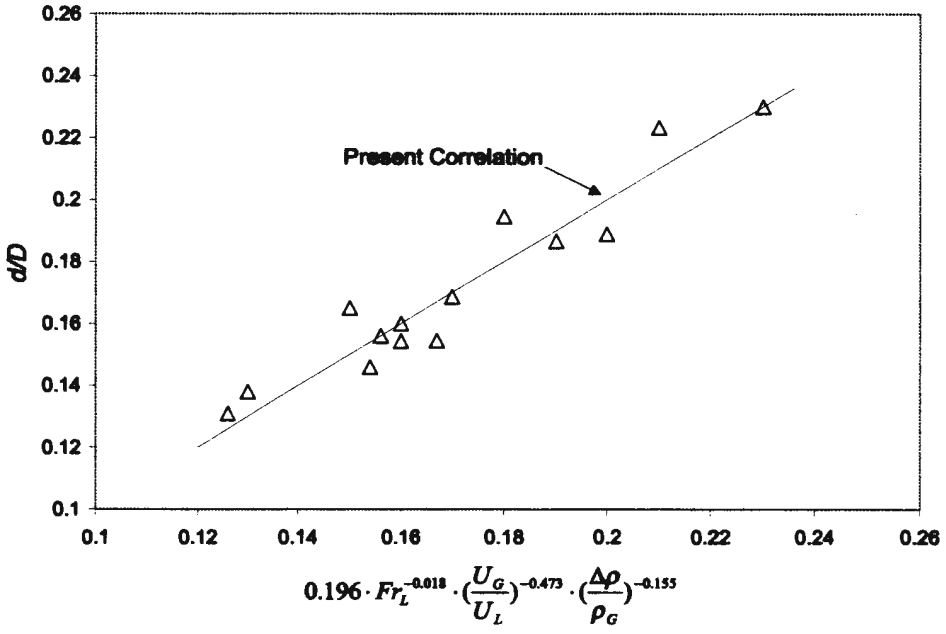

Figure 8.24 - Bubble diameter correlation [Δ Present data]

Equation 8-6 reveals that the bubble diameter increases with increasing superficial liquid velocity, and decreases with increasing superficial gas velocity. The influences of the two velocities on bubble diameter are fairly close. The present bubble diameter correlation and its comparison with the 14 flow data are shown in Figure 8.24. The correlation coefficient is 0.91, and the standard deviation is 0.008. When $Fr > 3$, the bubble diameter is more or less constant in the range of 0.2 – 0.22D. The bubble frequency can be correlated as:

$$f_b = 1.838 \cdot Fr_L^{-0.061} \cdot \left(\frac{U_G}{U_L}\right)^{0.516} \left(\frac{\Delta\rho}{\rho_G}\right)^{0.6} \tag{8-7}$$

or

$$f_b = 1.838 \cdot \frac{U_G^{0.516}(gD)^{0.061}}{U_L^{0.637}} \cdot \left(\frac{\Delta\rho}{\rho}\right)^{0.6} \qquad (8\text{-}8)$$

Figure 8.25 shows the present correlation for bubble frequency and its comparison with the present flow data. The coefficient of this correlation is 0.89, and the standard deviation 2.57 Hz. The bubble frequency increases with increasing superficial gas velocity and decreases with increasing superficial liquid velocity.

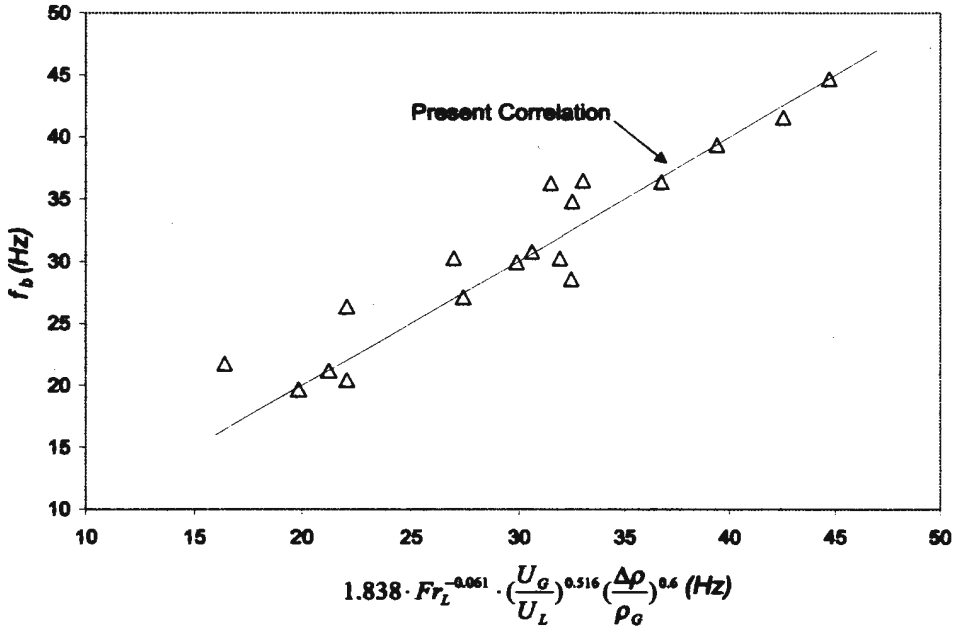

Figure 8.25 - Bubble frequency correlation [Δ Present data]

No apparent correlation can be formulated for the slug frequency of the current flow data. However, the slug frequency varies in the range of 1.2 to 3.1 Hz for the 18 flow cases.

8.2.3 Slug and Bubble Velocities

The local hot-film anemometry measurements were compared to the integrated local gross velocity with the superficial gas velocity directly measured by the gas flow meter. From the locally measured ε and u_b, the area-averaged gas velocity is defined as:

$$U_G^* = \frac{1}{A}\int_A \varepsilon \cdot u_G dA \tag{8-9}$$

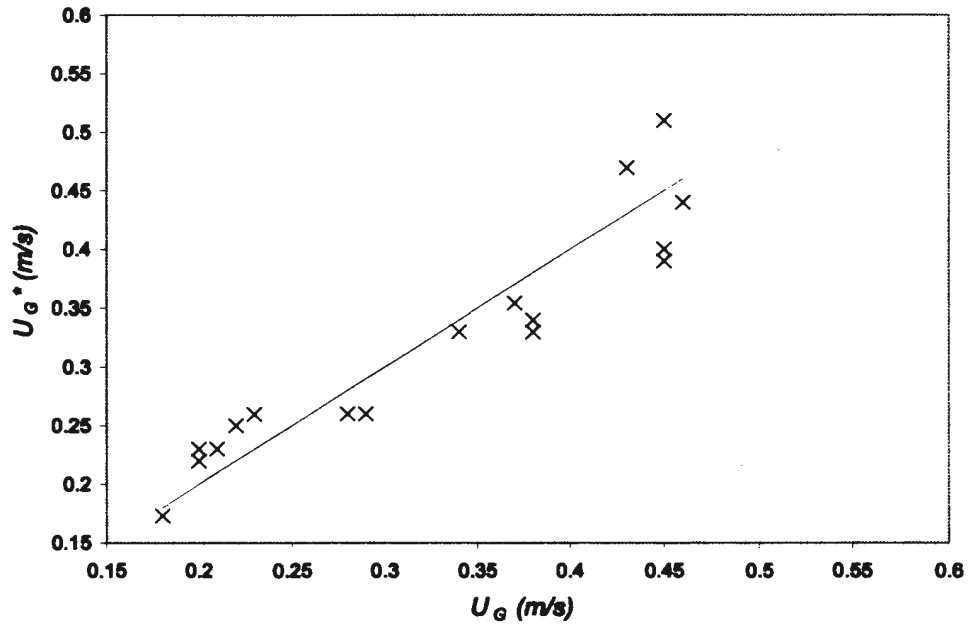

Figure 8.26 - Comparison between U_G and U_G^*

Measurements for all the 18 flow cases were checked and the comparisons are shown in Figure 8.26. The average discrepancy is 9.8% for the 18 flow conditions. The following reasons may account for the discrepancies:

1. Uncertainty in void fraction estimation by the data reduction method.
2. Uncertainties associated with measurements from the liquid and gas flow meters.

3. Uncertainties associated with pressure and temperature measurements.
4. Uncertainty associated with cross correlation analysis.

Nicklin et al. (1962) and Neal (1963) studied the rise velocity of Taylor bubbles in flowing water. Their experimental data indicated that the absolute rise velocity of a Taylor bubble is the sum of a term proportional to its rise velocity in a stagnant liquid and a term proportional to the velocity of the liquid. Mathematically, the rise velocity of Taylor bubbles, u_s, in flowing water can be expressed as:

$$u_s = C_0 \cdot U_M + U_{bs} \tag{8-10}$$

where U_M is the total superficial velocity, $U_{bs} = 0.346\sqrt{gD}$, is the rise velocity of Taylor bubbles in stagnant liquid, (Nicklin et al. (1962), and C_0 is the correction factor.

Nicklin et al. (1962) suggested that for liquid Reynolds numbers higher than 8000, 1.2 is the most appropriate value for C_0. The slug velocities estimated from the measurements are compared with equation 8-10, and the results are shown in Figure 8.27. The slug velocity values from the MUN flow loop are below the correlation suggested by Nicklin et al. (1962). This is probably because the correlation suggested by Nicklin et al. (1962) is valid for terminal slug velocity while the slugs measured at MUN are at L/D = 50. The corresponding value of C_0 for the present data is 1.0. This value is expected to increase with a higher measurement location (higher L/D ratio). The coefficient of this linear regression is 0.92, indicating a strong linear relationship between the two velocities. The standard deviation for this correlation is 0.13 m/s.

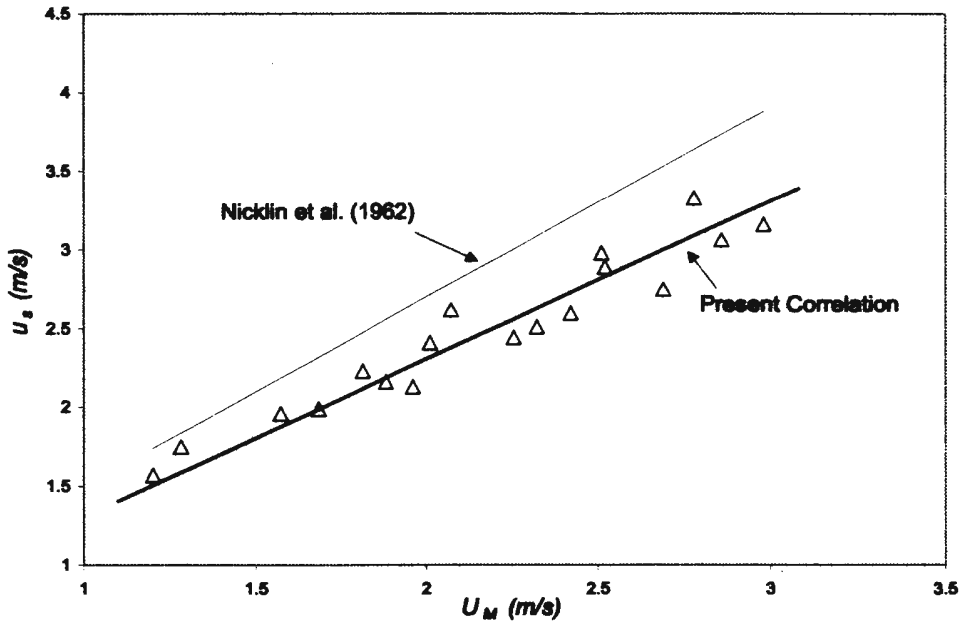

Figure 8.27 - Slug velocity correlation [Δ Present data]

Akagawa and Sakaguchi (1966) analyzed the small bubbles carried within the liquid slug of a slug flow in a 1.09-inch tube. They showed that the following empirical equation can be used for estimating the average velocity, u_b, of small bubbles in the liquid slug.

$$u_b = 1.10 \cdot U_M \tag{8-11}$$

Akagawa and Sakaguchi (1966) also found that the average velocity of the liquid slugs is $0.96U_M$. The study conducted by Schmidt et al. (1981) found that a value of 1.08 for equation 8-11 is most appropriate for correlating the two velocities measured in a 2-inch diameter pipe. They also found that the average velocity of the liquid slug is $0.92U_M$ rather than $0.96U_M$. The bubble mean velocity versus total superficial velocity is

presented in Figure 8.28. A linear relationship was assumed to correlate the two velocities. A coefficient of 0.99, instead of 1.10, results from the correlation. The correlation coefficient is 0.97 with a standard deviation of 0.08 m/s. The current flow data lie below the correlation proposed by Akagawa and Sakaguchi (1966). Again, this is probably due to the fact that the flows at L/D = 50 have not yet reached the terminal velocity. The bubble velocities are expected to increase at higher measurement locations.

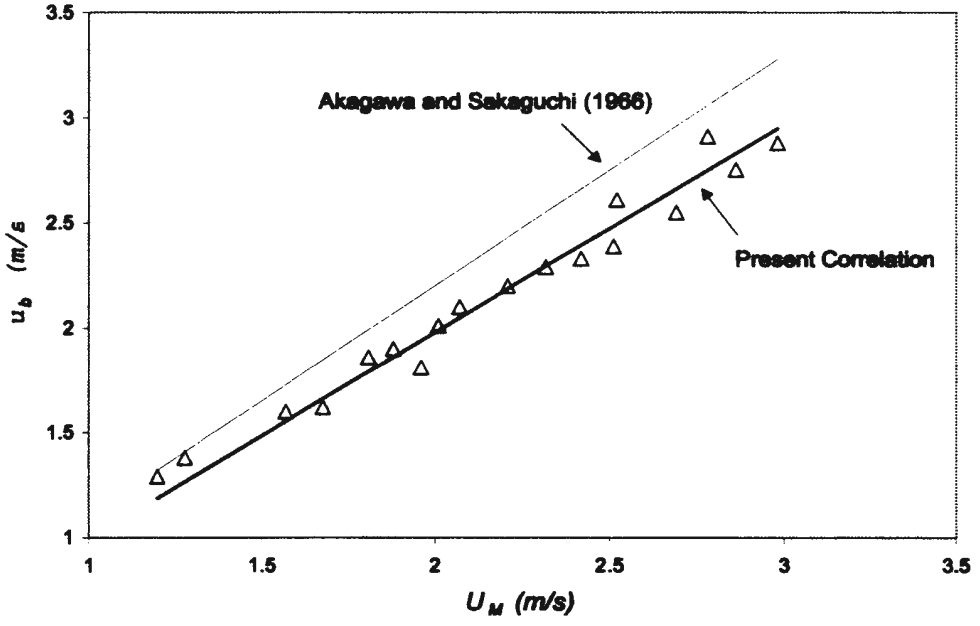

Figure 8.28 - Mean bubble velocity correlation [Δ Present data]

The mean liquid slug velocity can be estimated from the continuity equation. If the slug flow is modeled as a series of air slugs having the diameter of the pipe separated by liquid slugs with dispersed small air bubbles, the total volume flow rate should be equal to the sum of the volume flow rates of the air bubbles, air slug and liquid slug.

$$q_G + q_L = q_s + q_b + q_{LS} \tag{8-12}$$

By substituting each term with in equation 8-12 with a time-averaged velocity, multiplied by its corresponding void fraction and pipe cross section area, the following results:

$$A \cdot U_G + A \cdot U_L = A \cdot \bar{u}_s \cdot \bar{\varepsilon}_s + A \cdot \bar{u}_b \cdot \bar{\varepsilon}_b + A \cdot \bar{u}_{LS}(1 - \bar{\varepsilon}_s - \bar{\varepsilon}_b) \tag{8-13}$$

where $\bar{u}_s$, $\bar{u}_b$ and $\bar{u}_{LS}$ are the time-average velocities of the air slugs, bubbles and liquid slugs, respectively. Therefore, the velocity of liquid slugs can be calculated by rearranging equation 8-13 as:

$$\bar{u}_{LS} = \frac{U_G + U_L - \bar{u}_s\bar{\varepsilon}_s - \bar{u}_b\bar{\varepsilon}_b}{1 - \bar{\varepsilon}_b - \bar{\varepsilon}_s} \tag{8-14}$$

The correlation of the average liquid slug velocity with total superficial velocity is provided in Figure 8.29. Standard regression shows that the mean liquid slug velocity is $0.98U_M$, which is a little higher than the values suggested by Akagawa and Sakaguchi (1966) and Schmidt et al. (1981). The coefficient of this linear correlation is 0.99 and the standard deviation of this correlation is 0.04 m/s. The average velocity slip in the liquid slug is 1.01.

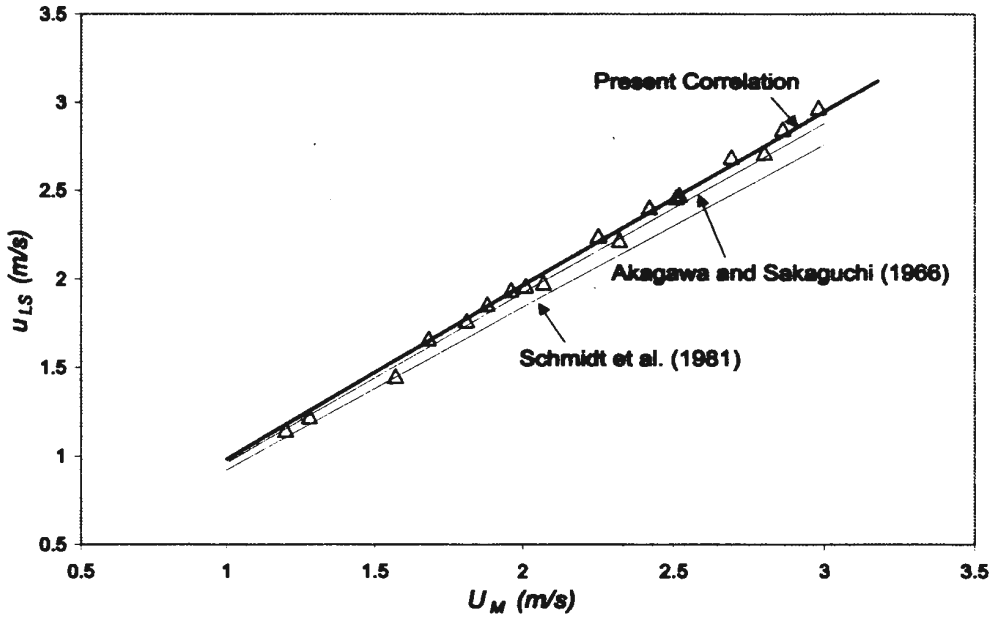

Figure 8.29 - Mean liquid slug velocity correlation [Δ Present data]

8.2.4 Interfacial Area Concentration

The quantitative flow information obtained through this study allows the development of an empirical interfacial area concentration equation for vertically upward slug flow. The average interfacial area concentrations measured are compared with the models proposed by Tabie et al. (1981), and Zeitou et al. (1994), respectively. The comparisons are provided in Figures 8.30 and 8.31. It is evident that both models overestimate the interfacial area concentrations for slug flows. In addition, the data do not show a sufficiently strong correlation. The poor agreements may be attributed to the fact that the two models were developed based on bubble flow. Very little information is available on interfacial area concentration models for slug flow. The need for developing a correlation that is suitable for vertically upward air-water slug flows is important.

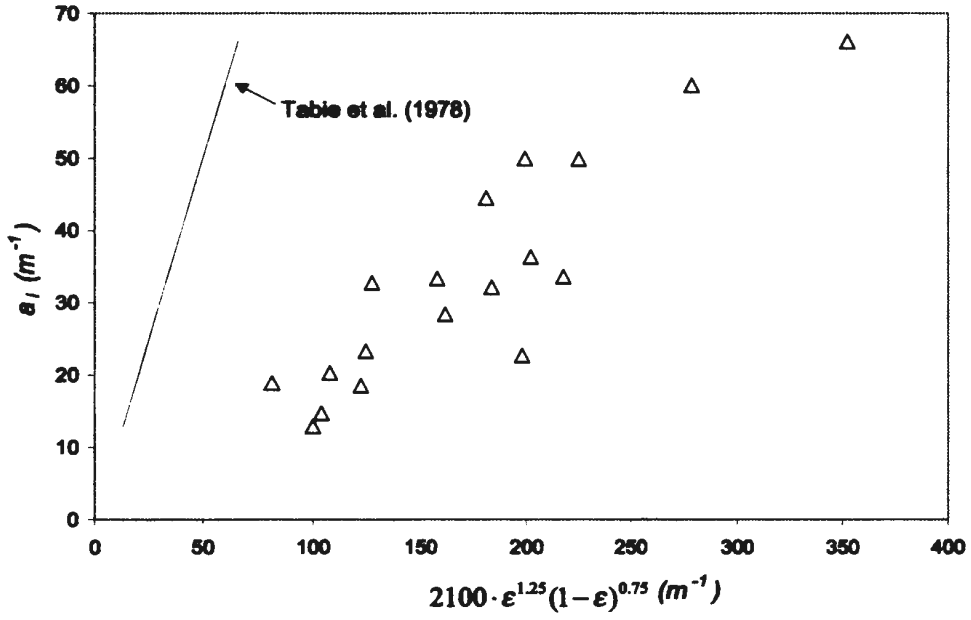

Figure 8.30 - Comparison of a_i with the model of Tabie et al. (1978) [Δ Present data]

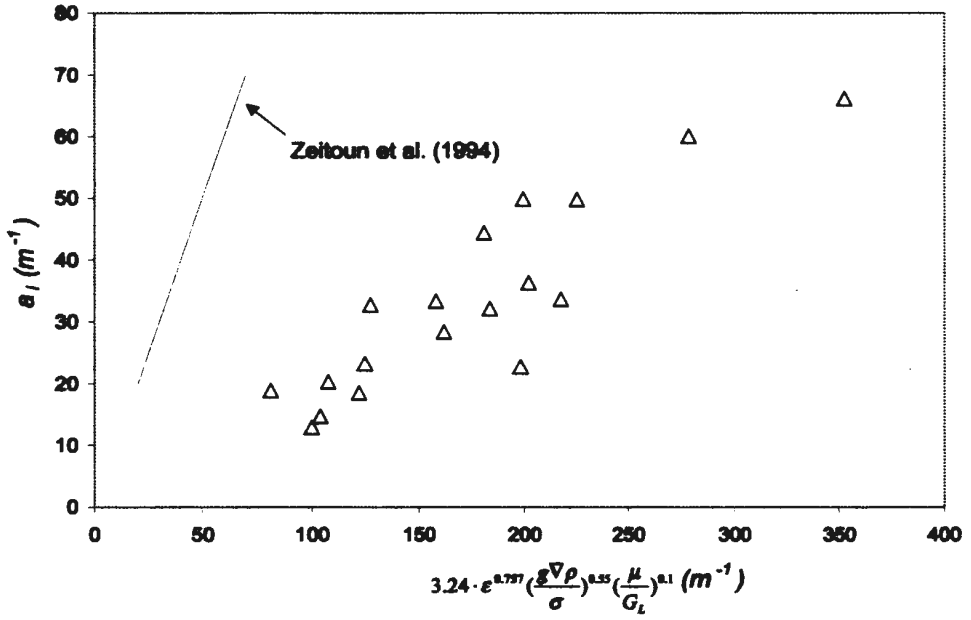

Figure 8.31 - Comparison of a_i with model of Zeitoun et al. (1994) [Δ Present data]

Equation 5-12, derived in chapter 5, provides guidelines for developing such an interfacial area concentration model. Values for the dimensionless terms are provided in Table 8.1. Notice that the value of $\frac{\sigma_L}{g\Delta\rho D^2}$ is fairly constant. This is due to the small variations in pressure and temperature among the 18 flow cases. Therefore, this term is dropped from equation 5-12. Tests indicate that the flow data in Table 8.1 can best be correlated with the interfacial area concentration in the form of Equation 8-15.

$$a_i D = C \cdot (\frac{v_G}{v_L})^a \cdot (\frac{v_L}{D^{3/2} g^{1/2}})^b \cdot (\frac{q_L}{v_L D})^c \cdot (\frac{q_G}{q_L})^d \cdot (\frac{\Delta\rho}{\rho_G})^e \qquad (8\text{-}15)$$

The resultant equation is approximated by using standard regression analysis as:

$$a_i D = 376.43 \cdot (\frac{v_G}{v_L})^{0.935} \cdot (\frac{v_L}{D^{3/2} g^{1/2}})^{0.804} \cdot (\frac{q_L}{v_L D})^{-0.455} \cdot (\frac{q_G}{q_L})^{0.788} \cdot (\frac{\Delta\rho}{\rho_G})^{1.235} \qquad (8\text{-}16)$$

Figure 8.32 provides the comparison between the proposed correlation with the present flow data. The coefficient of this linear correlation is 0.97 and the standard derivation is 0.6 m^{-1}. Equation 8-16 can be further simplified by combining the common terms as:

$$a_i = 376.43 \cdot \frac{v_G^{0.935} v_L^{0.324} g^{0.053} q_G^{0.788}}{D^{1.751} q_L^{1.243}} \cdot (\frac{\Delta\rho}{\rho_G})^{1.235} \qquad (8\text{-}17)$$

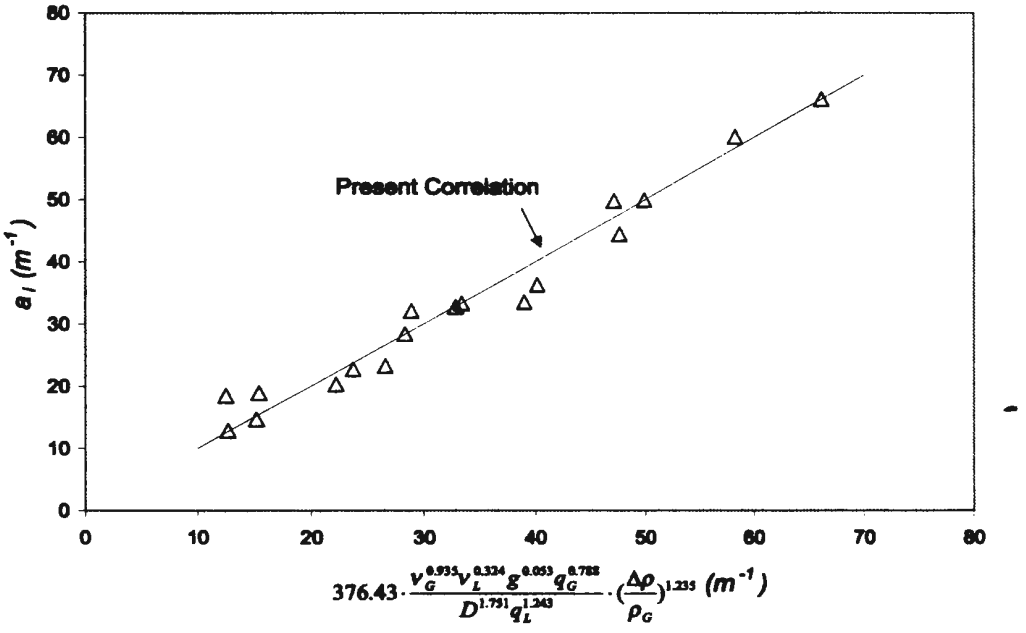

Figure 8.32 - Present interfacial area concentration correlation [Δ Present data]

Equation 8-17 indicates that the interfacial area concentration increases with the increases in both liquid and gas viscosities, gas flow rate and density difference. It decrease with increases in liquid flow rate, pipe diameter and gas density. Its decrease with pipe diameter is expected since the volume to surface ratio of a slug decreases with increasing pipe diameter, which is consistent with the flow description discussed in section 8.1. The use of volume flow rate instead of the void fraction, which is commonly used in other correlation functions, makes this model much easier to implement in practice since the volume flow rates are often readily available, especially in laboratory settings. It should be noted that the application of this model is only valid for vertically upward air-water slug flows.

8.3 Concluding Remarks

Investigations have been performed to understand void fraction, slug/bubble void fractions, slug/bubble velocities, slug/bubble dimensions, slug/bubble frequencies, and interfacial area concentration for vertically upward air-water slug flow in this chapter. The results of the flow measurements are summerized in Table 8.2.

Table 8.2 Results of Flow Measurements

Case	ε	ε_s	u_s (m/s)	u_b (m/s)	u_{LS} (m/s)	L/D	d/D	ai (1/m)
1	0.19	0.09	1.57	1.29	1.15	1.30	0.17	49.81
2	0.16	0.09	1.75	1.38	1.22	1.18	0.15	44.42
3	0.30	0.21	1.96	1.60	1.45	2.08	0.13	66.12
4	0.14	0.06	1.99	1.62	1.66	1.09	0.20	33.31
5	0.17	0.08	2.23	1.86	1.77	1.65	0.16	49.90
6	0.23	0.16	2.13	1.81	1.94	2.10	0.11	60.07
7	0.11	0.06	2.16	1.90	1.86	1.07	0.12	32.74
8	0.17	0.10	2.41	2.01	1.96	1.87	0.16	36.31
9	0.18	0.13	2.62	2.10	1.98	2.33	0.15	33.57
10	0.08	0.04	2.44	2.20	2.24	1.05	0.19	18.90
11	0.11	0.42	2.51	2.29	2.22	1.50	0.26	23.28
12	0.14	0.09	2.60	2.33	2.41	1.81	0.17	28.39
13	0.16	0.10	2.98	2.39	2.46	2.18	0.17	32.09
14	0.17	0.08	2.89	2.61	2.48	1.28	0.21	14.70
15	0.10	0.07	2.75	2.55	2.69	1.30	0.16	20.30
16	0.17	0.12	3.33	2.91	2.71	2.10	0.22	22.70
17	0.09	0.07	3.06	2.75	2.85	1.21	0.22	12.90
18	0.11	0.07	3.16	2.88	2.97	1.65	0.20	18.50

The air-water two-phase vertically upward slug flow shows the following characteristics:

1. The distributions of void fraction, bubble velocity, average bubble/slug velocity, bubble diameter, slug frequency, bubble frequency, slug void fraction and interfacial area concentration have a central maximum with a relatively rapid decrease close to the wall.
2. Slug velocities and lengths are fairly constant across pipe cross section.

3. Slug velocities are greater than the velocities of the smaller bubbles.
4. Bubble velocities and average bubble/slug velocities are very similar across the pipe cross section.
5. Void fraction distribution is closely related to slug and bubble sizes, slug/bubble frequencies, slug void fraction, as well as slug/bubble velocities.
6. The increase in gas flow at a constant liquid flow generally increases slug velocity, bubble velocity, average bubble/slug velocity, slug length, bubble length, void fraction, slug void fraction, slug frequency, bubble frequency and interfacial area concentration, but the bubble diameter decreases with the increasing gas flow.
7. The different flow behaviors observed with increasing liquid flow are due to the existence of a discontinuity in the slug flow regime. A Froude number of 3 of the mixture can be used to differentiate the sub-regimes.
8. An increase in liquid flow at a constant gas flow generally increases slug velocity, bubble velocity, average bubble/slug velocity and bubble diameter, but decreases void fraction, slug void fraction and interfacial area concentration. However, the variations in slug length, slug and bubble frequencies depend on the flow sub-regimes.
9. Slug frequency is in the range of 1.2 – 3.1 Hz for the 18 flow cases.
10. The majority of gas bubbles in the flow are small bubbles. The local bubble/slug frequency ratio is in the order of 10. However, the global bubble/slug ratio is expected to be much higher since the detection of a slug is global while the detection of a small bubble is relatively local. A significant portion of the air volume is occupied by the minority slugs.

11. A linear relation exists between the global void fraction and the superficial volume flow ratio, β. The global slug void fraction is linearly proportional to the global void fraction.
12. Slug/bubble sizes and bubble frequency can be correlated with the Froude number of the liquid, superficial gas and liquid velocity ratio and a dimensionless density term.
13. Correlations for predicting the interfacial area concentration have been developed. Comparisons of the interfacial area concentration with those reported for bubble flow reveal that correlatons developed for bubble flow are not valid for slug flows.

Chapter 9

Conclusions and Recommendations

9.1 Conclusions

The identification of flow patterns and prediction of interfacial area concentration are two important aspects in formulating the closure laws for two-phase flow models. In this thesis, a systematic investigation of vertically upward air-water slug flow has been presented. This study yields a more detailed knowledge of the flow and provides correlations to identify flow patterns, and predict interfacial area concentrations. In conclusion, the major contributions of this study can be summarized as follows:

1. A 3-inch ID and 180-foot long multiphase research flow loop has been designed and constructed. This flow loop is equipped with an integrated computerized data acquisition and operational control system. It is the first multiphase flow research facility that has been built in the Atlantic Canada region. The construction of this flow loop coincides with the increasing oil and gas activities taking place in this region. A wide range of flow patterns and conditions can be simulated in this flow loop, although the current study was focused on vertically upward air-water slug flow. The accurate instrumentation of this facility makes it suitable for both

conducting multiphase flow research and testing multiphase flow measurement systems.

2. A new dimensionless flow pattern map has been proposed. The functional equation governing the flow pattern formation is analyzed using dimensional analysis to formulate the proper dimensionless plotting parameters. The use of these parameters makes the resultant flow pattern map independent of flow geometry and fluid physical properties. Data collected from the MUN flow loop as well as from the literature were used to generate the new flow pattern map. Flow pattern boundaries are systematically determined using the MICD pattern recognition technique. The improved agreement among the data from different facilities indicates that the new flow pattern map is superior to other traditional flow pattern maps, and provides good portability to flow geometry and fluid physical properties
3. A simultaneous flow measurement system using both dual-probe hot-film anemometry and high-speed flow visualization was developed to obtain quantitative information about the flow. This system allows the comparison of the two flow measurement techniques. A supervised motion tracking and an edge detection cross correlation image processing algorithms have been used to verify the accuracy of the hot-film data reduction techniques developed in this study.
4. To interpret the hot-film signal, the dynamic response of the signal to the passage of a gas slug was investigated with the assistance of high-speed flow images. This information has not been previously available. Based on this study, a combined amplitude and first-order time derivative phase detection method has been developed to discriminate the signal into gas and liquid. The improved algorithm is superior to

those proposed by others, because it more realistically reflects the dynamic interaction between the hot-film and the two flow phases.

5. All previously reported measurements on two-phase flow result in an average flow information about the entire gas slug/bubble population. For developing a more accurate flow model, it is necessary to obtain more detailed flow information. An innovative data reduction technique using wavelet analysis combined with the phase detection method has been developed to decompose the original hot-film signals into signals corresponding to air slugs and bubbles. The unique features of wavelet analysis make it superior to the commonly used traditional Fourier transformation. It allows the main signal features to be preserved while removing the signals associated with noise and tiny gas bubbles. The data reduction technique results in two velocities corresponding to the slugs and bubbles from the cross-correlation analysis of the discriminated signals. The corresponding slug/bubble sizes, slug/bubble frequencies and slug/bubble void fractions were also estimated. Additionally, in wavelet transformation, the passage of slugs and bubbles is reflected by a sudden frequency variation with a precise temporal location. This can provide valuable information for better understanding the flow. The signal processing technique presented in this thesis has never been attempted previously by others in similar studies.
6. Measurements and estimations of slug/bubble void fractions, slug/bubble velocities, slug/bubble sizes and slug/bubble frequencies for slug flow were carried out under a significant range of flow conditions. Some of the flow information was not available or fully understood previously. The results were systematically analyzed to yield more detailed flow information. For the current experimental setup, the mean

velocities of air slugs, bubbles and liquid slugs are slightly lower than those predicted by the traditional phase velocity models. Some new coefficients for these models were recommended. New correlations for predicting slug/bubble sizes, slug void fraction and bubble frequency have also been developed for vertically upward developing air-water slug flow.

7. The resultant slug/bubble sizes and slug/bubble void fractions provide information necessary for estimating the interfacial area concentrations. Extremely limited information is available on the interfacial area concentration and its modeling. Most of the few available studies were conducted on bubble flow. There seems to be no systematic study conducted on vertically upward slug flow. A simplistic method for estimating the interfacial area concentration of slug flow was formulated. It allows the approximation of the interfacial area concentration from the flow measurement by a single normal hot-film probe. This technique has not been systematically investigated previously by others.
8. Comparisons of the resultant interfacial area concentrations with the correlations proposed for bubble flow indicate that these correlations are not suitable for slug flow. An interfacial area concentration model was, therefore, proposed for slug flow based on the synthesis method. The resultant correlation indicates that the interfacial area concentration is closely related to flow and fluid properties of the two phases. It can provide closure laws for modeling of vertically upward slug flow.
9. The data reduction techniques developed in this study provide the basis for the signal processing algorithms for the INSTRUMAR MPFM.

9.2 Recommendations

Although a significant amount of study has been conducted on slug flow, the understanding of its flow mechanism is far from complete. It is recommended that additional work be conducted to enhance the understanding of vertically upward two-phase slug flow. This future work would include the following:

1. More data should be collected for different fluids and flow dimensions to verify and improve the new dimensionless flow pattern map.
2. The development of the present interfacial area concentration model assumes that the bubbles are spherical and the slugs are regular bullet-like shapes. A more accurate prediction of the interfacial area concentration can be achieved if the variations of bubble dimension and shape under various flow conditions are considered. Techniques and data processing algorithms need to be developed to obtain such flow information.
3. Flow measurements at different streamwise locations (L/D) need to be performed to understand how the flow behaves and evolves along its streamwise direction. This includes the understanding of how slug/bubble velocities, slug/bubble void fractions, slug/bubble frequencies, slug/bubble dimensions and shapes, and interfacial area concentration vary and develop along the flow
4. Flow information near the wall need to be obtained to get a more complete understanding of the flow. This will augment our understanding of how the flow interacts with the wall and will help to predict the wall shear stress.

5. Other flow measurement strategies, such as the multiple probe method, may be used to obtain more accurate bubble size information. Consequently, this will improve the estimation of interfacial area concentration.
6. More flow conditions are needed to incorporate into the new correlations to improve their accuracy and the range of application.

References

Abel, R. and Resch, F.J., 1978. "A method for the analysis of hot-film anemometer signal in two-phase flows", *Int. J. Multiphase Flow*, Vol. 4, pp. 523-533.

Abouelwafa, M.S., and Kendall, E.J.M., 1980. "The measurement of component ratio in multiphase systems using gamma ray attenuation", *J. Phs. E. Sci. Instrum.*, 13, pp. 341-345.

Adrian, R.J., 1991. "Particle-Imaging Techniques for Experimental Fluid Mechanics", *Annual Review of Fluid Mechanics*, Vol. 23, pp. 261-304.

Akagawa, K., and Sakaguchi, T., 1966. "Bulletin J.S.M.E.", Volume 9, pp. 104.

Akita, K. and Yoshida, F., 1974. "Bubble size, interfacial area, and liquid-phase mass transfer coefficient in bubble columns", *Ind. Eng. Chem., Process Des. Develop.*, 13, pp. 84-91.

Annurgiates, M. and G. Giradi, 1983. "Flow pattern analysis on upward two-phase flow in 92 mm I.D. vertical tube", *European Two Phase Flow Group Meeting*, Paper H11, Zurich.

Bachalo, W.D., 1994. "Experimental methods in multiphase flows", *Int. J. Multiphase Flow*, Vol. 20, pp. 261-295.

Baker, J.J.L., 1965. "Flow regime transition at elevated pressures in vertical two-phase flow", *Argonne National Lab Report*, ANL 7093.

Baker, O., 1954. "Simultaneous flow of oil and gas", *Oil Gas J.*, 26, July, pp. 185-195.

Barr, D.I.H., 1969. "Method of synthesis – basic procedures for the new approach to similitude", *Water Power*, 21, April and May, pp. 148-153 and pp. 83-188.

Barr, D.I.H., 1971. "The proportionalities method of dimensional analysis", *J. Franklin Inst.*, 292, No. 6, (special issue).

Bendiksen, K.H., 1984. "An experimental investigation of the motion of long bubbles in inclined tubes", AIChE J., 39, pp. 1281-1291.

Bennet, A.W., Hewitt, G.F., Kearsey, H.A., Keeys, R K.F. and Lacey, P.M.C., 1965. "Flow visualization studies of boiling at high pressure", *AERE-R*, 4874.

Bergles, A.E. and Suo, M., 1966. "Investigation of boiling water flow regimes at high pressure", *Pynatech Corporation Report* 3304-8.

Buckingham, E., 1914. "On physically similar systems" *Phys. Rev.*, **4**, pp. 345.

Cartellier, A., 1990. "Optical probes for local void fraction measurements: Characterization of performance", *Rev. Sci. Instrum.*, 61 (2), pp. 874-886.

Cartellier, A., 1992. "Simultaneous void fraction measurement, bubble velocity, and size estimate using a single optical probe in gas-liquid two-phase flows", *Rev. Sci. Instrum.*, 63 (11), pp. 5442-5453.

Chark, N.N. and Turton, R., 1988. "Chord length distributions related to bubble size distributions in multiphase flows", *Int. J. Multiphase Flow*, Vol. 14, No. 4, pp. 413-424.

Chen, X.T. and Brill, J.P., 1997. "Slug to churn transition in upward vertical two-phase flow", *Chemical Enigineering Science*, Vol. 52, No. 23, pp. 4269-4272.

Cheng, H., Hill, J.H. and Azzorpardi, B.J., 1998. "A study of the bubble-to-slug transition in vertical gas-liquid flow in columns of different diameter", *Int. J. Multiphase Flow*, Vol. 24, No. 3, pp. 431-452.

Ching, C.Y., Hiscock, J., Cheng, X. and Robinson, J., 1999a. "Estimation of gas slug velocities in two-phase flows using successive images of the flow", *Proc. 17th Canadian Congress of Applied Mechanics CANCAM 99* (ed. S. Ziada and D.S. Weaver), pp. 173-174.

Davis, R.M., and Taylor, G.I., 1950. "The mechanics of large bubbles rising through extended liquids and through liquids in tubes", *Proc. R. Soc.* (London), 200, Ser. A. pp. 375-390.

DeJuses, J.M. and Kawaji, M., 1990. "Investigation of interfacial area and void fraction in upward co-current gas-liquid flow", *Can. J. Chem. Eng.*, 68, pp. 904-912.

Delhaye, J.M. and Brichard, P., 1994. "Interfacial area in bubble flow: Experimental data and correlations", *Nucl. Eng. Des.*, 151, pp. 65-77.

Dukler, A.E. and Hubbard, M.G., 1975. "A model for gas-liquid slug flow in horizontal tubes", *Ind. Eng. Fundam.*, 14, pp. 337-347.

Dukler, A.E., Maron, D.M. and Brauner, N., 1985. "A physical model for predicting the minimum stable slug length", *Chem. Engng. Sci.*, 40, pp. 1379-1385.

Ellis, J.E. and Jones, E.L, 1980. "Vertical gas-liquid model and interfacial area", ANL 80-111 NUREG/CR-1873.

Farrar, B. and Brunn, H.H., 1989. "Interaction effects between a cylindrical hot-film anemometer probe and bubbles in air/water and oil/water flows", *J. Phys. E. Sci. Instr.*, Vol. 22, pp. 114-123.

Farrar, B., 1988. "Hot-film anemometry in dispersed oil-water flows". *Ph.D. thesis, Department of Mechanical and Manufacturing Engineering, University of Bradford.*

Farrar, B., Samways, A. L., Ali, J. and Brunn, H.H., 1995. "A computer-based hot film technique for two-phase flow measurement", *Meas. Sci. Technol.*, Vol. 6, pp. 1528-1537.

Farrar, B., Samways, A. L., Ali, J. and Brunn, H.H., 1995. "A computer-based hot film technique for two-phase flow measurement", *Meas. Sci. Technol.*, 6, pp. 1528-1537.

Gopal, M. and Jepson, W.P., 1998. "The study of dynamic slug flow characteristics using digital image analysis – Part I: Flow visualization", *Journal of Energy Resources Technology*, Vol. 120, pp. 97-101.

Graps, A., 1995. "An introduction to wavelets". *IEEE Computational Science & Engineering,* Vol. 2, No. 2, pp. 50-61.

Griffith, P. and Wallis, G.B., 1961. "Two-phase slug flow", *J. Heat Transfer*, Ser. C, 83(3), pp. 307-320.

Griffith, P., 1963. "The prediction of low-quality boiling voids", ASME paper 63-HT-20, *National Heat Transfer Conference*, Boston.

Haberman, W.L. and Mortan, R.K., 1953. "An experimental investigation of the drag and shape of air bubbles rising in various liquids", *David W. Taylor Model Basin Report* 802.

Hall, A.R.W., 1997. "Flow patterns in the three-phase flows of oil, water, and gas", *BHR Group 1997 Multiphase 97*, pp. 241-256.

Hammer E.A., Tollefsen, J. and Olsvik, K., 1989. "Capacitance transducers for non-intrusive measurement of water in crude oil", *Flow Meas. Instrum.*, 1, pp. 51-58.

Harmathy, T.Z., 1969. "Velocity of large drops and bubbles in media of infinite and restricted extent", *A.I.Ch.E. J.*, 6, pp. 281.

Hawighorst, A., 1983. "Drop size measurement in a vertical gas-liquid flow", *Proceedings of the International Union of Theoretical and Applied Mechanics Symposium.*

Hay, K.J., Liu, Z.C. and Hanratty, T.J., 1998. "A backlighted imaging technique for particle size measurements in two-phase flows", *Experiments in Fluids*, Vol. 25, pp.226-232.

Herringe, R.A. and Davis, M.R., 1974. "Detection of instantaneous phase change in gas-liquid mixtures", *J. Phys. E. Sci. Instrum.*, 7, pp. 807-812.

Herringe, R.A. and Davis, M.R., 1976. "Structure development of gas-liquid mixture flows", *J. Fluid Mech.*, 73, pp. 97-123.

Hetsroni, G., 1982. "Handbook of Multiphase Systems", *Hemisphere* and *McGraw-Hill.*

Hewitt, G.F. and Hall-Taylor, N.S. 1970. "Annular Two-Phase Flow", *Pergamon Press.*

Hewitt, G.F. and Roberts, D.N., 1969. "Studies of two-phase flow patterns by simultaneous X-ray and flash photography", *Rept. AERE-M2159, UKAEA*, Harwell.

Hewitt, G.F., Harrison, P.S., Parry, S.J. and Shires, G.L., 1995. "Development and testing of the Mixmeter multiphase flow meter", *Proc. 13th North Sea Flow Measurement Workshop, Lillehammer, Norway.*

Hibiki, T., Hogsett, S, and Ishii, M., 1998. "Local measurement of interfacial area, interfacial velocity and liquid turbulent in two-phase flow", *Nuclear Engineering and Design* 184, pp. 287-304.

Hinze, J.O., 1955. "Fundamentals of the hydrodynamic mechanism of splitting dispersion processes", *AIChE J.*, 1, pp. 289.

Hiscock, J., Mouland, D., Wang, G. and Ching, C.Y., 2000. "Gas Bubble Velocity Measurements using High-Speed Images of Gas-Liquid Flows". *2000 ASME Fluids Engineering Summer Conference: Symposium on Noninvasive Measurements in Multiphase Flows.*

Hoogendoorn, C. J., 1959. "Gas-liquid flow in horizontal pipes", *Chem. Engng. Sci.*, 9, pp. 205-217.

Hutton, G., 1997. "Multiphase flow meters and application trends", *OTC*, Houston, U.S.A.

Ishii, M. and Mishima, K., 1980. "Study of two-fluid model and interfacial area", ANL 8-111, NUREG/CR-1873.

Ishii, M. and Mishima, K., 1984. "Two-fluid model and hydrodynamic constitutive relations", *Nuclear Engineering and Design* 82, pp. 107-126.

Ishii, M., 1975. "Thermo-fluid dynamic theory of two-phase flow", *Eyrolls*, Paris/Scientific and Medical Publications of France, New York.

Jones, O.C. and Zuber, N., 1978. "Use of a cylindrical hot-film anemometer for measurement of two-phase void and volume flux profiles in a narrow rectangular channel", *AIChE Symp. Series*, 74, No.174, pp. 191-204.

Kasturi, G. and Stepanek, J.B., 1974. "Two-phase flow – III. Interfacial area in co-current gas-liquid flow", *Chem. Eng. Sci.*, 29, pp. 713-719.

Kataoka, I., Ishii, M. and Serizawa, A., 1986. "Local formulation and measurements of interfacial area concentration in two-phase flow", *Int. J. Multiphase Flow*, Vol.12, No. 4, pp. 505-52.

King, N.W., 1992. "A multiphase flowmeter test and calibration facility", *Proceeding of 24th OTC*, Texas, pp. 553-563.

Kirouac, G.J., Trabold, T.A., Vasallo, P.F., Moore, W.E. and Kumar, R., 1999. "Instrumentation development in two-phase flow", *Experimental Thermal and Fluid Science*, Vol. 20, pp. 79-93.

Kocamustafaogullari, G., Huang, W.D., and Razi, J., 1994. "Measurement and modeling of average void fraction, bubble size and interfacial area", *Nuclear Engineering and Design*, 148, pp. 437-453.

Kokal, S.L. and Stanislav, J.F., 1989. "An experimental study of two-phase flow in slightly inclined pipes – I. Flow patterns", *Chem. Engng. Sci.*, 44, pp. 665-679.

Kolmogorov, A.N., 1949. "On the disintegration of drops in a turbulent flow", *Kokl. Akad. Nauk.*, SSSR 66, pp. 825.

Kosterin, S.I., 1949. "An investigation of the influence of diameter and inclination of a tube on the hydraulic resistance and flow structure of gas liquid mixtures", *Izv. Akad. Nauk SSSR, Otdel Tekh., Nauk*, 12, pp. 1824-1830.

Lemonnier, H., 1997. "Multiphase instrumentation: the keystone of multidimensional multiphase flow modeling", *Experimental Thermal and Fluid Science*, Vol. 15, pp. 154-162.

Levy, S., 1999. "Two-Phase Flow in Complex Systems", John Wiley & Son Inc.

Lin, P.Y. and Hanratty, T. J., 1987. "The effect of pipe diameter on flow patterns for air water flow in horizontal pipes", *Int. J. Multiphase Flow*, **13**, pp. 549-563.

Liu, T. J. and Bankoff, S. G., 1993a. "Structure of air-water bubbly flow in a vertical pipe - I. Liquid mean velocity and turbulence measurements", *Int. J. Heat Mass Transfer*, Vol. 36, No. 4, pp. 1049-1060.

Liu, T. J. and Bankoff, S. G., 1993b. "Structure of air-water bubbly flow in a vertical pipe - II. Void fraction, bubble velocity and bubble size distribution", *Int. J. Heat Mass Transfer*, Vol. 36, No. 4, pp. 1061-1072.

Liu, T.J., 1991. "The effect of bubble size on void fraction distribution in a vertical channel", *Proceedings of the Conference on Multiphase Flow*, Tsukuba, Japan, Vol. 1, pp. 453-457.

Lucas, G.P. and Simonian, S., 1991. "Towards a phase-distribution-independent impedance volume-fraction measurement", *Flow Meas. Instrum.*, 2, pp. 105-114.

Lunde, O., Hustvedt, E. and Linga, H., 1998. "Field measurements of volumetric phase fraction in multiphase flowlines", *Flow Meas. INSTRUM.*, 2, pp. 105-114

Mamayev, V.A., Odisharia, G.E., Klapchuk, O.V., Tochigin, A.A. and Semyonov, N.I, 1978. "Motion of Gas-Liquid Mixtures in Pipes", Nedra, Moscow.

Maron, M.D., Yacoub, N. and Brauner, N., 1982. "New thoughts on the mechanisms of gas-liquid slug flow", *Lett. Heat Mass Transfer*, 9, pp. 333-342.

Marshall, A. R., 1996. "Functional requirement specification for a pre-production prototype multiphase flow meter", *Instrumar Ltd., Project document* FRS/0525/001.

McQuillan, K.W. and Whalley, P.B. 1985. "Flow patterns in vertical two-phase flow", *Int. J. Multiphase Flow*, **11**, No. 2, pp. 161-175.

Meng, H., Boot, P. and Van Der Geld, C.W.M., 1995. "High pressure optical measurements of sizes, velocities and longitudinal positions of bubbles", *Int. J. of Multiphase Flow*, Vol. 21, No. 1, pp. 95-105.

Merilo, M., Dechene, R.L. and Cicowlas, W.M., 1977. "Void fraction measurement with a rotating electric field conductance gauge", *J. Heat Transfer Trans.*, ASME 99, pp. 330-331.

Millington, B., 1997. "Multiphase flow metering: a review", *3rd International Conference on Multiphase Metering*, Aberdeen, UK.

Moffat, R.J., 1988. "Describing the uncertainties in experimental results", *Experimental Thermal and Fluid Science*, 1, pp3-17.

Moujaes, S.F. and Sparks, J.C., 1998. "Determination of local two-phase variables and flow pattern characterization in an upward-flow rectangular channel", *Proceeding of the ASME Heat Transfer Division*, IMECE98, HTD Vol. 361-5, pp. 281-288.

Neal, L.G., 1963. "Analysis of slip in gas-liquid flow applicable to the bubble and slug flow regimes", Report KR-62, *Kjeller Research Establishment*, Kjeller, Norway.

Newson, I.H., 1964. "Heat transfer and pressure drop during horizontal flow of two-phase two-component mixtures", *Ph.D. thesis*, London.

Nicholson, M.K., Aziz, K. and Gregory, G., 1978. "Intermittent two-phase flow in horizontal pipes: predictable models", *Can. J. Chem. Eng.*, 56, pp. 653-663.

Nicklin, D.J., Wilkes, J.O. and Davidson, J.E., 1962. "Two-phase flow in vertical tubes", *Trans. Inst. Chem.* Eng., 40, pp. 61-68.

Ohba, K., Tsutomu, H. and Matsuyama, H., 1987. "Simultaneous measurements of bubble and liquid velocities in two-phase flow using LDA", *Bulletin of JSME*, Vol. 29, pp. 2487-2493.

Okawa, K., Yoneda, K. and Yoshioka, Y. 1998. "New interfacial area drag force model including effect of bubble wake, (I) Model development for steam-water bubbly flow in large-diameter pipes", *Journal of Nuclear Sciences and Technology*, Vol. 35, No. 12, pp. 895-904.

Paglianti, A., Giona, M. and Soldati, A., 1996. "Characterization of subregimes in two-phase slug flow", *Int. J. Multiphase Flow*, Vol. 22, No. 4, pp. 783-796.

Park, J.W, 1992. "Void wave propagation in two-phase flow", *Ph.D. thesis*, Rensselaer Polytechnic Institute.

Peebles, F.N. and Garber, H.J., 1953. "Studies of the motion of gas bubbles in liquids", *Chem. Eng. Prog.*, 49, pp. 88-97.

Peterson, D.A., Tankin, R.S. and Bankoff, S.G., 1983. "Holographic measurements of bubble size and velocity in a three-phase system", *Proceedings of the International Union of Theoretical and Applied Mechanics Symposium.*

Prenel, J.P., Porcar, R. and Rhassouli, A. El, 1989. "Three-dimensional flow analysis by means of sequential and volumic laser sheet illumination", *Experiments in Fluids*, Vol. 7, pp. 133-137.

Resch, F.J., Leutheussar, H.J. and Alemu, S., 1974. "Bubbly two-phase flow in hydraulic jump", *J. Hyd. Div. ASCE*, 100, pp. 137-149.

Roach, G.J., Watt, J.S., Zastawny, H.W., Hartley, P.E. and Ellis, W.K. 1994. "Multiphase flow meter for oil-water-gas in pipelines based on gamma-ray transmission techniques", *Nucl. Geophys.*, 8, pp. 225-242.

Samways, A.L., Ali, J., Al-Deen, M.F.N. and Bruun, H.H., 1994. "The calibration and measurements with cylindrical hot-film probes in water flow", *Meas. Sci. Technol.*, 5, pp. 1551-1559.

Schmidt, Z., Brill. J.P. and Beggs, H.D., 1981. "Experimental study of two-phase normal slug flow in pipeline rise pipe system", *Journal of Energy Resources Technology*, Vol. 103, pp. 67-75.

Scott, D.S., 1963. "Properties of concurrent gas-liquid flow". *Advances in Chemical Engineering*, **4**, Academic Press, New York.

Seleghim, P. Jr. and Hervieu, E., 1998. "Direct imaging of two-phase flows by electrical impedance measurements", *Measurement Science Technology*, Vol. 9, pp. 1492-1500.

Serizawa, A., Kataoka, I. and Michiyoshi, I., 1975a. "Turbulence structure of air-water bubbly flow I. measuring techniques", *Int. J. Multiphase Flow*, 2, pp. 221-233.

Serizawa, A., Kataoka, I. and Michiyoshi, I., 1975b. "Turbulence structure of air-water bubbly flow II. local properties", *Int. J. Multiphase Flow*, 2, pp. 235-246.

Serizawa, A., Kataoka, I. and Michiyoshi, I., 1975c. "Turbulence structure of air-water bubbly flow III. Transport properties", *Int. J. Multiphase Flow*, 2, pp. 247-259.

Serizawa, A., Kataoka, I. and Michiyoshi, I., 1987. "Phase distribution in bubbly flow", *Second International Workshop on Two-Phase Flow Fundamentals, Troy, NY.*

Serizawa, A., Tsida, K. and Michiyoshi, I., 1983. "Real-time measurement of two-phase flow turbulence using dual-sensor anemometry", *Proc. Symp. on Measuring Techniques in Gas-Liquid Two-Phase Flows*, Nancy, France, pp. 495-523.

Sevik, M. and Park, S.H., 1973. "The splitting of drops and bubbles by turbulent fluid flow", *J. Fluids Eng.*, 95, pp. 53.

Sharp J.J., 1981. "Hydraulic Modeling", *Butterworth & Co.*

Sharp, J.J. 1973. "Basic applications of similitude theory", *Water & water Engng.*, **77**, No. 931, pp. 344-349.

Sharp, J.J. 1975. "Application of dimensional reasoning to thermal systems", *J. of the Franklin Inst.*, **299**, No. 3, pp. 191-197.

Shilimkan, R.V. and Stepanek, J.B., 1978. "Interfacial area in concurrent gas-liquid flow in tubes of various size", *Chem. Eng. Sci.*, 32, pp. 149-154.

Sleicher, C.A., 1962. "Maximum drop size in turbulent flow", *AIChE J.*, 8, pp. 471.

Spedding, P.L. and Nguyen, V.T., 1980. "Regime maps for air-water two-phase flow", *Chem. Engng. Sci.*, **35**, pp. 799-793.

Spedding, P.L. and Spence, D.R., 1993. "Flow regimes in two-phase gas-liquid flow", *Int. J. Multiphase Flow*, 19, No. 2, pp. 245-280.

Tabei, K., Hasatani, M. and Kuroda, M., 1989. "Effective gas-liquid interfacial area in mobile-bed contactor", *Int. Chem. Eng.*, 29, pp. 679-688.

Taitel, Y., Bornea, D. and Dukler, A.E., 1980. "Modeling flow pattern transitions for steady upward gas-liquid flow in vertical tubes", *AIChE J.*, **26**, pp. 345-354.

Taylor, G.E., 1934. "The formation of emulsion in definable field of flow", *Pro. R. Soc., London*, A164, pp. 501.

Thang, N.T. and Davis, M.R., 1979. "The structure of bubbly flow through Venturis", *Int. J. Multiphase Flow*, Vol. 5, pp. 17-37.

Thorn, R., Johansen, G.A. and Hammer, E.A., 1997. " Recent development in three-phase flow measurement", *Meas. Sci. Technol.*, 8, pp. 691-701.

Tomida, T., Yusa, F. and Okazaki, T., 1978. "Effective interfacial area and liquid-side mass transfer coefficient in the upward two-phase flow of gas-liquid mixtures", *Chem. Eng. J.*, 16, pp. 81-88.

Tou, J.T. and Gonzales, R.C., 1974. "Pattern Recognition Principles", *Addison-Wesley*.

Tronconi, E., 1976. "Prediction of slug frequency in horizontal two-phase slug flow", AIChE J., 36, pp. 701-709.

Uga, T., 1972. "Determination of bubble-size distribution in a BWR", *Nucl. Engng Design*, 22, pp. 252-261.

Van Santen, H., Kolar, Z.I. and Scheers, A.M., 1995. "Photon energy selection for dual energy γ-and/or X-ray absorption composition measurements in oil-water-gas mixtures", *Nucl. Geophys.*, 9, pp. 193-202.

Wallis, G.B., 1961. "Some hydrodynamic aspect of two-phase flow and boiling", *Proceedings of the International Heat Transfer Conference*, Boulder, Colo., Paper 38.

Wallis, G.B., 1962. "General correlation for the rise velocity of cylindrical bubbles in inclined tubes", *GE Report* 626L130.

Wang, S.K., Lee, S.J., Jones, O.C. and Latey, R.T., 1987. "Turbulent structure and phase distribution measurements in bubbly two-phase flows", *Int. J. Multiphase Flow*, 3, pp. 327-343.

Weisman, J. and Kang, S.Y., 1981. "Flow pattern transition in vertical and upwardly inclined lines", *Int. J. Multiphase Flow*, 4, pp. 271-291.

Welle, R., 1985. "Void fraction, bubble velocity and bubble size in two-phase flow", *Int J. Multiphase Flow*, Vol. 11, No.3, pp. 317-345.

Zeitoun, O., Shoukri, M. and Chatoorgoon, V., 1994. "Measurement of interfacial area concentration in subcooled liquid-vapor flow", *Nuclear Engineering and Design*, 152, pp. 243-255.

Zuber, N. 1964. "On the dispersed two-phase flow in the laminar flow regimes", *Chem. Eng. Sci.*, 19.

Zuber, N. and Findlay, J.A., 1965. "Average volumetric concentration in two-phase flow systems", *J. Heat Transfer*, 87, pp. 453-468.

Zuber, N., and Hench, J., 1962. "Steady state and transient void fraction of bubbly systems and their operating limits 1: Steady state operation", *GE Report* 62GL100.

CENTRE FOR NFLD. STUDIES
JUL 18 1978
MEMORIAL UNIVERSITY
OF NEWFOUNDLAND